



저작자표시-비영리-변경금지 2.0 대한민국

이용자는 아래의 조건을 따르는 경우에 한하여 자유롭게

- 이 저작물을 복제, 배포, 전송, 전시, 공연 및 방송할 수 있습니다.

다음과 같은 조건을 따라야 합니다:



저작자표시. 귀하는 원저작자를 표시하여야 합니다.



비영리. 귀하는 이 저작물을 영리 목적으로 이용할 수 없습니다.



변경금지. 귀하는 이 저작물을 개작, 변형 또는 가공할 수 없습니다.

- 귀하는, 이 저작물의 재이용이나 배포의 경우, 이 저작물에 적용된 이용허락조건을 명확하게 나타내어야 합니다.
- 저작권자로부터 별도의 허가를 받으면 이러한 조건들은 적용되지 않습니다.

저작권법에 따른 이용자의 권리는 위의 내용에 의하여 영향을 받지 않습니다.

이것은 [이용허락규약\(Legal Code\)](#)을 이해하기 쉽게 요약한 것입니다.

[Disclaimer](#)

이학박사 학위논문

**Reconstruction of the genesis of banded iron
formation in North China Craton:
Evidences from geochemical studies on the
iron ore, related wall rock and magnetite**

북중국 호상철광상 성인과 지각 진화의 재구성:
광석, 관련된 모암, 자철석의 지구화학적 연구

2018년 8월

서울대학교 대학원
자연과학대학 지구환경과학부
문 인 경

Ph.D Thesis

**Reconstruction of the genesis of banded iron
formation in North China Craton:
Evidences from geochemical studies on the
iron ore, related wall rock and magnetite**

Inkyeong Moon

**A dissertation submitted in partial fulfillment of the
requirements for the degree of Doctor of Philosophy**

August 2018

**School of Earth and Environmental Sciences
Seoul National University**

**Reconstruction of the genesis of banded iron
formation in North China Craton:
Evidences from geochemical studies on the
iron ore, related wall rock and magnetite**

지도교수 이인성

이 논문을 이학박사 학위논문으로 제출함
2018년 8월

서울대학교 대학원
자연과학대학 지구환경과학부
문 인 경

문인경의 이학박사 학위논문을 인준함

2018년 8월

위 원 장	<u>허 영 숙</u>	(인)
부위원장	<u>이 인 성</u>	(인)
위 원	<u>박 정 우</u>	(인)
위 원	<u>신 동 복</u>	(인)
위 원	<u>김 중 욱</u>	(인)

Abstract

Reconstruction of the genesis of banded iron formation in North China Craton: Evidences from geochemical studies on the iron ore, related wall rock and magnetite

Inkyeong Moon
School of Earth and Environmental Sciences
The Graduate School
Seoul National University

My Ph.D. studies focus on the petrological, mineralogical and geochemical studies of iron ore and magnetite from banded iron formations (BIFs) and their related wall rock (amphibolite). I performed integrated studies on ore deposit geology, mineralogy, petrology and geochemistry on the Yishui BIF. Yishui BIF is located in North China Craton (NCC) and considered as the representative area for revealing an association between the genesis of BIF and tectonic setting. The genesis of Yishui BIF had never been studied before. The data constrained the genesis of these BIFs and provided information about the tectonic evolution of the Archean NCC. Additionally, the data provided an improved understanding of the petrogenesis of the BIF-related wall rocks. It can also be used to interpret the relationship between the BIFs and wall rock and the tectonic evolution of the NCC. Rare earth elements (REEs) and trace elements were used as geochemical proxies. The results of these studies suggest that the Yishui BIFs were precipitated from a mixture of less than 1% high-temperature hydrothermal fluids ($> 250\text{ }^{\circ}\text{C}$) and seawater. The abundant ore-forming materials, such as iron and silica, formed

under anoxic and suboxic submarine conditions. In addition, the protolith of the related wall rock (Yishui amphibolite) was alkali basalts reminiscent of ocean island basalt (OIB) and formed in an intraplate setting with no crustal assimilation during magma ascent. On the basis of these results, mantle plume model was preferred, which can explain the geochemical signatures of both the Yishui amphibolites and the Yishui BIFs. This model is also very consistent with the tectonic evolution of the NCC.

And, I determined trace element contents of magnetite from Superior–type BIFs and Algoma–type BIFs by in–situ LA–ICP–MS analyses. Combining the data obtained in my study with those from existing literatures, new systematic differences in magnetite composition between Archean Algoma–type and Paleoproterozoic Superior–type BIFs to understand the influence of their genetic conditions on magnetite chemistry were proposed. Magnetite is a representative ore mineral in BIFs and its composition can be a powerful indicator of petrogenesis and provenance. Previous studies classified BIFs into Algoma– and Superior–types based on their tectonic setting, size and lithologic associations. Our results, together with a compilation of previously reported trace element data on magnetite from other regions, indicate that there are systematic differences in trace element compositions of magnetite between Algoma– and Superior–type BIFs due to differences in their depositional environments. The magnetite from Algoma–type BIFs is more enriched in Al, Ti, Ni, and V than the magnetite from Superior–type BIFs. The former precipitated dominantly from high–temperature hydrothermal fluid under low oxygen fugacity conditions, whereas the latter formed mainly from low–temperature and relatively oxidized seawater. The results of the study demonstrate that the trace elemental composition trends of magnetite from

Algoma– and Superior–type BIFs are well consistent with previously suggested geochemical characteristics of these BIFs, further indicating the close relationship of BIFs with their genetic environments.

In addition, magnetite from the superior–type Yuanjiacun BIF in NCC was studied using Raman spectroscopy. The main purpose of the study was to clarify the relationship between the timing for the formation of Yuanjiacun BIF and the coeval oxygen fugacity (fO_2) through Raman analysis of magnetite. Combined with previous geochemical data, the results of this study suggest that the Yuanjiacun BIF has close relationship with Great Oxidation Event (GOE).

Keywords: Banded iron formations (BIFs), North China Craton (NCC), Great Oxidation Event (GOE), Geochemistry, Rare earth element (REE), Amphibolite, Magnetite, Precambrian

Student Number: 2012-20339

Table of Contents

Abstract	i
Table of Contents	iv
List of Figures	
.....	vi
ii	
List of Tables	
.....	x
v	
Chapter 1. Introduction	1
References	5
Chapter 2. Geochemical constraints on the genesis of the Algoma–type banded iron formation (BIF) in Yishui County, Western Shandong Province, North China Craton	9
Abstract	9
2.1. Introduction.....	10
2.2. Geological setting of the region and deposit.....	13
2.2.1. Regional Geology	13
2.2.2. Geology of the Yishui BIF	16
2.3. Petrology and mineralogy of the Yishui BIF	17
2.4. Analytical Methods.....	19
2.5. Results	20
2.5.1. Iron ore whole rock geochemistry	20
2.5.1.1. Major element analyses	20
2.5.1.2. Rare earth element and trace element analyses	21
2.5.2. Iron ore compositions	22
2.6. Discussion.....	23
2.6.1. Constraints on the source of the ore–forming material of the Yishui BIF.....	23
2.6.1.1. Detrital input	23
2.6.1.2. Source characteristics	24

2.6.2. Genesis of the Yishui BIF and tectonic implications.....	28
2.6.2.1. Depositional environment.....	28
2.6.2.2. Tectonic implications of the Archean NCC and a possible genetic model	29
2.7. Conclusions.....	31
References	33
Chapter 3. Archean tectonic evolution and the genetic link between wall rocks and BIFs in North China Craton.....	61
Abstract	61
3.1. Introduction.....	62
3.2. Regional and local geology.....	64
3.3. Sample description and analytical methods	66
3.3.1. Sample description	66
3.3.2. Analytical methods	67
3.4. Results	67
3.4.1. Major elements.....	67
3.4.2. Trace and rare earth elements.....	68
3.5. Discussion.....	69
3.5.1. Protolith reconstruction	69
3.5.1.1. Evaluation of element mobility	69
3.5.1.2. Petrological classification.....	70
3.5.1.3. Crustal contamination	70
3.5.2. Petrogenetic interpretation	71
3.5.2.1. Sources of mantle in the NCC.....	71
3.5.2.2. Tectonic significance.....	73
3.5.3. Genetic relationship between amphibolite and Yishui BIF.....	74
3.5.4. Implications for the evolution of the Eastern Block of the NCC.....	75
3.6. Conclusions.....	77
References	78
Chapter 4. Interpretation of formation condition in Superior–type banded iron formation (BIF) of Yuanjiacun in North China Craton using magnetite	96

Abstract	96
4.1. Introduction.....	97
4.2. Geological Setting.....	98
4.3. Method.....	99
4.4. Result.....	101
4.5. Discussion.....	102
4.5.1. The relationship between Yuanjiacun BIF and GOE	102
4.6. Conclusion	104
References	105

Chapter 5. In-situ LA-ICP-MS trace elements analyses of magnetite:

Implications for BIFs genesis and new insight on the geochemical difference between Algoma- and Superior-type BIFs	116
Abstract	116
5.1. Introduction.....	117
5.2. Geological background.....	118
5.2.1. The Yishui BIF	119
5.2.2. The Huoqiu BIF	120
5.2.3. The Yuanjiacun BIF	121
5.3. Analytical method	122
5.3.1. Whole-rock major and trace element analysis	122
5.3.2. Magnetite major and trace element analysis	122
5.4. Results	123
5.4.1. Algoma-type Yishui BIF	123
5.4.1.1. Petrography.....	123
5.4.1.2. Iron ore whole-rock composition.....	124
5.4.1.3. Magnetite composition.....	124
5.4.2. Superior-type Huoqiu BIF and Yuanjiacun BIF	125
5.4.2.1. Petrography	125
5.4.2.2. Geochemistry of iron ore	125
5.4.2.3. Geochemistry of magnetite	126
5.5. Discussion.....	126
5.5.1. Algoma- and Superior-type BIFs	126
5.5.2. Geochemical differences in magnetite from the Algoma- and	

Superior type BIFs	130
5.5.2.1. The global trend on the magnetite compositions	130
5.5.2.2. Regional trend on the magnetite compositions	134
5.6. Concluding remarks	137
References	139
Chapter 6. Summary and conclusions	161
요약 (국문초록).....	162

List of Figures

Figure 2.1. (a) Tectonic subdivisions of the North China Craton, modified after Zhao et al. (2005). SJ: Southern Jilin; NL: Northern Liaoning; AB: Anshan–Benxi; WL: Western Liaoning; EH: Eastern Hebei; SL: Southern Liaoning; ES: Eastern Shandong; WS: Western Shandong; MY: Miyun. (b) Geological map of the western Shandong Province, modified after Wan et al. (2011). (c) Geological map of the Yishui BIF (Lai and Yang, 2012b).

Figure 2.2. Representative photographs of the Yishui BIF and associated rocks. (a) Iron orebodies of the Yishui BIF with biotite–amphibole–leptynite and muscovite–quartz–schist (Lai and Yang, 2012b). (b) Iron orebodies with alternating Fe– and Si–rich layers (Lai and Yang, 2012b). (c) Iron ore with alternating Fe–rich and Si–rich bands. (d–e) Iron ore with massive texture. (f) Drill core photograph of amphibolite. (g) Drill core photograph of granite. (h) Drill core photograph of gneiss.

Figure 2.3. Representative photomicrographs of the Yishui BIF and associated rocks. (a) Alternating amphibole–, magnetite–, and quartz–rich microband of iron ore (cross polarized light). (b) Amphibole band with a close relationship between magnetite and epidote (cross polarized light). (c–d) Presence of calcite, hematite, quartz, and magnetite in iron ore (cross polarized light). (e) Needle–shaped iron oxide (hematite) and adjacent calcite (cross polarized light). (f) Chlorite in iron ore (plane polarized light). (g) Magnetite grains in iron ore (reflected light). (h–i) Amphibolite

consisting of amphibole, plagioclase with minor chlorite, biotite, and magnetite. (j) Granite consisting of quartz, K-feldspar, plagioclase, amphibole, and biotite. (k-l) Gneiss with mineral assemblage of quartz, plagioclase, and biotite. Mt: magnetite; Cc: calcite; Hem: hematite; Amp: amphibole; Bt: biotite; Chl: chlorite; Pl: plagioclase; Q: quartz; K-feld: K-feldspar.

Figure 2.4. $\text{Al}_2\text{O}_3 + \text{TiO}_2\text{-SiO}_2\text{-Fe}_2\text{O}_3$ diagram for iron ores from the Yishui BIF (Gross and McLeod, 1980; Lan et al., 2014b).

Figure 2.5. PAAS-normalized REY pattern of iron ores of the Yishui BIF. The average of the Archean BIFs in the NCC (Lan et al., 2014b) is plotted for comparison. The range of values for the Yishui BIF is shown as gray shadow and the average values are marked with a red circle.

Figure 2.6. $(\text{Ce}/\text{Ce}^*)_{\text{SN}}$ vs. $(\text{Pr}/\text{Pr}^*)_{\text{SN}}$ diagram for the Yishui BIF (Bau and Dulski, 1996). In this diagram, $(\text{Ce}/\text{Ce}^*)_{\text{SN}}$ and $(\text{Pr}/\text{Pr}^*)_{\text{SN}}$ are calculated from $\text{Ce}_{\text{SN}}/(0.5 * (\text{La}_{\text{SN}} + \text{Pr}_{\text{SN}}))$ and $\text{Pr}_{\text{SN}}/(0.5 * (\text{Ce}_{\text{SN}} + \text{Nd}_{\text{SN}}))$, respectively.

Figure 2.7. $\text{Al}/(\text{Al} + \text{Fe} + \text{Mn})$ vs. Fe/Ti diagram (Boström, 1973) for the Yishui BIF.

Figure 2.8. Archean upper crust-normalized diagram. The normalized values are from Taylor and McLennan (1985). The range of values for the Yishui BIF is shown as gray shadow and the average values are marked with a red circle.

Figure 2.9. Covariant relationship between Y/Ho and Zr (ppm) for the Yishui BIF.

Figure 2.10. (a) Al_2O_3 vs. SiO_2 diagram (Wonder et al., 1988), (b) Al-Fe-Mn (wt.%) ternary diagram (Boström, 1973), and (c) WMS-normalized La and Gd anomaly diagram (Alexander et al., 2008) for the Yishui BIF.

Figure 2.11. Conservative mixing line of high-temperature hydrothermal fluid (Bau and Dulski, 1999) and seawater (Alibo and Nozaki, 1999). (a) Eu/Sm versus Y/Ho, (b) Sm/Yb versus Y/Ho, and (c) Eu/Sm versus Sm/Yb (Alexander et al., 2008) for modern hydrogenetic Fe–Mn crust and Pongola IF (Alexander et al., 2008), Kuruman IF (Bau and Dulski, 1996), Isua IF (Bolhar et al., 2004), Gongchangling BIF (Sun et al., 2014a), and Wadi Karim and Um Anab BIFs (Basta et al., 2011).

Figure 2.12. Metamorphic P–T paths of various basement rocks of the EB of the NCC (Zhao et al., 1998). 1: Western Shandong; 2: Eastern Hebei; 3: Western Liaoning; 4: Northern Lianing; 5: Eastern Shandong; 6: Miyun–Chengde; 7: Southern Jilin; 8: Yishui County (study area).

Figure 2.13. A cartoon illustrating of a possible genetic model of Algoma-type Yishui BIF related to a mantle plume.

Figure 3.1. (a) Schematic tectonic map of the North China Craton (Zhao et al., 2005). (b) Geological sketch map of the Western Shandong Province (Wan et al., 2011). The locations of study area with comparable data from previous studies (Polat et al., 2006; Cheng and Kusky, 2007; Wang et al., 2013; Li et al., 2016) are marked red star. (c) Geological map of the Yishui BIF and Yishui amphibolite (Lai and Yang, 2012a). Abbreviations: Fm.=formation.

Figure 3.2. (a) Field photograph from the Yishui BIF and Yishui amphibolite. (b–d) Hand specimen photographs of amphibolites.

Figure 3.3. Representative photomicrographs of the Yishui amphibolites. Abbreviations: Amp=amphibole; Hbl=hornblende; Chl=chlorite; Bt=biotite; Q=quartz; Pl=plagioclase; Mag=magnetite; Chp=chalcopyrite; Py=pyrite.

Figure 3.4. Chondrite-normalized REE patterns and primitive mantle-normalized multielement spider diagram of the Yishui amphibolites (a, b), enriched basalt (c, d) and metavolcanic rocks (e, f) from WSP. Chondrite and primitive mantle normalization values are from Sun and McDonough (1989). Enriched basalt and metavolcanic rocks vales are from Wang et al. (2013) and Li et al. (2016), respectively. Oceanic island basalt (OIB), enriched mid-ocean ridge basalt (E-MORB) and normal mid-ocean ridge basalt (N-MORB) (Sun and McDonough, 1989) are plotted together for comparison.

Figure 3.5. Chondrite-normalized REE patterns and primitive mantle-normalized multi-element spider diagram of the amphibolites (a, b), komatiites (c, d) from TG (Polat et al., 2006). The normalized values and comparable data are same with Figure 3.4.

Figure 3.6. Geochemical classification diagram of Nb/Y vs. $Zr/TiO_2 \cdot 0.0001$ (Floyd and Winchester, 1975).

Figure 3.7. Ta/Yb vs. Th/Yb projections (Pearce, 1982).

Figure 3.8. Nb/Yb vs. TiO_2/Yb and diagram with the mantle array (Pearce, 2008). The line indicates the melting model calculated by Pearce (2008) for a primitive mantle source at given pressures.

Figure 3.9. Nb–Zr–Y (Meschede, 1986) tectonic setting discrimination diagram.

Figure 3.10. A simplified schematic sketch illustrating a possible tectonic model of a mantle plume based on geochemical data.

Figure 4.1. (a) Tectonic map of the North China Craton (NCC), revised from Zhao et al. (2005). Red square indicate location of Yuanjiacun BIF. The Archean to Proterozoic basement are widely distributed in the Eastern and Western Block of NCC. The Trans North China orogen is covered Paleoproterozoic

basement. (b) Simplified geological map of the Luliang Complex, modified after Zhao et al. (2008).

Figure 4.2. Yuanjiacun BIF consisting of alternating Fe-rich layer and Si-rich layer (a) under cross polarized light and (b) open polarized light. (Magnetite; Mag, Hematite; Hem, Pyrite; Py, Quartz; Qz, Biotite; Bt, Amphibole; Amp). (c) Magnetite occurred as a representative ore mineral (reflected light) with (d) minor pyrite (reflected light). (e) Magnetite and hematite are identified in the thin section under reflecting microscope of Raman. (f) Magnetite and hematite were simultaneously shown in magnetite.

Figure 4.3. Raman analysis position (a, c, e) and Raman spectrum (b, d, f) of the magnetite and hematite from Yuanjiacun BIF.

Figure 4.4. Ce/Ce_{PAAS}^{\square} versus Pr/Pr_{PAAS}^{\square} discrimination diagram for iron ores of Yuanjiacun BIF. Field I: neither Ce_{PAAS} nor La_{PAAS} anomaly; field II a: positive La_{PAAS} anomaly, no Ce_{PAAS} anomaly; field II b: negative La_{PAAS} anomaly, no Ce_{PAAS} anomaly; field IIIa: positive Ce_{PAAS} anomaly; field IIIb: negative Ce_{PAAS} anomaly. Red circles indicate iron ores from this study and blue circles comes from Hou et al. (2014) and Wang et al. (2014).

Figure 5.1. (a) Geological map of the North China Craton (Zhao et al., 2005). Simplified geological map of the (b) Huoqiu BIF (Xue et al., 2014), (c) Yishui BIF (Cao et al., 1996) and (d) Yuanjiacun BIF (Wan et al., 2010).

Figure 5.2. Photographs of iron ores from Yishui BIF (a–c) (Moon et al., 2017), Huoqiu BIF (d–f) and Yuanjiacun BIF (g–i). White lines indicate the individual bands.

Figure 5.3. Photomicrographs of iron ore from Yishui BIF (a–c), Huoqiu BIF (d–f) and Yuanjiacun BIF (g–i). The mineral abbreviations are listed as follows:

Mt–magnetite, Amp–amphibole, Hem–hematite, Q–quartz, Py–pyrite, Mus–muscovite.

Figure 5.4. Post Archean Average Shale normalized REY (REE + Y) patterns of the iron ores from Yishui, Huoqiu, Yuanjiacun BIFs; the values of the Post Archean Average Shale based on McLennan (1989). The blue and yellow fields are the compositional ranges of iron ores from Huoqiu and Yuanjiacun BIFs, respectively. Literature whole–rock REY compositions of Huoqiu and Yuanjiacun BIFs are from Hou et al. (2014) and Yang et al. (2014).

Figure 5.5. Bulk continental crust normalized trace elements in magnetite from (a) Yishui BIF, (b) Huoqiu BIF and (c) Yuanjiacun BIF with average of Algoma– and Superior–type BIFs. The red and blue fields are the compositional ranges of magnetites from Algoma– and Superior–type BIFs, respectively. Bulk continental crust values used for normalization are from (Rudnick and Gao, 2003). Elements are ordered with an increase in compatibility into magnetite to the right (Dare et al., 2012).

Figure 5.6. Time–resolved analytical signals of an LA–ICP–MS analysis across a magnetite grain from (a) Yishui BIF and (b) Huoqiu BIF and (c) Yuanjiacun BIF.

Figure 5.7. Binary diagram of (a) V vs. Ti (Knipping et al., 2015). The dark grey and light grey areas indicate magnetite of igneous and hydrothermal origin, respectively (Nadoll et al., 2014). Plots of chemical discrimination diagram for magnetite of (b) Ti+V vs. Al+Mn. The reference fields are from Dupuis and Beaudoin (2011) and Nadoll et al. (2014). The values are shown in weight percent (wt. %). Plot of (c) Ni vs. V for magnetites (Zhao et al., 2016).

Figure 5.8. Plots for (a) Ga, (b) Al, (c) Ni, (d) V and (e) Ti concentration in magnetites of studied BIFs. The error bars represent the maximum and minimum contents of each element in magnetite from each BIF. The average values of Algoma- and Superior-type BIFs are shown as red and blue lines, respectively. The Wadi Karim and Um Anab BIFs in 6 are separately plotted. The BIFs are ordered based on their ages. 1: Nuvvuagittuq BIF (3.75 Ga; Mloszewska et al., 2012); 2: Magin BIF (2.6–2.8 Ga; Duparc et al., 2016); 3: Izok Lake BIF (2.58–2.68 Ga; Makvandi et al., 2016); 4: Randalls (2.66 Ga; Steadman et al., 2014); 5: Yishui BIF (2.6 Ga; this study); 6: Wadi Karim and Um Anab BIFs (Neoproterozoic; Basta et al., 2011); 7: Houqui BIF (2.6–2.8 Ga; this study); 8: Yuanjiacun BIF (2.3–2.2 Ga; this study); 9: Sokoman BIF (1.88 Ga; Chung et al., 2015). The symbols as for Figure 5.7.

List of Tables

Table 2.1. Major element compositions of the Yishui BIF and representative BIF values (wt.%).

Table 2.2. Trace element and REE composition of the Yishui BIF and Archean BIFs of the NCC (ppm).

Table 4.1. EPMA data of the magnetite from Yuanjiacun BIF (wt.%)

Table 4.2. Pr/Pr* and Ce/Ce* data of the iron ores from Yuanjiacun BIF.

Table 5.1. The average major elements (wt.%) of the iron ores from the BIFs with representative values.

Table 5.2. Trace and rare earth elements (ppm) of iron ores from the BIFs.

Table 5.3. Average of trace elements (ppm) of magnetite from the BIFs.

Chapter 1. Introduction

Precambrian banded iron formations (BIFs) provide valuable information about the environment of the early Earth and evolutionary processes of chemical sedimentary rocks deposited in marine environments (Isley and Abbott, 1999). This study uses James (1954)'s definition of an iron formation as “a chemical sediment, typically thin bedded or laminated, containing 15% or more iron of sedimentary origin, commonly but not necessarily containing layers of chert”. For these reasons, BIFs have been used as a proxy to evaluate the environment of the early Earth, the evolution of the crust, contemporaneous atmospheric oxygenation, oceanic conditions and the presence of photosynthetic bacteria (Klein, 2005). They can also be used as classification criteria for the Archean and Proterozoic (Bekker et al., 2010; Han et al., 2014; Huston and Logan, 2004; Lascelles, 2007; Sun et al., 2014a; Sun et al., 2014b; Tang et al., 2013). The formation mechanisms of Precambrian BIFs are still unknown although they attract considerable interest. REY in BIFs have been studied as geochemical indicators since 1960. They provide information about the physicochemical conditions during BIF precipitation (Bau and Möller, 1992; Han et al., 2014; Kato et al., 1996; Sun et al., 2014a; Sun et al., 2014b). Many researchers have attempted to develop genetic models for BIFs based on petrological, mineralogical, geochemical, geochronological and tectonic data (Basta et al., 2011; Bolhar et al., 2005; Han et al., 2014; Holland, 1973; Huston and Logan, 2004; Isley and Abbott, 1999; Khalil et al., 2015; Lan et al., 2014; Sun et al., 2014a; Sun et al., 2014b; Yang et al., 2015; Zhu et al., 2015). Two main types of Precambrian BIFs are proposed by Gross (1980) based on related depositional settings and related rock associations, which are Algoma-type BIFs and Superior-type BIFs. The

Algoma-type BIFs are closely related to volcanic activity and interbedded with volcanic rocks, whereas Superior-type BIFs have formed in shallow marine environments at continental margin settings and are associated with quartzite, dolomite and black shale (Klein, 2005). Hence, the close relationship between the BIFs and the associated wall rock can be considered as a valuable proxy for understanding not only the reconstruction of the formation mechanism of BIFs but also the tectonic evolution of Archean cratons. Furthermore, geochemical interpretation of Archean rocks is critical for the reconstruction of early Earth's crustal evolution and the nature of the Earth's interior (Ilnicki, 2012; Shervais, 1982).

As explained above, studies of BIFs were typically conducted assuming a formation model based on the formation age and mechanism (Basta et al., 2011; Bolhar et al., 2005; Han et al., 2014; Huston and Logan, 2004; Isley and Abbott, 1999; Khalil et al., 2015; Moon et al., 2017; Sun et al., 2014a; Sun et al., 2014b; Yang et al., 2015; Zhu et al., 2015). Recently, the study area has changed to study the crystal shape, grain size and the lattice of magnetite as a representative ore mineral in BIFs (Li et al., 2014). Magnetite is mechanically and chemically stable during erosion, weathering, transportation, and metamorphism (Grigsby, 1990; McClenaghan, 2005). Various cations (Mg, Al, Sc, Ti, V, Cr, Mn, Co, Ni, Zn, Ga, Ge, Y, Hf, Nb, Mo, Ta, and Zr) can enter the cubic spinel structure of magnetite. Ppm to sub-ppm trace element concentrations of magnetite were determined by laser ablation inductively coupled plasma mass spectrometry (LA-ICP-MS). Magnetite's geochemistry is controlled by physicochemical conditions such as fluid composition, temperature, pressure, oxygen, sulfur fugacity and fluid-host rock interaction (Liu et al., 2015; Nadoll et al., 2012) and is a reflection of the

ore–fluid source and ore–forming processes (Huang et al., 2013). For these reasons, magnetite geochemistry enables us to constrain the physicochemical controlling factors and understand the depositional condition of BIFs (Dupuis and Beaudoin, 2011; Li et al., 2017; Nadoll et al., 2014; Nadoll et al., 2012; Razjigaeva and Naumova, 1992). In addition, we conducted Raman spectroscopic analysis on the magnetite. Each mineral has a strong spectral band at its inherent Raman shift depending on the constituent elements and molecular structure. Hence, we evaluated the degree of oxidation on the magnetite (transformed magnetite to hematite) through Raman analysis.

From these perspective, the main purposes of this Ph.D. thesis are identification of genesis of Algoma–type Yishui BIF, petrogenesis of Yishui amphibolite, the temporal and spatial relationship between Yishui amphibolite and Yishui BIF, suitable tectonic model in Archean NCC, relationship between the formation of timing for the Superior–type Yuanjiacun BIF and the GOE and genetic conditions of BIFs on magnetite chemistry. The highlight of these thesis include the following.

- In Chapter 2, the formation mechanism of Algoma–type Yishui BIF using iron ore is identified. A suitable tectonic model for explaining genesis of Yishui BIF and crustal evolution of NCC is proposed.
- In Chapter 3, geochemical signatures of Archean rock in NCC are characterized. The temporal and spatial relationship between the Yishui BIFs and wall rock (amphibolite) are revealed. The mantle plume model is proposed, which can explain the geochemical signatures of both Archean rocks and Yishui BIF deposition.

- In Chapter 4, the relationship between the timing for the formation of Yuanjiaocun BIF and the coeval oxygen fugacity (fO_2) through Raman analysis of magnetite as a representative ore mineral in the BIF are investigated.
- In Chapter 5, we provide results of magnetite trace elemental features from two representative types of BIF which are Algoma- and Superior-type BIFs in the world, with aims to understanding relation between magnetite geochemistry and the type of BIFs. Systematic differences in trace element composition of magnetite between Algoma- and Superior-type BIFs due to differences in their depositional environments are demonstrated.

References

- Basta, F. F., Maurice, A. E., Fontboté, L., and Favarger, P.-Y., 2011, Petrology and geochemistry of the banded iron formation (BIF) of Wadi Karim and Um Anab, Eastern Desert, Egypt: implications for the origin of Neoproterozoic BIF: *Precambrian Research*, v. 187, no. 3, p. 277-292.
- Bau, M., and Möller, P., 1992, Rare earth element fractionation in metamorphogenic hydrothermal calcite, magnesite and siderite: *Mineralogy and Petrology*, v. 45, no. 3-4, p. 231-246.
- Bekker, A., Slack, J. F., Planavsky, N., Krapež, B., Hofmann, A., Konhauser, K. O., and Rouxel, O. J., 2010, Iron formation: the sedimentary product of a complex interplay among mantle, tectonic, oceanic, and biospheric processes: *Economic Geology*, v. 105, no. 3, p. 467-508.
- Bolhar, R., Van Kranendonk, M. J., and Kamber, B. S., 2005, A trace element study of siderite–jasper banded iron formation in the 3.45 Ga Warrawoona Group, Pilbara Craton—formation from hydrothermal fluids and shallow seawater: *Precambrian Research*, v. 137, no. 1, p. 93-114.
- Dupuis, C., and Beaudoin, G., 2011, Discriminant diagrams for iron oxide trace element fingerprinting of mineral deposit types: *Mineralium Deposita*, v. 46, no. 4, p. 319-335.
- Grigsby, J. D., 1990, Detrital magnetite as a provenance indicator: *Journal of Sedimentary Research*, v. 60, no. 6.
- Gross, G. A., 1980, A classification of iron formations based on depositional environments: *The Canadian Mineralogist*, v. 18, no. 2, p. 215-222.
- Han, C., Xiao, W., Su, B., Chen, Z., Zhang, X., Ao, S., Zhang, J., Zhang, Z., Wan, B., and Song, D., 2014, Neoproterozoic Algoma-type banded iron formations from Eastern Hebei, North China Craton: SHRIMP U-Pb age, origin and tectonic setting: *Precambrian Research*, v. 251, p. 212-231.
- Holland, H. D., 1973, The oceans; a possible source of iron in iron-formations: *Economic*

- Geology, v. 68, no. 7, p. 1169-1172.
- Huang, X.-W., Zhou, M.-F., Qi, L., Gao, J.-F., and Wang, Y.-W., 2013, Re–Os isotopic ages of pyrite and chemical composition of magnetite from the Cihai magmatic–hydrothermal Fe deposit, NW China: *Mineralium Deposita*, v. 48, no. 8, p. 925-946.
- Huston, D. L., and Logan, G. A., 2004, Barite, BIFs and bugs: evidence for the evolution of the Earth's early hydrosphere: *Earth and Planetary Science Letters*, v. 220, no. 1, p. 41-55.
- Ilnicki, S., 2012, Amphibolites from the Szklarska Poręba hornfels belt, West Sudetes, SW Poland: magma genesis and implications for the break-up of Gondwana: *International Journal of Earth Sciences*, v. 101, no. 5, p. 1253-1272.
- Isley, A. E., and Abbott, D. H., 1999, Plume-related mafic volcanism and the deposition of banded iron formation: *Journal of Geophysical Research: Solid Earth* (1978–2012), v. 104, no. B7, p. 15461-15477.
- James, H. L., 1954, Sedimentary facies of iron-formation: *Economic Geology*, v. 49, no. 3, p. 235-293.
- Kato, Y., Kawakami, T., Kano, T., Kunugiza, K., and Swamy, N. S., 1996, Rare-earth element geochemistry of banded iron formations and associated amphibolite from the Sargur belts, south India: *Journal of Southeast Asian Earth Sciences*, v. 14, no. 3–4, p. 161-164.
- Khalil, K. I., El-Shazly, A. E., and Lehmann, B., 2015, Late Neoproterozoic banded iron formation (BIF) in the central Eastern Desert of Egypt: Mineralogical and geochemical implications for the origin of the Gebel El Hadid iron ore deposit: *Ore Geology Reviews*, v. 69, p. 380-399.
- Klein, C., 2005, Some Precambrian banded iron-formations (BIFs) from around the world: Their age, geologic setting, mineralogy, metamorphism, geochemistry, and origins: *American Mineralogist*, v. 90, no. 10, p. 1473-1499.
- Lan, T.-G., Fan, H.-R., Santosh, M., Hu, F.-F., Yang, K.-F., and Liu, Y., 2014, U–Pb zircon chronology, geochemistry and isotopes of the Changyi banded iron formation in the eastern Shandong Province: Constraints on BIF genesis and

- implications for Paleoproterozoic tectonic evolution of the North China Craton: *Ore Geology Reviews*, v. 56, p. 472-486.
- Lascelles, D. F., 2007, Black smokers and density currents: a uniformitarian model for the genesis of banded iron-formations: *Ore Geology Reviews*, v. 32, no. 1, p. 381-411.
- Li, H., Zhai, M., Zhang, L., Yang, Z., Kapsiotis, A., Zhou, Y., He, J., Wang, C., and Liang, J., 2014, Mineralogical and microfabric characteristics of magnetite in the Wuyang Precambrian BIFs, southern North China Craton: Implications for genesis and depositional processes of the associated BIFs: *Journal of Asian Earth Sciences*, v. 94, p. 267-281.
- Li, Y.-L., Konhauser, K. O., and Zhai, M., 2017, The formation of magnetite in the early Archean oceans: *Earth and Planetary Science Letters*, v. 466, p. 103-114.
- Liu, P.-P., Zhou, M.-F., Chen, W. T., Gao, J.-F., and Huang, X.-W., 2015, In-situ LA-ICP-MS trace elemental analyses of magnetite: Fe–Ti–(V) oxide-bearing mafic–ultramafic layered intrusions of the Emeishan Large Igneous Province, SW China: *Ore Geology Reviews*, v. 65, p. 853-871.
- McClenaghan, M. B., 2005, Indicator mineral methods in mineral exploration: *Geochemistry: Exploration, Environment, Analysis*, v. 5, no. 3, p. 233-245.
- Moon, I., Lee, I., and Yang, X., 2017, Geochemical constraints on the genesis of the Algoma–type banded iron formation (BIF) in Yishui County, Western Shandong Province, North China Craton: *Ore Geology Reviews*.
- Nadoll, P., Angerer, T., Mauk, J. L., French, D., and Walshe, J., 2014, The chemistry of hydrothermal magnetite: a review: *Ore Geology Reviews*, v. 61, p. 1-32.
- Nadoll, P., Mauk, J. L., Hayes, T. S., Koenig, A. E., and Box, S. E., 2012, Geochemistry of magnetite from hydrothermal ore deposits and host rocks of the Mesoproterozoic Belt Supergroup, United States: *Economic Geology*, v. 107, no. 6, p. 1275-1292.
- Razjigaeva, N., and Naumova, V., 1992, Trace element composition of detrital magnetite from coastal sediments of northwestern Japan Sea for provenance study: *Journal of Sedimentary Research*, v. 62, no. 5, p. 802-809.

- Shervais, J. W., 1982, Ti-V plots and the petrogenesis of modern and ophiolitic lavas: *Earth and planetary science letters*, v. 59, no. 1, p. 101-118.
- Sun, X.-H., Zhu, X.-Q., Tang, H.-S., Zhang, Q., and Luo, T.-Y., 2014a, The Gongchangling BIFs from the Anshan–Benxi area, NE China: Petrological–geochemical characteristics and genesis of high-grade iron ores: *Ore Geology Reviews*, v. 60, p. 112-125.
- Sun, X.-H., Zhu, X.-Q., Tang, H.-S., Zhang, Q., Luo, T.-Y., and Han, T., 2014b, Protolith reconstruction and geochemical study on the wall rocks of Anshan BIFs, Northeast China: Implications for the provenance and tectonic setting: *Journal of Geochemical Exploration*, v. 136, p. 65-75.
- Tang, H.-S., Chen, Y.-J., Santosh, M., Zhong, H., and Yang, T., 2013, REE geochemistry of carbonates from the Guanmenshan Formation, Liaohe Group, NE Sino-Korean Craton: implications for seawater compositional change during the Great Oxidation Event: *Precambrian Research*, v. 227, p. 316-336.
- Yang, X.-Q., Zhang, Z.-H., Duan, S.-G., and Zhao, X.-M., 2015, Petrological and geochemical features of the Jingtieshan banded iron formation (BIF): A unique type of BIF from the Northern Qilian Orogenic Belt, NW China: *Journal of Asian Earth Sciences*.
- Zhu, M., Dai, Y., Zhang, L., Wang, C., and Liu, L., 2015, Geochronology and geochemistry of the Nanfen iron deposit in the Anshan-Benxi area, North China Craton: Implications for ~ 2.55 Ga crustal growth and the genesis of high-grade iron ores: *Precambrian Research*.

Chapter 2. Geochemical constraints on the genesis of the Algoma–type banded iron formation (BIF) in Yishui County, Western Shandong Province, North China Craton

Abstract

The Yishui iron deposit is a typical Algoma–type banded iron formation (BIF) located in Yishui County, Taishan Group, Shandong Province in the Eastern Block (EB) of the North China Craton (NCC). The BIF is interlayered with amphibolite, migmatitic granite, gneiss, and schist. Integrated petrological, mineralogical, and geochemical interpretations of the iron ores were used to reconstruct the genesis of the Yishui BIFs and their tectonic evolution. The iron ore samples were collected from surface outcrops. Banding textures are not always present in the iron ores because the BIF experienced complex high–grade metamorphism after precipitation. Interpretations of the major elements and rare earth elements plus yttrium (REY) data of the iron ores suggests that the ore–forming materials of the Yishui BIF precipitated from a mixture of seawater and high–temperature hydrothermal fluids (< 0.1%) in a submarine environment with volcanic activity under relatively low oxygen conditions. Large amounts of iron and silica

were produced under these conditions. The main compositions of SiO_2 and $\text{Fe}_2\text{O}_3^{\text{T}}$ ($\text{SiO}_2 + \text{Fe}_2\text{O}_3^{\text{T}} = 85.8\text{--}95.8$ wt.%) are consistent with the major minerals, such as quartz and iron oxide, which represent chemical precipitates. Chlorite, amphibole, plagioclase, biotite, and calcite are present as minor minerals. The low contents of TiO_2 (0.01 to 0.09 wt.%), Al_2O_3 (0.42 to 1.18 wt.%), and high field strength elements (HFSEs) indicate little to no detrital assimilation, which implies that the iron ores preserved their original geochemical signatures. Based on geochemical interpretations, we conclude that the Yishui BIF can be explained by a mantle plume model that describes not only the tectonic evolution but also the sources of iron and silica of the Yishui BIF.

2.1. Introduction

Precambrian banded iron formations (BIFs) provide valuable information about the environment of the early Earth and evolutionary processes of chemical sedimentary rocks deposited in marine environments (Isley and Abbott, 1999). The definition used in this study follows that of James (1954) who defined an iron formation as “a chemical sediment, typically thin bedded or laminated, containing 15% or more iron of sedimentary origin, commonly but not necessarily containing layers of chert”.

The BIFs formed in the Precambrian, especially between $\sim 3.8\text{--}1.8$ Ga, with a peak in the Neoproterozoic and reappearance in the Neoproterozoic (Klein, 2005; Bekker et al., 2010). Precambrian BIFs can be classified as Superior– and Algoma–type BIFs based on their depositional environment and associated volcanic rocks. Superior–type BIFs

formed in shallow marine environments over large areas under stable conditions such as continental shelves of passive tectonic margins or in intracratonic basins with no coeval volcanic rocks (González et al., 2009). The representative largest BIF such as Australia Hamersley and South Africa Transvaal iron deposits are included in Superior-type BIFs (Evans et al., 2013; Hagemann et al., 2016). In contrast, Algoma-type BIFs cover smaller areas and are associated with coeval volcanic rocks (Gross and McLeod, 1980; Li et al., 2014b; Yang et al., 2015). They are mainly hosted by Archean greenstone belts (Zhai and Santosh, 2011). Most Algoma-type BIFs have been severely deformed and have undergone various degrees of metamorphism. As a result, the banding is not preserved in all cases (Klein, 2005; Bekker et al., 2010). The different depositional environments of BIFs are genetically linked to compositional changes of the atmosphere, hydrosphere, and biosphere (Bekker et al., 2010; Han et al., 2014; Sun et al., 2014a).

Based on these reasons, BIFs have been used as proxy to evaluate the environment of the early Earth, evolution of the crust, contemporaneous atmospheric oxygenation, oceanic conditions, and photosynthetic bacteria (Klein, 2005). They can also be used as classification criteria for the Archean and Proterozoic (Huston and Logan, 2004; Lascelles, 2007; Bekker et al., 2010; Tang et al., 2013a; Han et al., 2014; Sun et al., 2014a; Sun et al., 2014b).

The BIFs are major sources of iron in China (64% of the total iron reserves) and are widely distributed in the North China Craton (NCC). Most BIFs in China are classified as Algoma-type BIFs, whereas relatively few BIFs are Superior-type BIFs. Low-grade iron ores dominate most of the BIFs in China ($20\% \leq \text{TFe} < 50\%$). Unlike other countries, only 2% of the BIFs in China contain high-grade ores ($\text{TFe} \geq 50\%$). The

NCC is one of the oldest cratons in the world (~3.8 Ga); it experienced complex and high-grade metamorphism and magmatism (Zhai and Santosh, 2011). Geological events of the Earth's history are closely related to metallogenic deposits (Zhai and Santosh, 2013; Lan et al., 2014b). The Neoproterozoic is considered to be a relatively important period for the formation of Algoma-type BIFs in the NCC (Zhai and Santosh, 2013). Most of the BIFs in the NCC are located in the eastern Liaoning, eastern Hebei, northern Shanxi, western Anhui, southwestern Henan, and western Shandong provinces (Zhang et al., 2012).

Although being of great interest, the formation mechanisms of Precambrian BIFs are still unknown. Rare earth elements plus yttrium (REY) in BIFs have been studied as geochemical indicators since 1960. They provide information about the physicochemical conditions during BIF precipitation (Bau and Möller, 1992; Kato et al., 1996; Han et al., 2014; Sun et al., 2014a; Sun et al., 2014b). Many researchers attempted to develop genetic models for BIFs based on petrological, mineralogical, geochemical, geochronological, and tectonic data (Holland, 1973; Isley and Abbott, 1999; Huston and Logan, 2004; Bolhar et al., 2005; Basta et al., 2011; Han et al., 2014; Lan et al., 2014b; Sun et al., 2014a; Sun et al., 2014b; Khalil et al., 2015; Yang et al., 2015; Zhu et al., 2015).

In this study, the Algoma-type BIF in Yishui County (called the Yishui BIF) was investigated. The aim of this paper is to characterize the Yishui BIF by comparing it to other representative BIFs in China and around the world using the major element, trace element, and REY compositions of the iron ores. The integration of lithology, structural geology, geochemistry, and geochronology data is beneficial for the

reconstruction of past geological conditions and provides information about the genesis of the Yishui BIF. The geochronology data were obtained from Lai and Yang (2012b). The new data reported in this paper will provide an advanced understanding of the genesis of Yishui BIF and the evolution of the NCC in the Neoproterozoic.

2.2. Geological setting of the region and deposit

2.2.1. Regional Geology

The tectonic framework of China consists of the three cratonic blocks (NCC, South China Craton, and Tarim Block) along several orogenic belts (Himalaya, Kunlun, Altyn Tagh, Qilian, Tainshan, the western Altai, Junggar, and Qinling–Tongbai–Hong’an–Dabie–Sulu, etc.). The SCC is composed of the Late Archean to Paleoproterozoic Yangtze and Paleoproterozoic Cathaysia blocks. The Tarim Block has a Late Archean to Paleoproterozoic basement (Zhao et al., 2001; Zheng et al., 2013a). The NCC consists of Archean to Paleoproterozoic basement that is overlain by unmetamorphosed Mesoproterozoic to Cenozoic rocks. It covers an area of 1.5×10^6 km² and is the largest craton in the world. More than 80% of Late Archean basement is widespread in the NCC (Zhao et al., 2001; Zhao and Zhai, 2013; Zheng et al., 2013b). The basement rocks in the NCC formed during two periods: 2.8–2.7 Ga and 2.6–2.5 Ga (Zhao and Zhai, 2013). The region comprises tonalite–trondhjemite–granodiorite (TTG) gneiss, granite, migmatite, amphibolite, greenschist, BIF, high–pressure granulites, ultrahigh–temperature metamorphic rocks, various schist greenstone belts, and mafic–ultramafic rocks (Hu et al., 2005; Zhao et al., 2005; Wu et al., 2012). The NCC has

experienced five major tectonic events: (1) Neoproterozoic crustal growth and stabilization; (2) Paleoproterozoic rifting, subduction, accretion, and collision with imprints of the Great Oxidation Event (GOE); (3) Late Paleoproterozoic–Neoproterozoic multistage rifting; (4) Paleozoic orogenesis at the margins of the craton; and (5) Mesozoic extensional tectonics associated with lithospheric thinning and decratonization (Zhai and Santosh, 2011; Geng et al., 2012; Zhai and Santosh, 2013; Fan et al., 2014). These five geotectonic events are closely associated with six major mineral systems: (1) Archean BIF system, (2) Paleoproterozoic Cu–Pb–Zn and Mg–B system, (3) Mesoproterozoic REE–Fe–Pb–Zn system, (4) Paleozoic orogenic Cu–Mo system, (5) Mesozoic intracontinental Au, Ag–Pb–Zn, and Mo system, and (6) Fe mineralization system. The spatial distribution and formation processes of mineral deposits have regular patterns over the Earth’s history. The NCC is therefore considered to be an ideal location to explain the relationships between geological events and ore mineralization (Zhai and Santosh, 2013).

The NCC is divided into the Eastern Block (EB), Western Block (WB), and Trans–North China Orogen (Figure 2.1a). The Trans–North China Orogen divides the EB and WB (Liu et al., 1992; Zhao et al., 2003; Zhao et al., 2005; Wu et al., 2012). The EB of the NCC formed in the Archean and is composed of high–grade terranes and low–grade granite–greenstone belts. The southern Liaoning, western Liaoning, eastern Hebei, Miyun, western Shandong, and eastern Shandong provinces are distributed in the EB; these regions experienced greenschist to granulite metamorphism (Wu et al., 2012; Wu et al., 2013b). The EB mainly consists of TTG gneiss and mafic–ultramafic igneous rock that formed at ~2.7–2.6 Ga; diorite, granodiorite, monzogranite, high–K granite, and

charnockite that formed at ~2.52 Ga; and minor bimodal volcanic and supracrustal rocks (Zhao et al., 1998; Yang et al., 2008). The metamorphic evolution of the EB followed an anticlockwise P–T path implying the intrusion and underplating of large amounts of mantle–derived magma (Zhao et al., 1998).

The western Shandong Province (WSP) makes up the largest part of the EB and is mostly composed of the low–grade Luxi Granite–Greenstone Terrane and high–grade Yishui Terrane (Figure 2.1b). The Yishui Terrane trends NE–SW (Wu et al., 2013b). The WSP covers more than 15,000 km² and is bounded by the Liaochen–Lankao and Yi–Shu faults. The basement consists of Archean granite–greenstone belts. Some of the Archean rocks in Yishui County were exposed due to uplift or exhumation along the Tancheng–Lujiang fault. Igneous plutons make up approximately 70% of the exposed rocks (Wu et al., 2012). The WSP is composed of amphibolite, mafic granulite, minor magnetite quartzite, migmatite, and Al–rich metapelite (Hu et al., 2005; Wu et al., 2012). The Early to Late Neoproterozoic supracrustal rocks in the WSP include metasedimentary and minor BIF and volcanic rocks. The WSP granite–greenstone belts preserved the signatures of Neoproterozoic geological events. Significant tectonothermal events that occurred in the WSP at ~2.7 and ~2.5 Ga have been identified in previous studies (Wan et al., 2011; Wan et al., 2012b).

The Taishan Group makes up a large part of the supracrustal association in the WSP. The Taishan Group formed in the Early Neoproterozoic (2.8 to 2.7 Ga) and experienced upper greenschist to amphibolite facies metamorphism. It is composed of three formations, the Yanlingguan, Shancaoyu, and Liuhang formations. These formations extend from northeast to southwest (Wan et al., 2011; Wan et al., 2012b;

Wang et al., 2013).

The Liuhang Formation is composed of amphibolite, volcano–sedimentary rock, and detrital material and is divided into a lower part and an upper part. The lower part contains metabasalt with a relict pillow structure and the upper part comprises biotite gneiss and metaconglomerate. The supracrustal rock in this formation include fine–grained gneiss, metavolcanic rocks, conglomerates, and BIFs (Wan et al., 2012b). The Yishui BIF is located in Archean basement rock within the Liuhang Formation of the EB. The upper part of the Liuhang Formation formed at 2.6–2.5 Ga (based on zircon age dating of schist) and the lower part formed at ~2.6 Ga (based on zircon age dating of amphibolite; (Lai and Yang, 2012b).

2.2.2. Geology of Yishui BIF

The Algoma–type Yishui BIF is situated in the upper part of the Liuhang Formation of the Taishan Group in the northeastern part of the Yishui County, Shandong Province. The main orebodies are exposed in the Archean Taishan Group (Figure 2.1c). A ductile shear zone is well developed in the basement. Brittle fracture structures in NNE, NE, and NEE directions are intricately developed. The hanging wall of the orebodies is composed of irregular biotite–amphibole–leptynite and plagioclase amphibolite with 1–10 m thick. Locally, the orebodies are in contact with muscovite–quartz–schist. The footwall of the orebodies commonly comprises biotite–amphibole–leptynite. Garnet–biotite–plagioclase–leptynite and felsic pegmatite occur locally. The structures are indicative of the geological relationship between the BIF and wall rocks (Figure 2.2a). Both magnetite– and quartz–bearing amphibolites occur within the mineralized zone,

indicating the close genetic relationship between the BIF and volcanic activity (Lan et al., 2014b; Wang et al., 2015b). Amphibolite (basaltic protolith) related Yishui BIF is considered to be an Algoma-type BIF. Magnetite, pyrite, chalcopyrite, arsenopyrite, and pyrrhotite are dominant ore minerals, whereas quartz, amphibole, plagioclase, biotite, and apatite are gangue minerals. In addition, the dike in country rocks intruded at the late stage of tectonic evolution in this region. Topographically, the study area is inclined from north to south, and the orebodies are irregularly distributed. The orebodies extend over a length of approximately 5000 m and most of them are exposed in outcrops; these are mainly divided into three parts from south to north based on fault structure. The first orebody is situated in the southern part of the ore deposit and is exposed at the surface. The orebody is stratiform or sub-stratiform, extends 2300 m along strike, and extends over 170–1050 m in the dip direction. It is the largest orebody of the Yishui BIF. The center thickness gradually decreases toward the boundary of the orebody. The second orebody occurs in the middle part of the ore deposit with a length of 850 m and extending over approximately 200–430 m in the dip direction. The central orebody corresponds to the thinnest part of the whole ore deposit and becomes thicker toward both boundaries of the orebody. The third orebody is distributed in the northern part of the mining area with 1600 m long, 10–15 m thick, and extends over 220–990 m in the dip direction. The layering structure and surface exposure of the orebody were investigated using structural analysis. The third orebody becomes narrower toward the north and finally disappears. The post-depositional processes (metamorphism or deformation) were accompanied by dislocation of the orebodies on the surface and had influence of continuity of the orebodies (Lai and Yang, 2012b).

2.3. Petrology and mineralogy of the Yishui BIF

Representative rock samples were collected from drill cores and surface outcrops of the Yishui BIF. In this paper, iron ores are defined as $20\% < TFe < 45\%$ following the definition of Sun et al. (2014a). The Yishui BIF is dominated by low-grade iron ore and the orebody is characterized by alternating micro- to macro-scale dark Fe-rich bands and light Si-rich bands (Figure 2.2b). The Fe-rich bands mainly consist of magnetite and amphibole with minor quartz, whereas the Si-rich bands are mainly composed of quartz with minor magnetite and amphibole. The orebody has relatively sharp contact between two layers (Figure 2.2b). Some of the iron ores are characterized by distinctive banding patterns (Figure 2.2c), while others are characterized by massive structure (Figure 2.2d–e). They have shiny textures (Figure 2.2d) and often contain quartz veins (Figure 2.2e). Related wall rocks such as amphibolite (Figure 2.2f), granite (Figure 2.2g) and gneiss (Figure 2.2h) are occurring with the orebody in this study. Amphibolite is dark and dark green in color and has a massive texture. Medium- to coarse-grained granite and gneiss have phaneritic textures.

Based on microscopic analysis, differences in the degree of alteration were observed. Iron ores have simple mineralogical association of major magnetite and quartz with less abundant amphibole (Figure 2.3a). Despite high-grade metamorphism and deformation, the banding texture of the iron ores is well preserved (Figure 2.3a–b). Hematite, pyrite, chlorite, plagioclase, biotite, amphibole, zircon, and calcite occur as minor minerals (Figure 2.3c–f). Amphiboles are well aligned under the microscope (Figure 2.3b). Acicular hematite is a distinctive feature of iron ore (Figure 2.3e).

Magnetite is the representative Fe-bearing mineral of the Yishui BIF (Figure 2.3g). Magnetite appears as a dominant component in magnetite-rich microbands and a minor component of quartz- and amphibole-rich microbands. Both individual grains and granoblastic aggregates of magnetite were observed. The grains are almost anhedral to subhedral with sizes of 40–300 μm . Based on electron microprobe analysis, the magnetites of the Yishui BIF are mainly composed of FeO^{T} (average of 93.69 wt.%), with minor Al_2O_3 (average of 0.08 wt.%) and TiO_2 (average of 0.16 wt.%), close to the ideal FeO^{T} content of magnetite (93.1 wt.%;(Lan et al., 2014b). Quartz is another main mineral and commonly forms quartz-rich microbands, which often do not have notable boundaries between mineral grains. Quartz is also present in amphibole- and magnetite-rich microbands as individual grains or aggregates. The grains tend to be larger in size (190–600 μm) and are subhedral to anhedral. The quartz grains show undulatory extinction. The amphiboles (mainly hornblende and grunerite) are subhedral to anhedral crystals with sizes of 220–480 μm . They compose alternating quartz- and magnetite-rich microbands, which are often intermixed within quartz and amphibole. The secondary minerals are indicative of the influence of alteration and weathering (Alexander et al., 2008). Amphibolite commonly consists of medium- to fine-grained amphibole and plagioclase with less abundant pyroxene, chlorite, quartz, and magnetite (Figure 2.3h–i). The magnetite concentrations in this rock are < 20%. The samples have a weakly developed lineation. Undulose quartz and plagioclase were observed in irregularly shaped grains. The granite is mainly composed of medium- to coarse-grained plagioclase, microcline, K-feldspar, quartz, biotite, and small amount of magnetite and apatite (Figure 2.3j). Gneiss displays a blocky structure and is mainly composed of

medium- to coarse-grained quartz and feldspar and minor amphibole and biotite. Quartz and feldspar grains exhibit undulatory extinction (Figure 2.3k-l). Both granite and gneiss are characterized by granophyric, exsolution, and intergrowth textures.

2.4. Analytical Methods

The major elements (SiO_2 , Al_2O_3 , TiO_2 , $\text{Fe}_2\text{O}_3^{\text{T}}$, MgO , CaO , Na_2O , K_2O , MnO , P_2O_5 , and LOI), trace elements (Th, Ni, Sr, Ba, Zr, Y, Nb, Ti, Tb, and Cr), and REEs (La, Ce, Pr, Nd, Sm, Eu, Gd, Tb, Dy, Ho, Er, Tm, Yb, and Lu) were analyzed at the National Center for Inter-University Research Facilities (NCIRF) at Seoul National University. The major elements of whole rock powder samples were analyzed with a Shimadzu XRF-1700 X-ray fluorescence spectrometer (XRF) using $\text{Li}_2\text{B}_4\text{O}_7$ glass beads. The trace elements and REEs of the whole rock powder samples were analyzed with an Elan 6100 inductively coupled plasma mass spectrometer (ICP-MS). The samples were crushed to 200 mesh. Loss on ignition (LOI) means the total change in weight in percent after burning the powder samples at 950°C . Selected mineral compositions and polished thin sections were examined using a JXA-8900R electron microprobe (EPMA) and SEM-EDS. The analytical errors were smaller than 2% and the beam size was $10\ \mu\text{m}$.

2.5. Results

2.5.1. Iron ore whole rock geochemistry

2.5.1.1. Major element analyses

The major element compositions of the Yishui BIF, Archean BIFs in the NCC, and Algoma- and Superior-type BIFs around the world are listed in Table 2.1. The major

components of the iron ores are SiO_2 and $\text{Fe}_2\text{O}_3^{\text{T}}$ (85.82 to 95.82 wt.%); concentrations of CaO (0.91–6.56 wt.%) and MgO (1.76–3.75 wt.%) are subordinate. The concentrations of K_2O (0.02–0.10 wt.%), TiO_2 (0.01–0.09 wt.%), Na_2O (0.03–0.27 wt.%), and MnO (0.07–0.16 wt.%) are < 1 wt.%. One sample has relatively high concentrations of Al_2O_3 (0.42–0.57 wt.% and 1.18 wt.%). The compositions of the iron ores are comparable to those of Archean BIFs in the NCC and worldwide Algoma– and Superior–type BIFs. All iron ores plot in similar fields in the $\text{Al}_2\text{O}_3 + \text{TiO}_2 - \text{SiO}_2 - \text{Fe}_2\text{O}_3^{\text{T}}$ diagram, suggesting that the chemical composition of the Yishui BIF is nearly identical to that of BIFs around the world (Figure 2.4). The average SiO_2 and $\text{Fe}_2\text{O}_3^{\text{T}}$ concentrations of the Yishui BIF (44.91 wt.% and 47.51 wt.%, respectively) are similar to those of Archean BIFs in the NCC. The iron ores of the Yishui BIF have lower SiO_2 and Al_2O_3 concentrations and higher $\text{Fe}_2\text{O}_3^{\text{T}}$ and MgO concentrations than general Algoma– and Superior–type BIFs. Positive correlations were observed for K_2O vs. Al_2O_3 , K_2O vs. TiO_2 , Al_2O_3 vs. TiO_2 , and $\text{Fe}_2\text{O}_3^{\text{T}}$ vs. MgO . The LOI values vary from 0.10 to 4.65 wt.%.

2.5.1.2. Rare earth element and trace element analyses

The trace elements and REY concentrations of the iron ore are shown in Table 2.2. The physicochemical characteristics of yttrium (Y), such as ionic radius and electronegativity, are similar to that of REEs. Thus, yttrium is occasionally included with the REEs, expressed as REY (REE + Y). Yttrium is inserted between Dy and Ho (Bau et al., 1996; Bau and Dulski, 1999); Y and Ho act similarly because of their similar ionic radii and valences (Bau and Dulski, 1999). The REY concentrations were used in many previous studies to study the genesis of BIFs because of minimal fractionation of REY

during precipitation of iron oxide and negligible mobility of REY during diagenesis and metamorphism (Bau and Möller, 1993; Bekker et al., 2010). The iron ore REY concentrations were normalized in four ways: 1) chondrite (subscript CN; values from (Taylor and McLennan, 1985), 2) post–Archean Australian shale (PAAS, subscript SN; values from McLennan (1989), 3) North American shale composite (NASC, subscript NN; values from Gromet et al. (1984), and 4) Mozaan shale (WMS, subscript WMS; values from Alexander et al. (2008). The WMS values were calculated from the average of three Mozaan shales. The normalized values are commonly marked with the subscript N. The REE anomalies were calculated using $Eu/Eu^* = Eu_N / (0.5 * (Sm_N + Gd_N))$, $La/La^* = La_N / (3 Pr_N - 2Nd_N)$, $Gd/Gd^* = Gd_N / (2 Tb_N - Dy_N)$, and $Ce/Ce^* = Ce_N / (2 Pr_N - Nd_N)$; the Y anomalies were calculated using $Y/Y^* = 2Y / (Dy_N + Ho_N)$ or the Y/Ho ratio. These equations consider the relationships with adjacent elements (Bolhar et al., 2004). The fractionation of LREE/HREE is expressed as $(La/Yb)_N$. The total REY concentrations vary from 9.60 to 19.41 ppm, with an average of 13.33 ppm. The values are lower than those of the Archean BIFs in the NCC. Most of the BIFs are assumed to have formed from metal–enriched basinal fluids (Laurila et al., 2014). Figure 2.5 shows the REY patterns of the iron ores of the Yishui BIF against PAAS. The geochemical signatures of the Yishui BIF include positive La anomalies (1.05–1.18), Eu anomalies (2.44–4.19), and Gd anomalies (1.09–1.24); positive to slightly negative Y anomalies (0.95–1.53); and slightly negative Ce anomalies (0.87–0.98) with enriched HREE [$(La/Yb)_{SN} = 0.17–0.32$]. The $(Eu/Eu^*)_{SN}$ values of the Yishui BIF are higher than those of Archean BIFs in the NCC. The $(Ce/Ce^*)_{SN}$ versus $(Pr/Pr^*)_{SN}$ diagram from Bau and Dulski (1996) introduced a standard to distinguish the La and Ce anomalies in BIFs because positive anomalies

affect the Ce anomalies (Figure 2.6). The IIa field in the diagram indicates a positive La anomaly and an insignificant Ce anomaly, which are related to low oxygen concentrations (Bau and Dulski, 1996). Typical values of Archean BIFs are $(La/Sm)_{CN} > 1$, $(Sm/Yb)_{SN} < 1$, and $(Eu/Sm)_{SN} > 1$; they are consistent with the values of the Yishui BIF. The Ge (n.d.–9.66 ppm), Cr (n.d.–8.54 ppm), Co (0–1.85 ppm), Zn (0–21.47 ppm), and Ni (2.42–6.92 ppm) concentrations are low and variable and the Th, Rb, Pb, Mo, and Nb concentrations are lower than 1 ppm.

2.5.2. Iron ore compositions

The main components, such as SiO_2 and $Fe_2O_3^T$, and low contents of high field strength elements (HFSE) and $\sum REE$ suggest that the iron ores preserved the original chemical precipitation components when they first formed. Quartz and iron oxide host SiO_2 and Fe_2O_3 , respectively (Klein et al., 2005). The minor elements, such as Al_2O_3 , Na_2O , and K_2O , are hosted in silicate minerals. The very low contents of Ba (average 6.82 ppm) and Cu (average 5.88 ppm) are correlated with the absence of barite and chalcopyrite (Yang et al., 2015). A positive relationship between Al_2O_3 and TiO_2 is a common feature of other BIFs around the world (Yang et al., 2015). Zirconium is positively correlated with Al_2O_3 and TiO_2 (R^2 values of 0.74 and 0.52, respectively; not shown).

2.6. Discussion

2.6.1. Constraints on the source of the ore-forming material of the Yishui BIF

2.6.1.1. Detrital input

Precambrian sediment might be affected by syndepositional contamination and post-depositional metamorphism (diagenesis and metamorphism). Not all BIFs preserved their original chemical components (Bekker et al., 2010; Zhang et al., 2011; Sun et al., 2014a; Sun et al., 2014b). The contribution of contamination has to be evaluated before interpreting the genesis of BIFs. Because Al_2O_3 , TiO_2 , and HFSE (Th, Zr, Hf and Sc) are considered to be immobile during weathering, diagenesis, and hydrothermal processes (Kato et al., 1996; Zhang et al., 2011), they are used as indicators of contamination (Kato et al., 1996; Basta et al., 2011). The iron ores of the Yishui BIF have low concentrations of $\text{Al}_2\text{O}_3 + \text{TiO}_2$ (0.58–1.27 wt.%); the correlations between Al_2O_3 and TiO_2 are poor. The $\text{Al}/(\text{Al} + \text{Fe} + \text{Mn})$ vs. (Fe/Ti) diagram represents the proportions of terrigenous sediment and hydrothermal material (Figure 2.7). Iron and manganese are enriched in hydrothermal sediments, whereas aluminium and titanium are enriched in pelagic and terrigenous sediments (González et al., 2009). The diagram indicates that the effect of contamination on the Yishui BIF is almost negligible. With respect to Archean upper crust, the trace element concentrations of the Yishui BIF are relatively low (Figure 2.8). Zirconium and thorium are depleted in the evolved crust and are related to minor detrital input during BIF precipitation (Dai et al., 2014). Terrestrial material, such as igneous rocks or epiclastic sediments, has a constant chondritic Y/Ho ratio (28) and modern seawater has superchondritic Y/Ho ratios (> 44 ; (Nozaki et al., 1997; Bau and Dulski, 1999). Mixing of terrestrial material and seawater leads to lower Y/Ho ratios. The poor correlation with Y/Ho and lithophile elements is responsible for detritus-free BIFs (Figure 2.9). The results suggest the insignificance of contamination during the formation of the Yishui BIF.

2.6.1.2. Source characteristics

During the precipitation of ferric iron oxides and oxyhydroxides, REY is considered to be immobile (Bekker et al., 2010). The REY concentrations are commonly used to identify the sources of iron and silica and genetic environment of BIFs (Derry and Jacobsen, 1990; Planavsky et al., 2010; Tang et al., 2013a; Sun et al., 2014a; Sun et al., 2014b).

Research on the sources of iron and silica is one of the most important steps in investigating the genesis of BIFs. Bolhar et al. (2004) summarized the REY characteristics of modern seawater, which include: 1) positive La, Gd, and Y anomalies and negative Ce anomalies in PAAS-normalized REY; 2) HREE enrichment relative to LREEs and MREEs [(Gd/Yb)_{SN} < 1 and (La/Yb)_{SN} < 1]; and 3) strong negative Ce anomalies (most unique characteristic of modern seawater). The negative Ce anomaly is the result of oxidation of Ce³⁺ to Ce⁴⁺ (Bau and Möller, 1993; Sun et al., 2014a). The positive La, Gd, and Y anomalies of PAAS-normalized REYs are related to the ionic stability. The elements are more stable in solution as a complexation than other adjacent elements because of the structure of the inner 4f electron (Lee and Byrne, 1993; Bolhar et al., 2005). The HREE enrichment is the cause of the affinity (or stability) and atomic mass. The affinity of the solution complex increases with increasing atomic mass. The LREE depletion indicates a deep seawater origin (German and Elderfield, 1989; Lee and Byrne, 1993; Sholkovitz et al., 1994; Bolhar et al., 2005).

The iron ores of the Yishui BIF have modern seawater inheritance of positive La and Y anomalies with enrichment of HREE (Alibo and Nozaki, 1999; Bolhar et al.,

2004). The slightly negative Ce anomalies are related to the low fO_2 condition during BIF precipitation. The ore samples in this study display a strong positive Eu anomaly. The REY features of seawater do not exhibit a positive Eu anomaly, while high-temperature hydrothermal fluids have a positive Eu anomaly with LREE enrichment (Danielson et al., 1992; Bau and Dulski, 1999). Strong positive Eu anomalies account for the contribution of high-temperature hydrothermal fluids to BIF formation. The REY patterns suggest that seawater and high-temperature hydrothermal fluids were involved in the genesis of the Yishui BIF. The reduction of Eu^{3+} to Eu^{2+} increases the intensity of the Eu anomaly (Danielson et al., 1992). The Eu redox potential is temperature dependent (Sverjensky, 1984; Bilal, 1991). Reduced Eu only occurs at high-temperature conditions; Eu^{2+} occurs in high-temperature hydrothermal fluid systems under extremely oxygen-deficient conditions of the Archean (Danielson et al., 1992). Hence, a strong positive Eu anomaly is considered to be the signature of high-temperature hydrothermal fluid input, whereas a weak or no Eu anomaly is related to the disappearance or decrease of high-temperature hydrothermal fluid input. The thermal evolution of the oceanic crust in the Precambrian can explain the decreasing intensity of the positive Eu anomaly (Danielson et al., 1992). Since the role of high-temperature hydrothermal fluids decrease from Archean to the Paleoproterozoic, the intensity of Eu anomaly of Superior-type BIFs is smaller than that of Algoma-type BIFs (Klein and Beukes, 1993). Thus, Superior-type BIFs can better preserve coeval seawater features than Algoma-type BIFs (Huston and Logan, 2004). Huston and Logan (2004) proposed a classification scheme for different types of BIFs based on the NASC-normalized Eu anomaly. The $(Eu/Eu^*)_{NN}$ value of Algoma-type BIFs is greater than 1.8 and that of Superior-type BIFs is smaller than 1.8. The different

values are the result of distinct depositional environments. High-temperature hydrothermal fluids ($> 250^{\circ}\text{C}$) have $(\text{Eu}/\text{Eu}^*)_{\text{CN}} > 1$ and lower-temperature hydrothermal fluids ($< 250^{\circ}\text{C}$) have $(\text{Eu}/\text{Eu}^*)_{\text{CN}} \approx 1$ (Bau and Dulski, 1996). The $(\text{Eu}/\text{Eu}^*)_{\text{NN}}$ values vary from 2.47 to 4.38 and the $(\text{Eu}/\text{Eu}^*)_{\text{CN}}$ values vary from 1.70 to 3.07 of the Yishui BIF. In conclusion, Yishui BIF is an Algoma-type BIF and volcanic hydrothermal activity is involved in formation processes.

Several diagrams also support seawater and hydrothermal origin. Both the SiO_2 vs. Al_2O_3 (Figure 2.10a) and $(\text{Co} + \text{Ni} + \text{Cu})$ vs. $\sum\text{REE}$ discrimination diagrams (Dymek and Klein, 1988) distinguish hydrothermal field and hydrogenous origin. The samples in this study plot within the hydrothermal field. The Fe–Mn–Al (wt.%) ternary diagram (Figure 2.10b) and $(\text{Gd}/\text{Gd}^*)_{\text{WMS}} - (\text{La}/\text{La}^*)_{\text{WMS}}$ diagram (Figure 2.10c) indicate that all samples are genetically related to submarine hydrothermal deposits. The Y/Ho ratio of seawater is superchondritic (> 44) and that of the hydrothermal fluids is chondritic (26–28; Bau and Dulski, 1999). The Y/Ho ratios of the Yishui BIF are 24–40, with an average of 33. It is reasonable to infer that the Yishui BIF was formed by a mixture of seawater and hydrothermal fluid.

Alexander et al. (2008) conducted further research on the mixing proportions of seawater and high-temperature hydrothermal fluids during BIF precipitation. Conservative two-endmember mixing lines, such as the Y/Ho vs. Eu/Sm (Figure 2.11a), Y/Ho vs. Sm/Yb (Figure 2.11b), and Sm/Yb vs. Eu/Sm (Figure 2.11c) diagrams, show that the iron ores of the Yishui BIF can be precipitated from less than 1% of high-temperature hydrothermal fluid mixed with seawater (Figure 2.11). The REEs are mainly affected by the hydrothermal fluid (Danielson et al., 1992). The REE concentrations of

hydrothermal fluids are much higher than those of seawater (Elderfield and Greaves, 1982; Douville et al., 1999). In addition, many BIFs in the world were identified as precipitation contribution of seawater and high-temperature hydrothermal fluids (< 1%), as mentioned above (Figure 2.11). The role of extremely low high-temperature hydrothermal fluids is considered to be common feature of BIFs around the world. We conclude that the ore-forming material of the Yishui BIF was derived from seawater and high-temperature fluids in a submarine environment.

The Co/Zn (0.06–0.11), Ni/Zn (0.21–0.33), and MnO/Fe₂O₃^T (0.001–0.004) ratios also indicate a hydrothermal origin (Sugitani, 1992); Co, Mn, K, Ca, Cd, and Zn are highly abundant near hydrothermal vents (Hein et al., 1994). The low concentrations of these elements in the iron ores indicate that the Yishui BIF was formed relatively far from hydrothermal vents, which is similar to Jingtieshan BIFs in NW China and Arabian–Nubian Shield BIFs (Stern et al., 2013; Yang et al., 2015).

The interpretation of geochemical data is indicative of the source of the ore-forming material, which derived from the mixture of high-temperature hydrothermal fluids (less than 1%) and seawater in a submarine environment.

2.6.2. Genesis of the Yishui BIF and tectonic implications

2.6.2.1. Depositional environment

As described previously, Precambrian BIFs are mainly divided into Algoma- and Superior-type BIFs based on their depositional settings (Gross and McLeod, 1980). Most of the BIFs in the NCC have Archean Algoma-type BIF affinity (Shen et al., 2005; Lan et al., 2014b), while few BIFs belong to Paleoproterozoic Superior-type BIFs,

indicating that the depositional environment is one of the essential factors determining the BIF type (Lan et al., 2014b). The former underwent greenschist to granulite facies metamorphism and the latter experienced lower-grade amphibolite facies metamorphism (Li et al., 2014b). Hence, the majority of the BIFs in the NCC did not preserve their original geochemical signature. Algoma-type BIFs are widespread in the eastern and central NCC including the Hebei, Liaoning, Wutai, and western Shandong provinces (Zhang et al., 2012; Lan et al., 2014b), whereas Superior-type BIFs are located in the Shanxi and eastern Shandong provinces (Lan et al., 2014b). The different distribution of the BIFs based on the age implies remarkably different environmental conditions of the Archean and Paleoproterozoic (Lan et al., 2014b).

Obvious Eu anomalies of the iron ores from the Yishui BIF indicate that the BIF was precipitated in a hydrothermal volcanic submarine environment. The depositional environment might have supplied iron and silica to the Yishui BIF. In addition, Yishui BIF related amphibolitic wallrock indicates a relationship between BIF and volcanic activity. It is worth noting that the Yishui BIF is an Algoma-type BIF in terms of depositional condition.

The Ce anomaly can be used as a paleo-redox indicator of the paleo-ocean during BIF formation (German and Elderfield, 1990). The oxidation of Ce^{3+} to Ce^{4+} leads to the decoupling of Ce from other REEs, which causes the formation of less soluble Ce^{4+} . Hence, Ce^{4+} is preferentially absorbed onto Mn-Fe oxyhydroxides, clay particles, and organic matter (Elderfield and Greaves, 1982; Alibo and Nozaki, 1999; Basta et al., 2011). The oxygenated modern seawater therefore has a strong negative Ce anomaly, whereas suboxic and anoxic marine conditions lack a negative Ce anomaly (Bekker et al.,

2010). The iron ores of the Yishui BIF plot in fields IIa and IIIb in the Ce and Pr anomaly scatter diagram (Bau and Dulski, 1996), indicating no and a negative Ce anomaly, respectively. Both oxidized surface seawater and reduced bottom water might have influenced the formation of the Yishui BIF.

2.6.2.2. Tectonic implications of the Archean NCC and a possible genetic model

Amalgamation of seven microblocks, including the Jiuliao (JL), Qianhuai (QH), Ordos (IR), Jining (JN), Xuchang (XCH), Alshan (ALS) and Xuhuai (XH) blocks led to magmatic activity and metamorphism. These depositional conditions were sufficient for the deposition of Algoma-type BIFs and are closely associated with the abundance of BIFs in the NCC (Zhai and Santosh, 2011; Lan et al., 2014b). Despite of the close relationship between the metallogenic systems and tectonic events in China, the formation mechanism of BIFs and tectonic evolution of the NCC are still controversial.

Based on whole-rock Nd isotope and zircon U-Pb and Hf isotopic analyses, some have proposed that the two main periods of crustal growth of the NCC are 2.8 to 2.7 Ga and 2.6 to 2.5 Ga (Shen et al., 2005; Han et al., 2014). The Archean metamorphism of the NCC can be explained by a counter-clockwise P-T path involving near-isobaric cooling (Zhao et al., 1998; Wu et al., 2012). As shown in Figure 2.12, the P-T path of the NCC is counter-clockwise involving near-isobaric cooling. Counter-clockwise P-T paths can occur in continental rift regions, continental arc regimes, and mantle plume tectonic regimes (Sandiford and Powell, 1986; Bohlen, 1991; Zhao et al., 1998, 1999; Wu et al., 2012). The continental rift environment model cannot explain the extensive exposure of 2.6–2.5 Ga granitoid, predominant domal structure, and lack of

abundant alkali intrusions (Zhao et al., 1998). The continental magmatic arc environment model cannot explain the geological characteristics of the Late Neoproterozoic basement rocks in the NCC such as the large exposure of TTG rocks that formed over a short period (2.6–2.5 Ga) and the presence of komatiites and dominant diapirism–related domal structures (Han et al., 2014). In contrast, the mantle plume model better explains the tectonic setting of the EB of the NCC including the large–scale intrusions, bimodal volcanic assemblage, and relationship between mafic rocks and continental tholeiitic basalt (Zhao et al., 1998; Wu et al., 2012). Hence, Zhao et al. (1998) first adapted the mantle plume model to describe the tectonic evolution of the EB of the NCC. Wu et al. (2012) studied the petrology and quantitative P–T pseudosection models using mafic granulite from the Yishui Group. They explained the specific tectonothermal evolution scenario based on an upwelling mantle plume beneath the western Shandong Province and used the terms M1 (metamorphic stage 1; pre–peak), M2 (metamorphic stage 2; peak), and M3 (metamorphic stage 3; post–peak) to describe the metamorphic episodes of different metamorphic events. Liu et al. (2017) conducted a geochronological, geochemical, and isotope study using charnockite of the Yishui Group, further suggesting extensive tectonic settings in the Archean in the NCC. Based on previous regional tectonic studies, Yishui County is considered to be related to the intrusion and underplating of mantle–derived magma. We infer that the Yishui BIF might have formed in a similar tectonic setting. The orebody of the Yishui BIF and the amphibolite contact (basaltic protolith) represent the relationship between the BIF and volcanic activities, indicating Algoma–type BIF affinity.

Isley and Abbott (1999) revealed the relationship between mafic mantle plume

magmatism and BIF deposition based on statistical analysis. Mantle plume activity provides the source of iron and enhances the precipitation of the BIF. In addition, the age of the Precambrian BIF is consistent with global mantle plume events (3.8–1.6 Ga). In this study, we favor mantle plume model since it can not only explain the petrological and geochemical signatures of Yishui county but also explain the source of iron and silica for Yishui BIF (Figure 2.13). It could have formed Algoma–type BIFs conditions during the precipitation of the Yishui BIF. In this theory, iron–rich fluid and silica–rich fluid were possibly generated by the mantle plume and 0.1% high–temperature hydrothermal fluid and seawater were responsible BIF formation.

2.7. Conclusions

Based on the results of geological, petrological, and geochemical analyses, the significant characteristics of the Yishui BIF are as follows:

- 1) The Yishui BIF is located in the Liuhang Formation of the Taishan Group in Yishui County of the WSP in the NCC.
- 2) The analysis of major elements, trace elements, and REEs indicates that the Yishui BIF are Neoproterozoic Algoma–type BIFs and both less than 1% high–temperature hydrothermal fluids ($> 250^{\circ}\text{C}$) and seawater were involved in the formation of the BIFs. Submarine hydrothermal fluids associated with volcanic activity produced ore–forming material, such as silica and iron, under anoxic and suboxic conditions.
- 3) The low contents of Al_2O_3 , TiO_2 , and HFSEs indicate that little contamination contributed to the formation of the Yishui BIF.

- 4) The mantle plume model does not only account for the tectonic events and evolution of the NCC but also for the genetic mechanism of the Yishui BIF.

References

- Alexander, B. W., Bau, M., Andersson, P., Dulski, P., 2008. Continentally-derived solutes in shallow Archean seawater: rare earth element and Nd isotope evidence in iron formation from the 2.9 Ga Pongola Supergroup, South Africa. *Geochimica et Cosmochimica Acta*. 72, 378-394.
- Alibo, D. S., Nozaki, Y., 1999. Rare earth elements in seawater: particle association, shale-normalization, and Ce oxidation. *Geochimica et Cosmochimica Acta*. 63, 363-372.
- Basta, F. F., Maurice, A. E., Fontboté, L., Favarger, P.-Y., 2011. Petrology and geochemistry of the banded iron formation (BIF) of Wadi Karim and Um Anab, Eastern Desert, Egypt: implications for the origin of Neoproterozoic BIF. *Precambrian Research*. 187, 277-292.

- Bau, M.Dulski, P., 1996. Distribution of yttrium and rare-earth elements in the Penge and Kuruman iron-formations, Transvaal Supergroup, South Africa. *Precambrian Research*. 79, 37-55.
- Bau, M.Dulski, P., 1999. Comparing yttrium and rare earths in hydrothermal fluids from the Mid-Atlantic Ridge: implications for Y and REE behaviour during near-vent mixing and for the Y/Ho ratio of Proterozoic seawater. *Chemical Geology*. 155, 77-90.
- Bau, M., Koschinsky, A., Dulski, P., Hein, J. R., 1996. Comparison of the partitioning behaviours of yttrium, rare earth elements, and titanium between hydrogenetic marine ferromanganese crusts and seawater. *Geochimica et Cosmochimica Acta*. 60, 1709-1725.
- Bau, M., Möller, P., 1992. Rare earth element fractionation in metamorphogenic hydrothermal calcite, magnesite and siderite. *Mineralogy and Petrology*. 45, 231-246.
- Bau, M., Möller, P., 1993. Rare earth element systematics of the chemically precipitated component in Early Precambrian iron formations and the evolution of the terrestrial atmosphere-hydrosphere-lithosphere system. *Geochimica et Cosmochimica Acta*. 57, 2239-2249.
- Bekker, A., Slack, J. F., Planavsky, N., Krapež, B., Hofmann, A., Konhauser, K. O., Rouxel, O. J., 2010. Iron formation: the sedimentary product of a complex interplay among mantle, tectonic, oceanic, and biospheric processes. *Economic Geology*. 105, 467-508.
- Bilal, B., 1991. Thermodynamic study of $\text{Eu}^{3+}/\text{Eu}^{2+}$ redox reaction in aqueous solutions at elevated temperatures and pressures by means of cyclic voltammetry. *Zeitschrift für Naturforschung A*. 46, 1108-1116.
- Bohlen, S., 1991. On the formation of granulites. *Journal of Metamorphic Geology*. 9, 223-229.
- Bolhar, R., Kamber, B. S., Moorbath, S., Fedo, C. M., Whitehouse, M. J., 2004. Characterisation of early Archaean chemical sediments by trace element signatures. *Earth and Planetary Science Letters*. 222, 43-60.

- Bolhar, R., Van Kranendonk, M. J., Kamber, B. S., 2005. A trace element study of siderite–jasper banded iron formation in the 3.45 Ga Warrawoona Group, Pilbara Craton—formation from hydrothermal fluids and shallow seawater. *Precambrian Research*. 137, 93-114.
- Boström, K., 1973. The origin and fate of ferromagnesian active ridge sediments. *Stockholm contributions in geology*.
- Dai, Y., Zhang, L., Zhu, M., Wang, C., Liu, L., Xiang, P., 2014. The composition and genesis of the Mesoproterozoic Dagushan banded iron formation (BIF) in the Anshan area of the North China Craton. *Ore Geology Reviews*. 63, 353-373.
- Danielson, A., Möller, P., Dulski, P., 1992. The europium anomalies in banded iron formations and the thermal history of the oceanic crust. *Chemical Geology*. 97, 89-100.
- Derry, L. A., Jacobsen, S. B., 1990. The chemical evolution of Precambrian seawater: Evidence from REEs in banded iron formations. *Geochimica et Cosmochimica Acta*. 54, 2965-2977.
- Douville, E., Bienvenu, P., Charlou, J. L., Donval, J. P., Fouquet, Y., Appriou, P., Gamo, T., 1999. Yttrium and rare earth elements in fluids from various deep-sea hydrothermal systems. *Geochimica et Cosmochimica Acta*. 63, 627-643.
- Dymek, R. F., Klein, C., 1988. Chemistry, petrology and origin of banded iron-formation lithologies from the 3800 Ma Isua supracrustal belt, West Greenland. *Precambrian Research*. 39, 247-302.
- Elderfield, H., Greaves, M. J., 1982. The rare earth elements in seawater. *Nature*. 296, 214-219.
- Evans, K., McCuaig, T., Leach, D., Angerer, T., Hagemann, S., 2013. Banded iron formation to iron ore: A record of the evolution of Earth environments? *Geology*. 41, 99-102.
- Fan, H.-R., Zhang, L.-C., Yang, K.-F., 2014. Major Precambrian events and mineralization in the North China Craton: Preface. *Ore Geology Reviews*.
- Geng, Y., Du, L., Ren, L., 2012. Growth and reworking of the early Precambrian continental crust in the North China Craton: constraints from zircon Hf isotopes.

- Gondwana Research. 21, 517-529.
- German, C. R., Elderfield, H., 1989. Rare earth elements in Saanich Inlet, British Columbia, a seasonally anoxic basin. *Geochimica et Cosmochimica Acta*. 53, 2561-2571.
- German, C. R., Elderfield, H., 1990. Application of the Ce anomaly as a paleoredox indicator: the ground rules. *Paleoceanography*. 5, 823-833.
- González, P. D., Sato, A. M., Llambías, E. J., Petronilho, L. A., 2009. Petrology and geochemistry of the banded iron formation in the Eastern Sierras Pampeanas of San Luis (Argentina): Implications for the evolution of the Nogolí Metamorphic Complex. *Journal of South American Earth Sciences*. 28, 89-112.
- Gromet, L. P., Haskin, L. A., Korotev, R. L., Dymek, R. F., 1984. The "North American shale composite": its compilation, major and trace element characteristics. *Geochimica et Cosmochimica Acta*. 48, 2469-2482.
- Gross, G., McLeod, C., 1980. A preliminary assessment of the chemical composition of iron formations in Canada. *The Canadian Mineralogist*. 18, 223-229.
- Hagemann, S., Angerer, T., Duuring, P., Rosière, C., e Silva, R. F., Lobato, L., Hensler, A., Walde, D., 2016. BIF-hosted iron mineral system: A review. *Ore Geology Reviews*. 76, 317-359.
- Han, C., Xiao, W., Su, B., Chen, Z., Zhang, X., Ao, S., Zhang, J., Zhang, Z., Wan, B., Song, D., 2014. Neoproterozoic Algoma-type banded iron formations from Eastern Hebei, North China Craton: SHRIMP U-Pb age, origin and tectonic setting. *Precambrian Research*. 251, 212-231.
- Hein, J. R., Hsueh-Wen, Y., Gunn, S. H., Gibbs, A. E., Chung-ho, W., 1994. Composition and origin of hydrothermal ironstones from central Pacific seamounts. *Geochimica et Cosmochimica Acta*. 58, 179-189.
- Holland, H. D., 1973. The oceans; a possible source of iron in iron-formations. *Economic Geology*. 68, 1169-1172.
- Hu, H., Niu, S., Wang, B., Sun, A., Xu, C., Li, Y., Li, M., 2005. Source of fluids in the Longquanzhan gold deposits in the Yishui area, Shandong, China. *Mineral Deposit Research: Meeting the Global Challenge*. Springer. pp. 1539-1542.

- Huston, D. L., Logan, G. A., 2004. Barite, BIFs and bugs: evidence for the evolution of the Earth's early hydrosphere. *Earth and Planetary Science Letters*. 220, 41-55.
- Isley, A. E., Abbott, D. H., 1999. Plume-related mafic volcanism and the deposition of banded iron formation. *Journal of Geophysical Research: Solid Earth* (1978–2012). 104, 15461-15477.
- James, H. L., 1954. Sedimentary facies of iron-formation. *Economic Geology*. 49, 235-293.
- Kato, Y., Kawakami, T., Kano, T., Kunugiza, K., Swamy, N. S., 1996. Rare-earth element geochemistry of banded iron formations and associated amphibolite from the Sargur belts, south India. *Journal of Southeast Asian Earth Sciences*. 14, 161-164.
- Khalil, K. I., El-Shazly, A. E., Lehmann, B., 2015. Late Neoproterozoic banded iron formation (BIF) in the central Eastern Desert of Egypt: Mineralogical and geochemical implications for the origin of the Gebel El Hadid iron ore deposit. *Ore Geology Reviews*. 69, 380-399.
- Klein, C., 2005. Some Precambrian banded iron-formations (BIFs) from around the world: Their age, geologic setting, mineralogy, metamorphism, geochemistry, and origins. *American Mineralogist*. 90, 1473-1499.
- Klein, C., Beukes, N. J., 1993. Sedimentology and geochemistry of the glaciogenic late Proterozoic Rapitan iron-formation in Canada. *Economic Geology*. 88, 542-565.
- Lai, X., Yang, X., 2012. Characteristics of the banded iron formation (BIF) and its zircon chronology in Yangzhuang, western Shandong. *ACTA PETROLOGICA SINICA*. 28, 3612-3622.
- Lan, T.-G., Fan, H.-R., Santosh, M., Hu, F.-F., Yang, K.-F., Liu, Y., 2014. U–Pb zircon chronology, geochemistry and isotopes of the Changyi banded iron formation in the eastern Shandong Province: Constraints on BIF genesis and implications for Paleoproterozoic tectonic evolution of the North China Craton. *Ore Geology Reviews*. 56, 472-486.
- Lascelles, D. F., 2007. Black smokers and density currents: a uniformitarian model for the genesis of banded iron-formations. *Ore Geology Reviews*. 32, 381-411.
- Laurila, T. E., Hannington, M. D., Petersen, S., Garbe-Schönberg, D., 2014. Early

- depositional history of metalliferous sediments in the Atlantis II Deep of the Red Sea: evidence from rare earth element geochemistry. *Geochimica et Cosmochimica Acta*. 126, 146-168.
- Lee, J. H. Byrne, R. H., 1993. Complexation of trivalent rare earth elements (Ce, Eu, Gd, Tb, Yb) by carbonate ions. *Geochimica et Cosmochimica Acta*. 57, 295-302.
- Li, H., Zhang, Z., Li, L., Zhang, Z., Chen, J. Yao, T., 2014. Types and general characteristics of the BIF-related iron deposits in China. *Ore Geology Reviews*. 57, 264-287.
- Liu, D., Nutman, A., Compston, W., Wu, J. Shen, Q. H., 1992. Remnants of ≥ 3800 Ma crust in the Chinese part of the Sino-Korean craton. *Geology*. 20, 339-342.
- Liu, J., Liu, F., Ding, Z., Liu, P., Wang, F., Yang, H., Cai, J. Shi, J., 2017. Petrogenesis and tectonic implications of the charnockites in the Yishui Terrane, North China Craton. *Precambrian Research*.
- McLennan, S., 1989. Rare earth elements in sedimentary rocks; influence of provenance and sedimentary processes. *Reviews in Mineralogy and Geochemistry*. 21, 169-200.
- Nozaki, Y., Zhang, J. Amakawa, H., 1997. The fractionation between Y and Ho in the marine environment. *Earth and Planetary Science Letters*. 148, 329-340.
- Planavsky, N., Bekker, A., Rouxel, O. J., Kamber, B., Hofmann, A., Knudsen, A. Lyons, T. W., 2010. Rare earth element and yttrium compositions of Archean and Paleoproterozoic Fe formations revisited: new perspectives on the significance and mechanisms of deposition. *Geochimica et Cosmochimica Acta*. 74, 6387-6405.
- Sandiford, M. Powell, R., 1986. Deep crustal metamorphism during continental extension: modern and ancient examples. *Earth and Planetary Science Letters*. 79, 151-158.
- Shen, B.-f., Zhai, A.-m., Yang, C.-l. Cao, X.-l., 2005. Temporal-spatial distribution and evolutionary characters of Precambrian iron deposits in China. *Geological Survey and Research*. 4, 196-206.
- Sholkovitz, E. R., Landing, W. M. Lewis, B. L., 1994. Ocean particle chemistry: the fractionation of rare earth elements between suspended particles and seawater.

Geochimica et Cosmochimica Acta. 58, 1567-1579.

- Stern, R. J., Mukherjee, S. K., Miller, N. R., Ali, K., Johnson, P. R., 2013. ~ 750Ma banded iron formation from the Arabian-Nubian Shield—Implications for understanding neoproterozoic tectonics, volcanism, and climate change. *Precambrian Research*. 239, 79-94.
- Sugitani, K., 1992. Geochemical characteristics of Archean cherts and other sedimentary rocks in the Pilbara Block, Western Australia: evidence for Archean seawater enriched in hydrothermally-derived iron and silica. *Precambrian Research*. 57, 21-47.
- Sun, X.-H., Zhu, X.-Q., Tang, H.-S., Zhang, Q., Luo, T.-Y., 2014a. The Gongchangling BIFs from the Anshan–Benxi area, NE China: Petrological–geochemical characteristics and genesis of high-grade iron ores. *Ore Geology Reviews*. 60, 112-125.
- Sun, X.-H., Zhu, X.-Q., Tang, H.-S., Zhang, Q., Luo, T.-Y., Han, T., 2014b. Protolith reconstruction and geochemical study on the wall rocks of Anshan BIFs, Northeast China: Implications for the provenance and tectonic setting. *Journal of Geochemical Exploration*. 136, 65-75.
- Sverjensky, D. A., 1984. Europium redox equilibria in aqueous solution. *Earth and Planetary Science Letters*. 67, 70-78.
- Tang, H.-S., Chen, Y.-J., Santosh, M., Zhong, H., Yang, T., 2013. REE geochemistry of carbonates from the Guanmenshan Formation, Liaohe Group, NE Sino-Korean Craton: implications for seawater compositional change during the Great Oxidation Event. *Precambrian Research*. 227, 316-336.
- Taylor, S. R., McLennan, S. M., 1985. *The continental crust: its composition and evolution*.
- Wan, Y., Liu, D., Wang, S., Yang, E., Wang, W., Dong, C., Zhou, H., Du, L., Yang, Y., Diwu, C., 2011. ~ 2.7 Ga juvenile crust formation in the North China Craton (Taishan-Xintai area, western Shandong Province): further evidence of an understated event from U–Pb dating and Hf isotopic composition of zircon. *Precambrian Research*. 186, 169-180.
- Wan, Y., Wang, S., Liu, D., Wang, W., Kröner, A., Dong, C., Yang, E., Zhou, H.,

- Hangqian, X., Ma, M., 2012. Redefinition of depositional ages of Neoproterozoic supracrustal rocks in western Shandong Province, China: SHRIMP U–Pb zircon dating. *Gondwana Research*. 21, 768-784.
- Wang, E., Han, C., Xia, J., Yun, S., 2015. Geochemistry and Tectonic Significance of Chlorite Amphibolite in Nanfen BIF, Benxi Area, Northeastern China. *Journal of Geoscience and Environment Protection*. 3, 54.
- Wang, W., Yang, E., Zhai, M., Wang, S., Santosh, M., Du, L., Xie, H., Lv, B., Wan, Y., 2013. Geochemistry of ~ 2.7 Ga basalts from Taishan area: Constraints on the evolution of early Neoproterozoic granite-greenstone belt in western Shandong Province, China. *Precambrian Research*. 224, 94-109.
- Wonder, J. D., Spry, P. G., Windom, K. E., 1988. Geochemistry and origin of manganese-rich rocks related to iron-formation and sulfide deposits, western Georgia. *Economic Geology*. 83, 1070-1081.
- Wu, M., Zhao, G., Sun, M., Li, S., He, Y., Bao, Z., 2013. Zircon U Pb geochronology and Hf isotopes of major lithologies from the Yishui Terrane: Implications for the crustal evolution of the Eastern Block, North China Craton. *Lithos*. 170, 164-178.
- Wu, M., Zhao, G., Sun, M., Yin, C., Li, S., Tam, P. Y., 2012. Petrology and P–T path of the Yishui mafic granulites: implications for tectonothermal evolution of the Western Shandong Complex in the Eastern Block of the North China Craton. *Precambrian Research*. 222, 312-324.
- Yang, J.-H., Wu, F.-Y., Wilde, S. A., Zhao, G., 2008. Petrogenesis and geodynamics of Late Archean magmatism in eastern Hebei, eastern North China Craton: geochronological, geochemical and Nd–Hf isotopic evidence. *Precambrian Research*. 167, 125-149.
- Yang, X.-Q., Zhang, Z.-H., Duan, S.-G., Zhao, X.-M., 2015. Petrological and geochemical features of the Jingtieshan banded iron formation (BIF): A unique type of BIF from the Northern Qilian Orogenic Belt, NW China. *Journal of Asian Earth Sciences*.
- Zhai, M.-G., Santosh, M., 2011. The early Precambrian odyssey of the North China Craton: a synoptic overview. *Gondwana Research*. 20, 6-25.

- Zhai, M.Santosh, M., 2013. Metallogeny of the North China Craton: link with secular changes in the evolving Earth. *Gondwana Research*. 24, 275-297.
- Zhang, L., Zhai, M., Zhang, X., Xiang, P., Dai, Y., Wang, C.Pirajno, F., 2012. Formation age and tectonic setting of the Shirengou Neoproterozoic banded iron deposit in eastern Hebei Province: constraints from geochemistry and SIMS zircon U–Pb dating. *Precambrian Research*. 222, 325-338.
- Zhang, X., Zhang, L., Xiang, P., Wan, B.Pirajno, F., 2011. Zircon U–Pb age, Hf isotopes and geochemistry of Shuichang Algoma-type banded iron-formation, North China Craton: constraints on the ore-forming age and tectonic setting. *Gondwana Research*. 20, 137-148.
- Zhao, G., Sun, M.Wilde, S. A., 2003. Correlations between the eastern block of the North China Craton and the South Indian block of the Indian shield: an Archean to Palaeoproterozoic link. *Precambrian Research*. 122, 201-233.
- Zhao, G., Sun, M., Wilde, S. A.Sanzhong, L., 2005. Late Archean to Paleoproterozoic evolution of the North China Craton: key issues revisited. *Precambrian Research*. 136, 177-202.
- Zhao, G., Wilde, S. A., Cawood, P. A.Lu, L., 1998. Thermal evolution of Archean basement rocks from the eastern part of the North China Craton and its bearing on tectonic setting. *International Geology Review*. 40, 706-721.
- Zhao, G., Wilde, S. A., Cawood, P. A.LU, L., 1999. Thermal evolution of two textural types of mafic granulites in the North China craton: evidence for both mantle plume and collisional tectonics. *Geological Magazine*. 136, 223-240.
- Zhao, G., Wilde, S. A., Cawood, P. A.Sun, M., 2001. Archean blocks and their boundaries in the North China Craton: lithological, geochemical, structural and P–T path constraints and tectonic evolution. *Precambrian Research*. 107, 45-73.
- Zhao, G.Zhai, M., 2013. Lithotectonic elements of Precambrian basement in the North China Craton: review and tectonic implications. *Gondwana Research*. 23, 1207-1240.
- Zheng, Y.-F., Xiao, W.-J.Zhao, G., 2013a. Introduction to tectonics of China. *Gondwana Research*. 23, 1189-1206.

Zheng, Y.-F., Xiao, W.-J., Zhao, G., 2013b, Introduction to tectonics of China. Elsevier.

Zhu, M., Dai, Y., Zhang, L., Wang, C., Liu, L., 2015. Geochronology and geochemistry of the Nanfen iron deposit in the Anshan-Benxi area, North China Craton: Implications for ~ 2.55 Ga crustal growth and the genesis of high-grade iron ores. *Precambrian Research*.

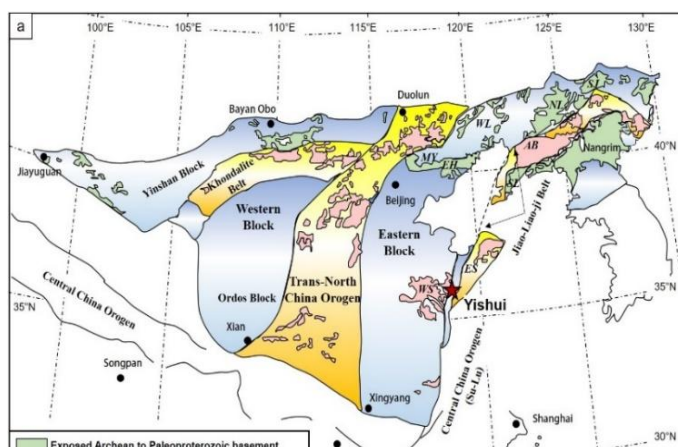


Figure 2.1

Figure 2.1. (a) Tectonic subdivisions of the North China Craton, modified after Zhao et al. (2005). SJ: Southern Jilin; NL: Northern Liaoning; AB: Anshan–Benxi; WL: Western Liaoning; EH: Eastern Hebei; SL: Southern Liaoning; ES: Eastern Shandong; WS: Western Shandong; MY: Miyun. (b) Geological map of the western Shandong Province, modified after Wan et al. (2011). (c) Geological map of the Yishui BIF (Lai and Yang, 2012b).

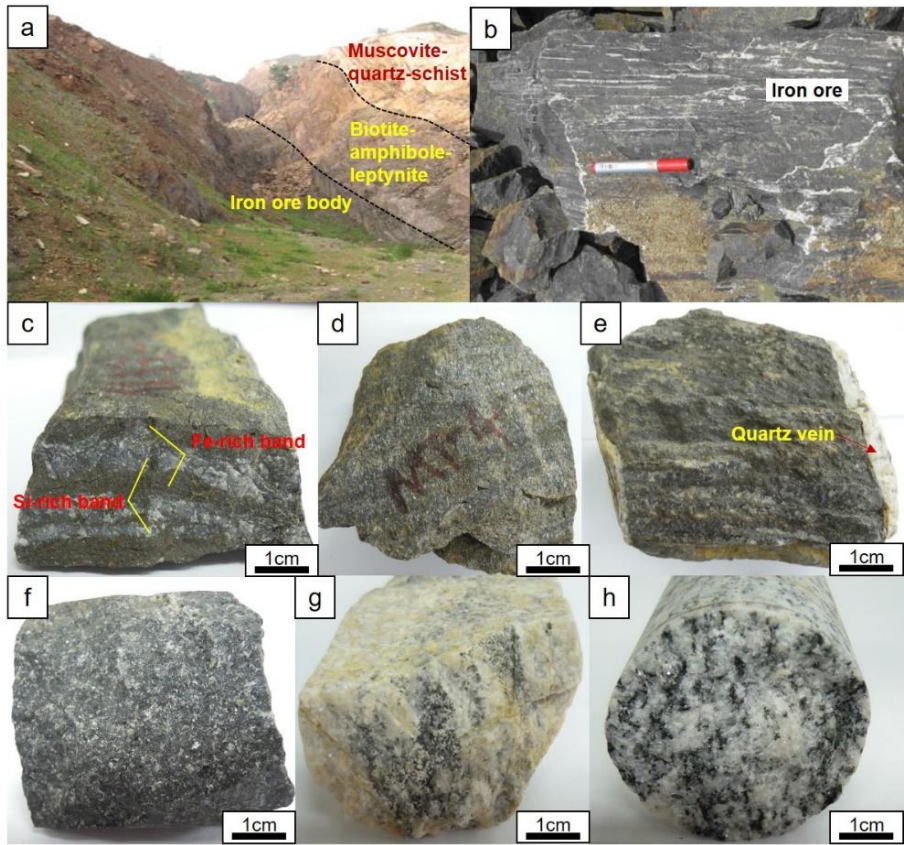


Figure 2.2. Representative photographs of the Yishui BIF and associated rocks. (a) Iron orebodies of the Yishui BIF with biotite–amphibole–leptynite and muscovite–quartz–schist (Lai and Yang, 2012b). (b) Iron orebodies with alternating Fe– and Si–rich layers (Lai and Yang, 2012b). (c) Iron ore with alternating Fe–rich and Si–rich bands. (d–e) Iron ore with massive texture. (f) Drill core photograph of amphibolite. (g) Drill core photograph of granite. (h) Drill core photograph of gneiss.

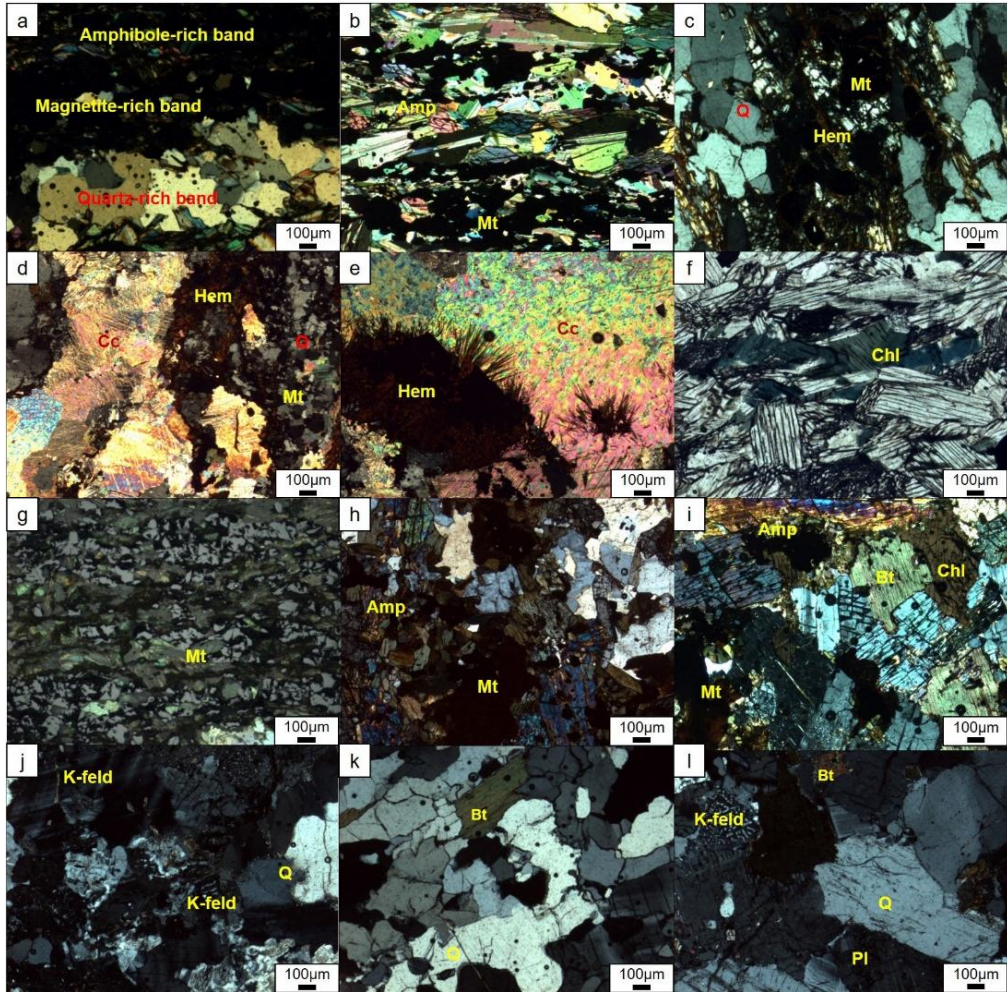


Figure 2.3. Representative photomicrographs of the Yishui BIF and associated rocks. (a) Alternating amphibole-, magnetite-, and quartz-rich microband of iron ore (cross polarized light). (b) Amphibole band with a close relationship between magnetite and epidote (cross polarized light). (c–d) Presence of calcite, hematite,

quartz, and magnetite in iron ore (cross polarized light). (e) Needle-shaped iron oxide (hematite) and adjacent calcite (cross polarized light). (f) Chlorite in iron ore (plane polarized light). (g) Magnetite grains in iron ore (reflected light). (h–i) Amphibolite consisting of amphibole, plagioclase with minor chlorite, biotite, and magnetite. (j) Granite consisting of quartz, K-feldspar, plagioclase, amphibole, and biotite. (k–l) Gneiss with mineral assemblage of quartz, plagioclase, and biotite. Mt: magnetite; Cc: calcite; Hem: hematite; Amp: amphibole; Bt: biotite; Chl: chlorite; Pl: plagioclase; Q: quartz; K-feld: K-feldspar.

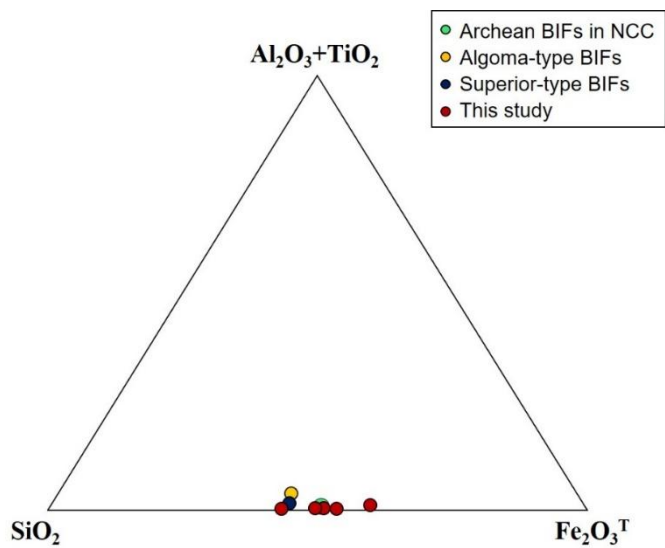


Figure 2.4. Al₂O₃ + TiO₂–SiO₂–Fe₂O₃^T diagram for iron ores from the Yishui BIF (Gross and McLeod, 1980; Lan et al., 2014b).

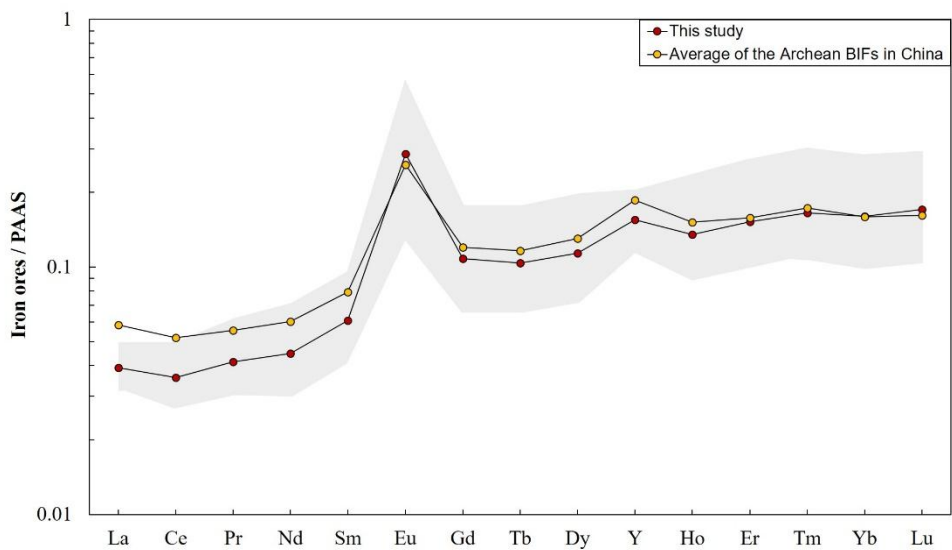


Figure 2.5. PAAS-normalized REY pattern of iron ores of the Yishui BIF. The average of the Archean BIFs in the NCC (Lan et al., 2014b) is plotted for comparison. The range of values for the Yishui BIF is shown as gray shadow and the average values are marked with a red circle.

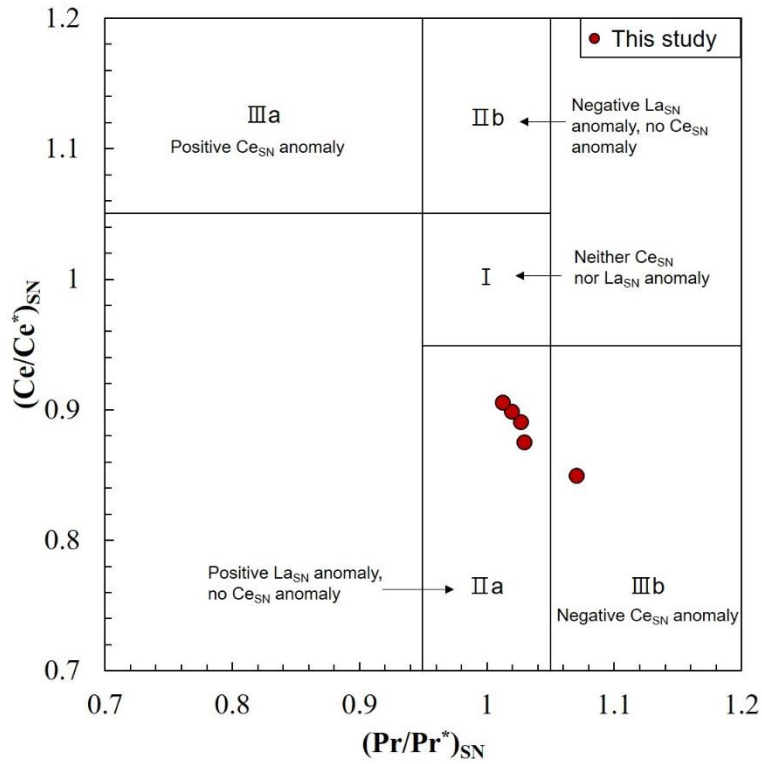


Figure 2.6. $(Ce/Ce^*)_{SN}$ vs. $(Pr/Pr^*)_{SN}$ diagram for the Yishui BIF (Bau and Dulski, 1996).

In this diagram, $(Ce/Ce^*)_{SN}$ and $(Pr/Pr^*)_{SN}$ are calculated from $Ce_{SN}/(0.5 * (La_{SN} + Pr_{SN}))$ and $Pr_{SN}/(0.5 * (Ce_{SN} + Nd_{SN}))$, respectively.

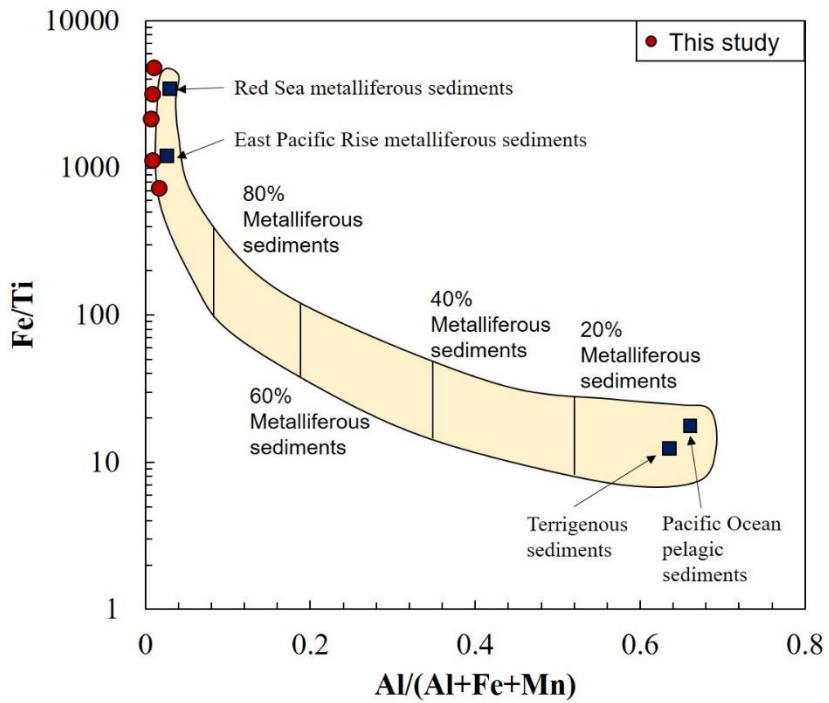


Figure 2.7. Al/(Al + Fe + Mn) vs. Fe/Ti diagram (Boström, 1973) for the Yishui BIF.

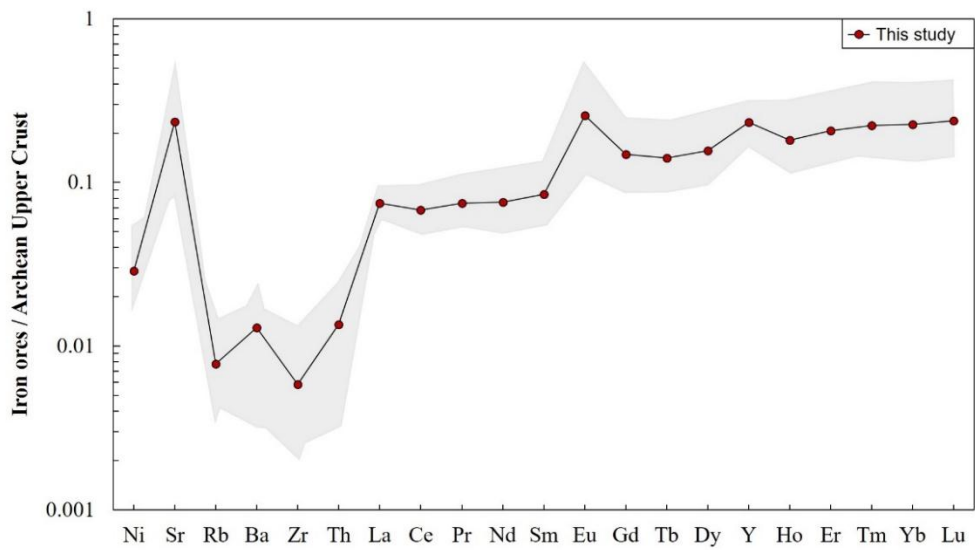


Figure 2.8. Archean upper crust-normalized diagram. The normalized values are from Taylor and McLennan (1985). The range of values for the Yishui BIF is shown as gray shadow and the average values are marked with a red circle.

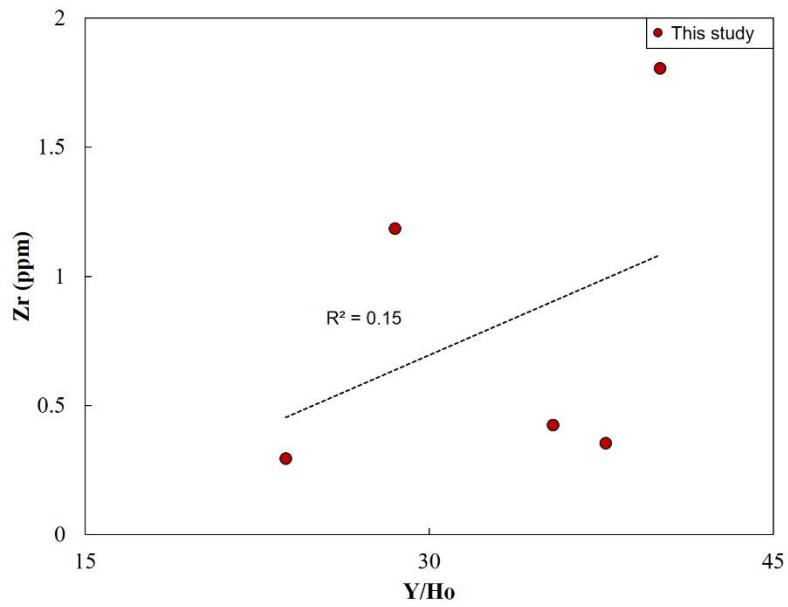


Figure 2.9. Covariant relationship between Y/Ho and Zr (ppm) for the Yishui BIF.

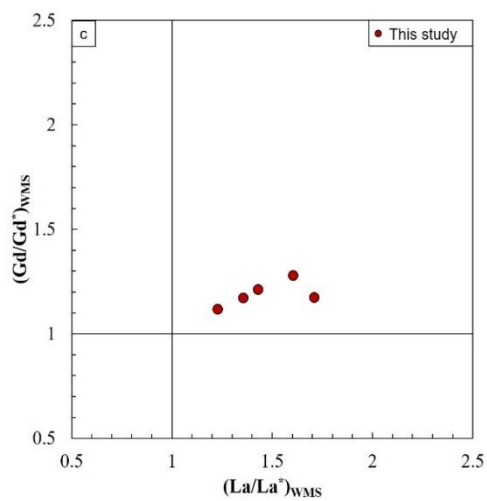
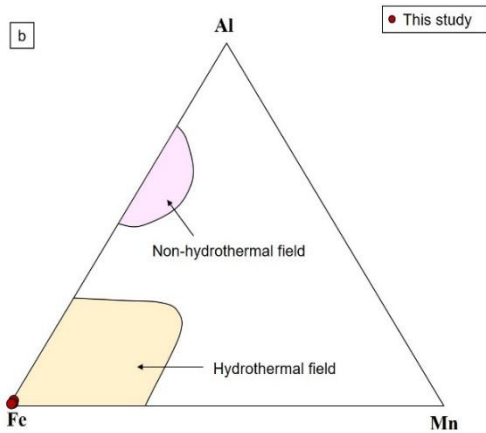
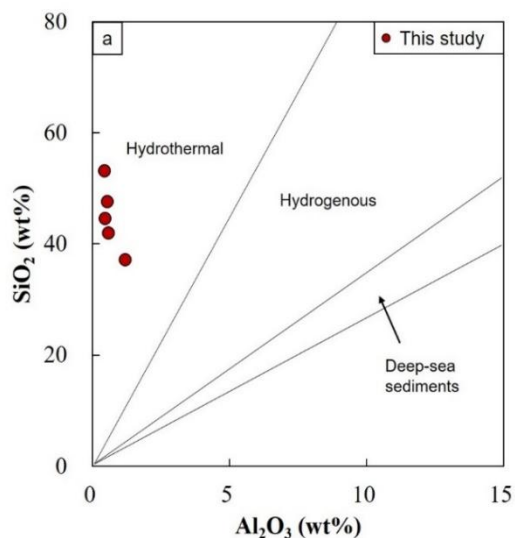


Figure 2.10. (a) Al_2O_3 vs. SiO_2 diagram (Wonder et al., 1988), (b) Al–Fe–Mn (wt.%) ternary diagram (Boström, 1973), and (c) WMS–normalized La and Gd anomaly diagram (Alexander et al., 2008) for the Yishui BIF.

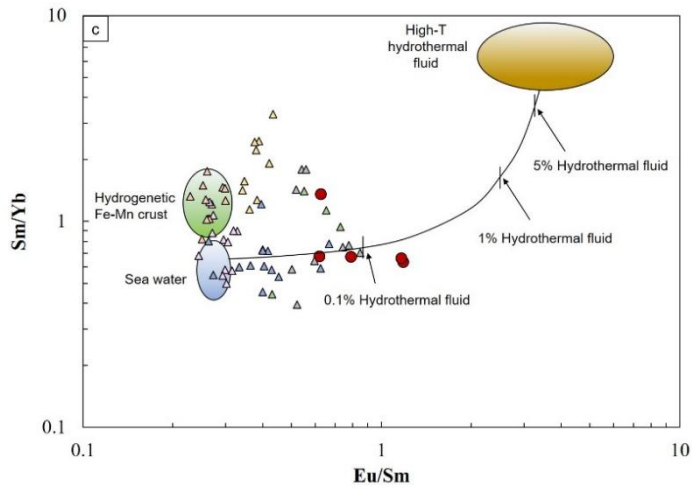
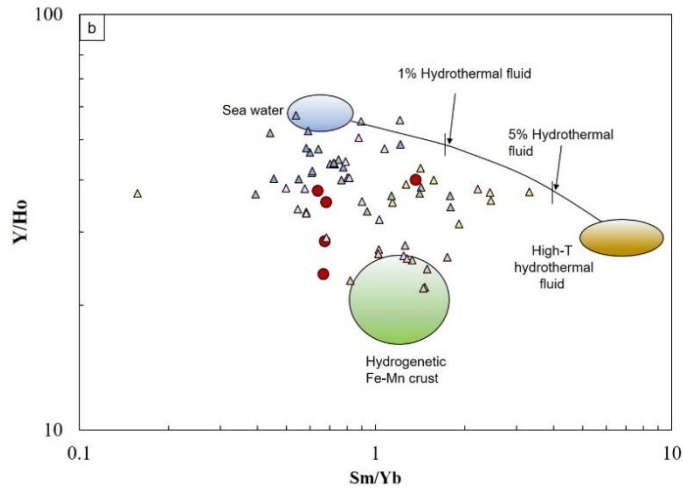
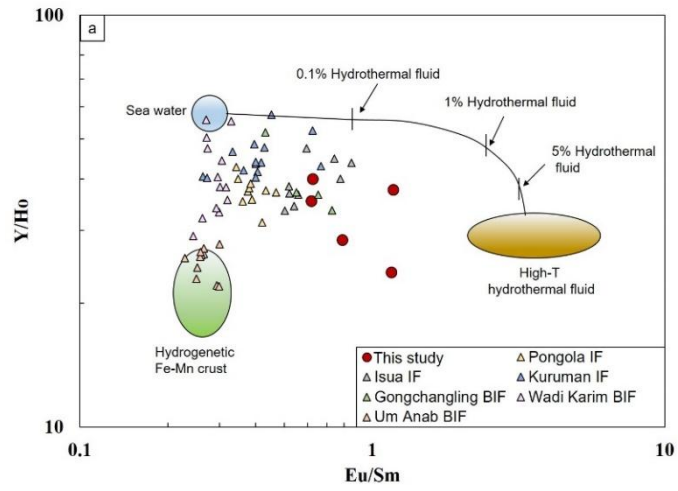


Figure 2.11. Conservative mixing line of high-temperature hydrothermal fluid (Bau and Dulski, 1999) and seawater (Alibo and Nozaki, 1999). (a) Eu/Sm versus Y/Ho, (b) Sm/Yb versus Y/Ho, and (c) Eu/Sm versus Sm/Yb (Alexander et al., 2008) for modern hydrogenetic Fe–Mn crust and Pongola IF (Alexander et al., 2008), Kuruman IF (Bau and Dulski, 1996), Isua IF (Bolhar et al., 2004), Gongchangling BIF (Sun et al., 2014a), and Wadi Karim and Um Anab BIFs (Basta et al., 2011).

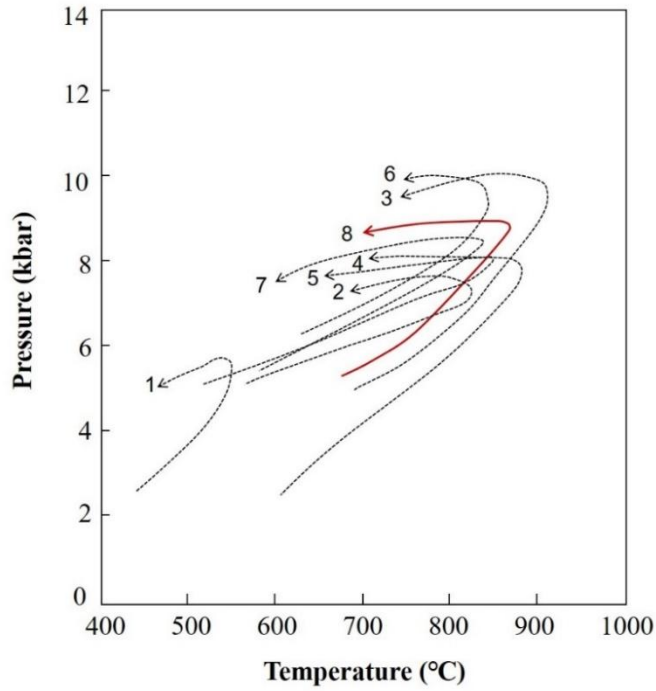


Figure 2.12. Metamorphic P–T paths of various basement rocks of the EB of the NCC (Zhao et al., 1998). 1: Western Shandong; 2: Eastern Hebei; 3: Western Liaoning; 4: Northern Lianing; 5: Eastern Shandong; 6: Miyun–Chengde; 7: Southern Jilin; 8: Yishui County (study area).

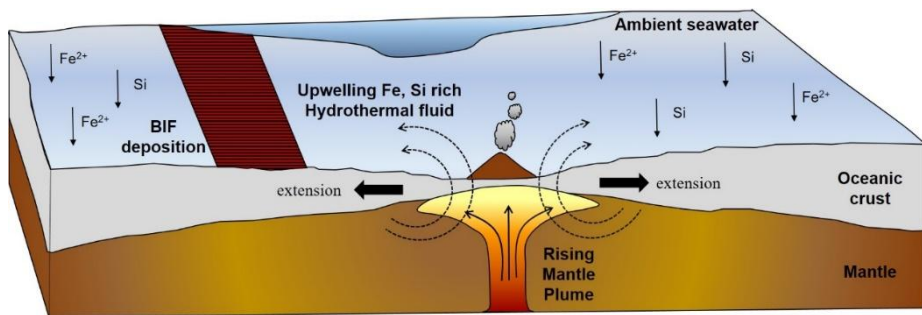


Figure 2.13. A cartoon illustrating of a possible genetic model of Algoma-type Yishui BIF related to a mantle plume.

Table 2.1. Major element compositions of the Yishui BIF and representative BIF values (wt.%).

Sample	MT-1	MT-2	MT-3	MT-4	11YZ-1	average	BIFs in NCC ^a	Algoma type ^b	Superior type ^b
SiO ₂	42.0	53.1	37.2	47.6	44.6	44.9	46.4	48.9	47.1
Al ₂ O ₃	0.57	0.42	1.18	0.54	0.45	0.63	0.8	3.7	1.5
TiO ₂	0.01	0.04	0.09	0.02	0.03	0.04	0.04		
Fe ₂ O ₃ ^T	43.9	40.4	55.4	46.7	51.2	47.5	48	39.7	40.3
MgO	1.76	2.52	3.75	3.64	2.52	2.84	2.41	2	1.93
CaO	6.56	1.33	1.67	0.95	0.91	2.29	1.8	1.87	2.24
Na ₂ O	0.14	0.27	0.21	0.06	0.03	0.14	0.29	0.43	0.13
K ₂ O	0.02	0.10	0.08	0.07	0.02	0.06	0.13	0.62	0.2
MnO	0.16	0.14	0.10	0.16	0.07	0.12	0.09		
P ₂ O ₅	0.03	0.04	0.14	0.06	0.06	0.07	0.14	0.23	0.08
LOI	4.65	1.21	0.10	0.13	0.11	1.24			
Total	99.7	99.6	99.9	100	100	99.8			
SiO ₂ +Fe ₂ O ₃ ^T	85.8	93.5	92.6	94.4	95.8	92.4	94.4	88.6	87.4
MnO/Fe ₂ O ₃ ^T	0.004	0.003	0.002	0.003	0.001	0.003	0.002		

Fe₂O₃^T = total Fe oxide

^a After Lan et al., 2014 (references therein).

^b After Gross and McLeod (1980).

Table 2.2. Trace element and REE composition of the Yishui BIF and Archean BIFs of the NCC (ppm).

Sample	MT-1	MT-2	MT-3	MT-4	¹¹ YZ- ₁	Average	Archean BIFs in the NCC ^a
Th	0.03	0.13	0.18	0.07	1.10	0.48	
Ni	2.42	2.43	3.89	6.92	3.56	3.84	
Sr	121	26.3	88.0	21.3	38.4	59.1	
Ba	11.9	1.73	9.03	9.47	1.94	6.82	
Zr	0.36	0.43	1.81	1.19	0.30	0.82	
Rb	0.48	0.31	0.27	1.00	0.69	0.55	
La	1.75	1.25	1.21	1.40	1.88	1.50	2.23
Ce	2.95	2.13	2.52	2.62	3.98	2.84	4.19
Pr	0.34	0.27	0.35	0.32	0.54	0.37	0.49
Nd	1.30	1.02	1.54	1.31	2.41	1.52	2.04
Sm	0.29	0.22	0.38	0.27	0.53	0.34	0.44
Eu	0.34	0.14	0.23	0.21	0.62	0.31	0.28
Gd	0.46	0.30	0.51	0.41	0.83	0.50	0.56
Tb	0.08	0.05	0.07	0.07	0.14	0.08	0.09
Dy	0.50	0.34	0.47	0.43	0.92	0.53	0.61
Y	4.94	3.09	4.14	3.26	5.52	4.20	5.03
Ho	0.13	0.09	0.10	0.11	0.23	0.13	0.15
Er	0.42	0.28	0.32	0.38	0.77	0.44	0.45
Tm	0.07	0.05	0.04	0.06	0.12	0.07	0.07
Yb	0.45	0.33	0.28	0.40	0.80	0.45	0.45
Lu	0.07	0.06	0.05	0.07	0.13	0.07	0.07
∑REE+Y	14.1	9.60	12.2	11.3	19.4	13.3	17.1
Y/Ho	37.7	35.4	40.1	28.5	23.8	33.1	34.6
La/La* _{SN}	1.16	1.05	1.13	1.14	1.18	1.13	1.24
Ce/Ce* _{SN}	0.94	0.87	0.94	0.96	0.97	0.94	0.91
Eu/Eu* _{SN}	4.18	2.44	2.44	2.85	4.19	3.22	2.31
Y/Y* _{SN}	1.53	1.43	1.51	1.16	0.95	1.31	1.05
Pr/Pr* _{SN}	1.03	1.07	1.03	1.02	1.01	1.03	1.00
La/Yb _{SN}	0.29	0.28	0.32	0.26	0.17	0.26	0.29

^a after Lan et al. (2014) and references therein.

Chapter 3. Archean tectonic evolution and the genetic link between wall rocks and BIFs in North China Craton

Abstract

The Yishui amphibolites in the North China Craton (NCC) occur interbedded with the Algoma-type Yishui BIFs as related wall rocks. The reconstruction of the protoliths for the amphibolites was conducted based on the results of petrological, mineralogical and geochemical analyses. The Yishui amphibolites are mainly composed of SiO_2 , $\text{Fe}_2\text{O}_3^{\text{T}}$, CaO and Al_2O_3 , with subordinate TiO_2 , MgO , Na_2O , K_2O , P_2O_5 and MnO . The chondrite-normalized REE diagram, characterized by enriched LREE ($\text{La}/\text{Yb}_{\text{CN}}=19.51\text{--}24.05$) with insignificant Eu and Ce anomalies, exhibits coherent trends. The primitive mantle-normalized multi-element spider diagram is enriched in LILE, HFSE and LREE which are related to a mantle source. The results, combined with previous literature data, indicate that the protoliths of the Archean basalts have an affinity with intraplate alkaline basalts and were derived from an ocean island basalt (OIB)-type mantle source with no contribution of contamination. In addition, they further suggest that the OIB-type basalts were primarily the products of low degrees of partial melting. Several tectonic models have been recommended to explain the tectonic evolution of the NCC. Based on the results of this study, we prefer the mantle plume model because this model can better explain the geochemical signatures of basalts, which have OIB-type affinity and formed in a within-plate

setting. Furthermore, the model can provide crucial information about Archean tectonic evolution in the NCC and can demonstrate the temporal and spatial relationships between BIFs and wall rocks.

3.1. Introduction

Precambrian banded iron formations (BIFs) are economically important sedimentary rocks that contain iron-rich layers and silica-rich layers. James (1954) defined BIFs as chemical sediments, typically thin bedded or laminated, containing 15% or more iron, of sedimentary origin, and commonly but not necessarily containing layers of chert. They mainly formed during 3.8 Ga to 1.8 Ga and reappeared from 0.8 Ga to 0.6 Ga. Among the periods, abundance of the BIFs are exclusively high at 2.5 Ga (Klein, 2005). Although their origin remains imperfectly understood, BIFs provide valuable information for understanding the evolution of the atmosphere and biosphere and coeval ocean composition (Bekker et al., 2010). Two main types of Precambrian BIFs are proposed by Gross (1980) based on related depositional settings and related rock associations, which are Superior-type BIFs and Algoma-type BIFs. Superior-type BIFs were formed in nearshore continental shelf environments, and they are related to carbonates, quartz arenite and black shale. In particular, Superior-type BIFs are insignificantly correlated with volcanic rocks. In contrast, Algoma-type BIFs are regarded to have been deposited in volcanic centres and have close relationships with volcanic rocks. Hence, the close relationship between the BIFs and the associated wall rock can be considered as a valuable proxy for understanding not only the reconstruction of the formation mechanism of BIFs but also the tectonic evolution of Archean cratons

(Sun et al., 2014b). Previous studies have focused on the relationships between the BIFs and wall rocks to evaluate their provenance and the tectonic evolution of China (Zhai et al., 1990; Lan et al., 2014a; Sun et al., 2014b).

From this point of view, the geochemical features of the associated wall rocks (amphibolites) are key to understanding the mantle sources and tectonic evolution history of the North China Craton (NCC) in Archean. Combined the results of this study, we used previously reported data from Wang et al. (2013) and Li et al. (2016). Hence, we plotted our data together with data from Wang et al. (2013) and Li et al. (2016) in several diagrams. Wang et al. (2013) studied geochemical signatures of enriched basalts in Liuhan formation and demonstrated that mantle plume was welling up beneath the Western Shandong Province (WSP) in Archean. Li et al. (2016) also contributed understanding of tectonic evolution processes in Archean WSP based on investigation of petrological, geochemical, geochronological data of metavolcanic rocks. In addition, the geochemical data of the Archean amphibolites and komatiites from Polat et al. (2006) and Cheng and Kusky (2007) in an adjacent area, Taishan Group (TG), provide useful information for further research. They characterized the geochemical signatures of komatiites and amphibolites, and inferred suitable tectonic model. We used geochemical data from Polat et al. (2006).

In this contribution, we focus on the petrogenesis of the Archean rocks in the WSP using trace elements (including REE) as a geochemical proxy. The aims of this study are: (1) to constraint the mantle sources of the Archean basalts in the NCC, (2) to provide an insight into the most reasonable Archean tectonic model of the NCC and (3) to understand genetic relationship between the amphibolite and

the BIF in study area.

3.2. Regional and local geology

The NCC is one of the oldest representative Precambrian cratons in the world and consists of the Archean to Paleoproterozoic Eastern and Western blocks and three Proterozoic orogenic belts: the Jiao–Liao–Ji Belt, the Khondalite Belt and the Trans–North China Orogen (Zhao et al., 2005; Wu et al., 2009; Zhai and Santosh, 2011) (Figure 3.1a). The Yinshan Block and Ordos Block collided to form the Khondalite Belt of the Western Block, and the Longgang Block and Langrim Block collided to form the Jiao–Liao–Ji Belt of the Eastern Block. The collision of the Western and Eastern Blocks formed the Trans–North China Orogen (Nutman et al., 2011; Zeng et al., 2011; Geng et al., 2012; Lv et al., 2012; Wu et al., 2013a). The Archean basement of the Eastern Block is composed of the Southern Jilin, North Liaoning, Anshan–Benxi, Southern Liaoning, Western Liaoning, Eastern Hebei, Miyun and Western and Eastern Shandong complexes and experienced deformation and greenschist– to amphibolite–facies metamorphism (Zhao et al., 1998; Zhai et al., 2005; Polat et al., 2006; Wan et al., 2011). The Neoproterozoic period between ~2.7 Ga and ~2.5 Ga was a significant time for crustal formation based on Nd isotope studies (Condie and O’Neill, 2009; Wan et al., 2011). Approximately 2.7 Ga, a tectonothermal event occurred in many cratons around the world; this time was an important period for the formation of Archean continental crust. However, ~2.5 Ga, a tectonothermal event occurred in only a few cratons such as the NCC (Wan et al., 2012a). Further, Paleoproterozoic rifting–subduction–accretion–collision tectonics and subsequent high–grade granulite–facies metamorphism–granitoid magmatism during ca. 2.0–1.82 Ga have been reported.

The Yishui amphibolites were collected from Liuhang formation of Yishui county in the WSP of the NCC. The WSP is located in the southeastern part of the NCC, which is called the granite–greenstone belt; it spreads across 15,000 km² and extends northwest to southeast (Jahn et al., 1988; Zeng et al., 2011; Peng et al., 2012). The WSP experienced multiple events of severe metamorphism, magmatism and deformation (Polat et al., 2006; Wan et al., 2011). The TG, which experienced strong deformation, occupies a large proportion of the WSP and is subdivided into the Yanlingguan, Shancaoyu, and Liuhang formations (Cao et al., 1996; Wan et al., 2011; Wang et al., 2013) (Figure 3.1b). The Yanlingguan formation is composed of komatiitic metavolcanic rocks, amphibolite and minor volumes of fine–grained biotite (\pm hornblende) gneiss (leptynite). The Shancaoyu formation consists of fine–grained biotite gneiss, fine–grained hornblende gneiss and minor amphibole schist. The Liuhang formation is lithologically composed of amphibolite, fine–grained biotite–hornblende gneisses, komatiitic rocks and schist. The Liuhang formation is divided into the upper part and the lower part. The former consists of Neoproterozoic metaconglomerate and fine–grained biotite gneiss, and the latter is composed of a thick metabasaltic lava sequence and minor biotite gneiss (Wan et al., 2012a). The Liuhang formation was formed 2.71 Ga based on the SHRIMP U–Pb zircon study (Wang et al., 2009). An insignificant contribution of contamination and well–developed geological structures indicates that the Liuhang formation was formed in a relatively deep marine environment (Wang et al., 2013).

The Algoma–type Yishui BIF is distributed in the upper part of the Liuhang formation (Figure 3.1c). The iron orebodies are exposed in outcrops and

are composed of three parts. The stratiform or sub-stratiform structure of the orebodies were mainly observed (Lai and Yang, 2012b). Plagioclase amphibolite and muscovite–quartz–schist are in contact with the ore bodies as shown in Figure 3.2a. The amphibolitic wall rock of Yishui BIF is indicative of the close relationship between BIF and volcanic activity. Based on the structure features, it is reasonable to infer that the Yishui BIF is included in the Algoma–type BIFs (Moon et al., 2017b).

3.3. Sample description and analytical methods

3.3.1. Sample description

The amphibolite core samples (depths from 53–72 m) are referred to as the Yishui amphibolite in this study. The amphibolites are interbedded with the Yishui BIF, which provides the principal evidence for an Algoma–type BIF, and are closely associated with migmatitic granite, schist and gneiss (Moon et al., 2017b). Based on macroscopic analyses, the amphibolites are dark green and mainly consist of fine– to coarse–grained minerals (Figure 3.2b–d).

Based on microscopic analyses, these rocks are mainly composed of amphibole (mostly ferrohornblende and actinolite), plagioclase (albite to oligoclase) and biotite with minor chlorite and clinopyroxene and variable amounts of opaque minerals (magnetite, chalcopyrite and pyrite). Altered hornblende, rare plagioclase sericitization and biotite chloritization, and the intergrowth of plagioclase and biotite are also observed. The rim of the amphibole is rarely clear because of alteration. Amphibole does not exhibit mineral foliation or lineation. Anhedral amphibole is pale brown to green, and subhedral to anhedral biotite is reddish

brown. Quartz has variable sizes larger than 90 μm , anhedral grains and observed undulose extinction. The typical assemblage of the amphibolite consists of amphibole, plagioclase, quartz, chlorite, biotite and magnetite (Figure 3.3).

3.3.2. Analytical methods

The EPMA, XRF and ICP–MS analyses were conducted at the National Centre for Inter–University Research Facilities (NCIRF) at Seoul National University (SNU).

Polished thin sections were prepared for mineral identification using a JEOL JXA–8900R electron probe microanalyzer (EPMA). The analytical conditions were as follows: accelerating voltage of 20 kV and beam size of 1 μm . Whole–rock powders were prepared for quantitative analysis. Major element abundances (SiO_2 , TiO_2 , Al_2O_3 , $\text{Fe}_2\text{O}_3^{\text{T}}$, MgO , MnO , CaO , Na_2O , K_2O , P_2O_5 and LOI) were determined by X–ray fluorescence spectroscopy (XRF) using a Shimadzu XRF–1700. The analytical uncertainties were generally within 0.1–1%. The LOI (Loss on ignition) represents the mass concentration of volatile or impurity materials lost from the sample and is determined by weight changes for samples; it was measured after heating to 950°C. For trace elements and rare earth element (REE) abundances, the samples were analysed with inductively coupled plasma mass spectrometry (ICP–MS) using ELAN 6100 and Perkin–Elmer SCIEX. The analytical conditions were 1 ml/min of injection flow rate, 0.3–3.0 amu of mass resolution, 1100 W RF (radio frequency) power and 6000 K argon plasma source.

3.4. Results

3.4.1. Major elements

The Yishui amphibolites have an almost uniform composition. They are mainly composed of SiO_2 , $\text{Fe}_2\text{O}_3^{\text{T}}$, CaO and Al_2O_3 , with subordinate TiO_2 , MgO , Na_2O , K_2O and P_2O_5 and minor MnO . The SiO_2 concentrations range from 35.1 to 44.2 wt.%, the Fe_2O_3 concentrations range from 15.9 to 22.0 wt.%, and the $\text{Na}_2\text{O}/\text{K}_2\text{O}$ ratios range from 1.2 to 5.4. The TiO_2 (1.6 to 5.1 wt.%), Al_2O_3 (8.5 to 10.6 wt.%), and P_2O_5 (1.2 to 1.5 and 8.7 wt.%) concentrations are relatively high. The samples have low MgO concentrations (from 3.2 to 4.5 wt.% with an average of 3.9 wt.%) and a low $\text{Mg}\#$ (from 25 to 30 with an average of 28). The LOI values scatter widely from 0.1 to 10.1. The values reflect the alteration effects on Archean volcanic rocks that experienced seafloor hydrothermal alteration and regional metamorphism.

3.4.2. Trace and rare earth elements

The chondrite-normalized REE patterns of the Yishui amphibolites are represented in Figure 3.4a, and their patterns exhibit coherent trends. The total REE concentrations of all samples are relatively high, ranging from 305 to 380 ppm (average $\sum\text{REE}=344$ ppm), which suggests a mantle origin (Barley, 1986). Their parallel patterns with strongly enriched LREE instead of HREE are consistent with those of typical Archean basalts. The normalized diagrams are characterized by relatively strong fractionation between LREE and HREE (average of $\text{La}/\text{Sm}_{\text{CN}}$ is 1.93 and average of $\text{La}/\text{Yb}_{\text{CN}}$ is 21.4) and insignificant Ce anomalies (average of $\text{Ce}/\text{Ce}_{\text{CN}}^*$ is 1.02) and Eu anomalies (average of $\text{Eu}/\text{Eu}_{\text{CN}}^*$ is 0.93). The primitive mantle-normalized trace element spider diagram is shown in Figure 3.4b, with

enriched large-ion lithophile elements (LILE) and high field strength elements (HFSE). The Yishui amphibolites display a relatively narrow variation, with slight enrichment in Nb and depletion in Ti. CN and PM represent normalization to chondrite and primitive mantle values, respectively. The Yishui amphibolites have high Sr (average of 1194 ppm), Ba (average of 589 ppm) and Ti (average of 24458 ppm) abundances.

3.5. Discussion

3.5.1. Protolith reconstruction

3.5.1.1. Evaluation of element mobility

The elemental behaviour of metamorphic rocks should be carefully considered because these rocks experienced deformation, seafloor hydrothermal alteration, and metamorphism during more than one event (Gómez-Pugnaire et al., 2003; Wang et al., 2015c). The study area experienced deformation and greenschist- to granulite-facies metamorphism (Zhao et al., 1998). Immobile elements and their ratios are used as reliable indicators to clarify the origins of metamorphic rocks because they are not affected by fractional crystallization and crustal contamination (Pearce and Peate, 1995; Condie, 2003, 2005; Pearce, 2008; Ilnicki, 2012). The chondrite-normalized REE and primitive mantle-normalized multi-element spider diagrams of Yishui amphibolites show almost coherent trends. In other words, the degree of conformity for the normalized REE and multi-element patterns of the Yishui amphibolites is relatively high. The stable geochemical signatures suggest that the pre- and post-alteration and metamorphism did not affect their original trace element concentrations

(Manikyamba and Kerrich, 2011; Lan et al., 2014a; Li et al., 2015; Wang et al., 2015c). Consequently, immobile elements are used to identify the magmatic affinity and petrogenesis of the Yishui amphibolites in the following discussion.

3.5.1.2. Petrological classification

The Nb/Y vs. Zr/(TiO₂ * 1000) diagram (Figure 3.6) confirms that the protolith of all Yishui amphibolites can be classified as alkali basalt. The Nb/Y ratio is an index of the alkalinity of volcanic rocks (Li et al., 2000). However, the result of the above-mentioned discrimination diagram is inconsistent with the results of the (Na₂O + K₂O) vs. SiO₂ discrimination diagram (Le Bas et al., 1992). Based on the element behaviour, the immobile element discrimination diagram is more suitable than the major element discrimination diagram. Enriched basalts (Wang et al., 2013) and metavolcanic rocks (Li et al., 2016) are also plotted in the diagram and they show alkali basalt affinity. Alkaline magma activity is uncommon not only in the Archean and Early Proterozoic but also at present (Blichert-Toft et al., 1996; Manikyamba and Kerrich, 2011). Hence, the geochemical signature of alkaline basalts provides significant insights into geodynamic processes of the past.

3.5.1.3. Crustal contamination

Crustal assimilation must be considered as a magmatic differentiation process (Zhu et al., 2016). The Lu/Yb (0.13), Nb/La (1.10), Rb/La (0.93), Nb/Ta (17.5), and Pb/Nb (0.15) ratios in this study are similar to primitive mantle values (Taylor and McLennan, 1985; Sun and McDonough, 1989; Pearce and Peate, 1995; Condie, 2005; Pearce, 2008; Zhou et al., 2009; Dai et al., 2011). The Th/La (0.09),

Th/Yb (2.60), Ce/Pb (16.4), La/Ta < 22, La/Nb < 1.5, Nb/U > 40 and Th/Nb < 1 of the spider diagrams are typically indicative of a lack of contribution from continental crust (Hofmann et al., 1986; Zeng et al., 2010; Ilnicki, 2012). In addition, the coherent normalized elemental patterns and their narrow ranges indicate no crustal contamination during magma ascent, which suggests that the protolith of the Yishui amphibolites was mainly controlled by a mantle source and that continental crust only minimally contributed to the melting conditions. Wang et al. (2013) and Li et al. (2016) also suggested negligible crustal contamination in the study area.

3.5.2. Petrogenetic interpretation

3.5.2.1. Sources of mantle in the NCC

Enriched LILE, HFSE, LREE and insignificant Eu and Ce anomalies suggest that the primary features of the Yishui amphibolites resemble those of a typical OIB-type magma source, precluding the possibility of MORB, oceanic plateau basalt, and continental margins (Zhou et al., 2009; Ilnicki, 2012). The Ta/Yb vs. Th/Yb (Figure 3.7), Nb/Yb vs. TiO₂/Yb (Pearce, 2008), Th/Nb vs. Ce/Nb (Saunders et al., 1988), La/Yb vs. Th/Ta (Pearce, 1982) and Nb vs. Nb/U (Hofmann et al., 1986; Kepezhinskas et al., 1997) projections and La/Th, Nb/Th, K/Zr, Ba/Zr, Ba/Nb, Ba/Ce, La/Nb, Zr/Nb, Sm/Nd and Zr/Y ratios clearly indicate that all Yishui amphibolites have OIB affinity (Zhu et al., 2016). The sources of the protoliths of the Yishui amphibolites are homogeneous. In addition, OIB-type basalts have been recognized at enriched basalts (Figure 3.4c, d) and metavolcanic rocks (Figure 3.4e, f) and these results provide an opportunity to examine the

sources of the mantle beneath the WSP at Archean. The low Y/Nb and Zr/Nb concentrations and high Sr concentrations of Yishui amphibolites are indicative of the geochemical values of an enriched mantle source (Wilson, 2007; Ilnicki, 2012; Wang et al., 2015c). The trend of incompatible elements increases with decreasing degree of melting (Zeng et al., 2010), which indicates that the mantle sources in this study originated by a low degree of partial melting. Generally, the OIB-like basalt is considered to be derived from a mantle plume-related source and is referred to as enriched mantle (White, 2010; Ilnicki, 2012). As shown in Figure 3.8, the parental magma of the Yishui amphibolites was generated at approximately 4.0 GPa (depth of 120–135 km; upper mantle environment) with low partial melting (approximately 1%) based on the model of Pearce (2008). However, the enriched basalts and metavolcanic rocks plot in the fields of 2.0–3.0 GPa and 3.5–4.0 GPa, respectively with considerably high degrees of partial melting. The results are inconsistent with those from Wang et al. (2013) and Li et al. (2016). They suggested different point of view based on their research. Wang et al. (2013) provided supporting evidence for the petrogenesis of the enriched basalts. The enriched basalts in the Liuhan basaltic lava sequence are less than 5% in volume and are characteristically depleted in MgO and enriched in HFSE and LREE. Based on their lithological and geochemical features, the enriched basalts are characterized as transitional to alkaline basalts and might have originated directly from lower-degree partial melting of a mantle plume or from a mixture of LREE-depleted and more LREE-enriched (OIB-like) melts in an upwelling mantle plume (Wang et al., 2013). Similar geochemical features, including basaltic origin and high concentrations of REE and HFSE, were also reported in metavolcanic rocks

by Li et al. (2016). According to their geochemical and chronological data with previous literature, they suggested that the study area was affected by the underplating of mantle derived magma. These Archean rocks therefore indicate that the alkali basalts in the Archean WSP were originated from OIB-like magma generated by a low degree of partial melting of asthenospheric mantle.

However, non-OIB affinities are also reported in the TG. The chondrite-normalized REE and primitive mantle-normalized multi-element spider diagrams of amphibolites and komatiites of the TG from Polat et al. (2006) are suggestive of a MORB origin and preclude the possibility of an OIB origin (Figure 3.5). Based on geochemical, geochronological and mineralogical research of the amphibolites and komatiites, they suggested that a tectonic model of plume-craton interaction was the most reasonable tectonic model for the Archean WSP (Polat et al., 2006; Cheng and Kusky, 2007). As a consequence, despite the different magma sources, our data coupled with published data of Archean samples from the WSP are thought to be products derived from a mantle plume. The diverse mantle sources of the Archean NCC might reflect the partial melting of heterogeneous mantle sources by the mantle plume. Tang et al. (2013b) also suggested the highly heterogeneous lithosphere mantle of the Archean NCC.

3.5.2.2. Tectonic significance

The Ti vs. V diagram provides a standard to determine possible tectonic settings (Shervais, 1982). The Ti/V ratio of the Yishui amphibolites varies from 119 to 309 due to high Ti concentrations. The Ti/V ratios of island arc tholeiite (IAT) and back-arc basin tholeiite (BAT) vary from 10 to 20, those of MORB and

continental flood basalts vary from 20 to 50, and those of OIB and alkali basalt vary from 50 to 100. A Ti/V ratio > 100 places the rocks into the field of within-plate basalt. The values of Ti/V ratio in Yishui amphibolites are larger than 100 and those of the metavolcanic rocks vary from 50 to 100. The former indicates a feature of within-plate basalt, and the latter represents a signature of OIB-type alkaline basalts. In the Nb–Zr–Y diagram (Figure 3.9), the samples of Yishui amphibolites, enriched basalts and metavolcanic rocks are located in and near the within-plate alkali basalts, suggesting that their protoliths formed in an intraplate environment. Intraplate tectono–magmatic phenomena have a close relationship with a deep mantle plume and decompression asthenospheric upwelling (Pirajno, 2007).

3.5.3. Genetic relationship between amphibolite and Yishui BIF

Geochemical data make it possible to determine the original tectonic environment (Gill, 2010). Moon et al. (2017b) revealed the genetic mechanism for the Yishui BIF based on geological, petrological and geochemical data. They concluded that the Algoma-type Yishui BIF was precipitated from a mixture of seawater and high-temperature hydrothermal input under submarine conditions with insignificant influences from continental sources. The deposition site of the Yishui BIF was closely related to volcanic activity. In addition, a mantle plume model would be proposed as the most reasonable tectonic model.

According to the results of geochemical signatures and discrimination diagrams in this study, the protoliths of the Yishui amphibolites (intraplate alkaline basalts) are geochemically akin to the OIB-type basalts and derived from a low degree of partial melting of an asthenospheric mantle. As explained above, OIB–

type basalts are generally associated with mantle plumes and considered to originate from the upper mantle and crust through melting (White, 2010). Furthermore, intraplate magma has also been closely linked with both asthenospheric upwelling and deep mantle plumes (Pirajno, 2007). Based on the combined research on the Yishui amphibolite and the Yishui BIF, the mantle plume model may be chosen as the most appropriate tectonic model. In other words, the mantle plume model suggests a framework for the understanding of not only the petrogenesis of the Yishui amphibolite and but also the genesis of the Yishui BIF.

Further, Algoma-type BIFs and related volcanic rocks have been considered to have formed synchronously in the Archean (Gross, 1980). Lai and Yang (2012a) conducted zircon U–Pb analyses on the amphibolites of the same samples as in this study. The combined geochemical fingerprints confirm that the Yishui BIF and the related amphibolite were formed in a tectonic setting related to a mantle plume at 2.6 Ga.

As consistent with the results of this study, the mantle plume was located under the WSP at 2.6–2.5 Ga. The study area was related to mantle-derived magma, and the plume head ascended toward the upper mantle or lower crust. Lithospheric stretching yielded ultramafic to mafic volcanic rock eruptions. Heat transfer led to the extensive partial melting of basaltic or amphibolitic rocks and regional metamorphism (Wu et al., 2012). These tectonic thermal events are the crucial evidence to identify, as well as the geological properties of the WSP and the genetic link between the Yishui amphibolite and the Yishui BIF.

3.5.4. Implications for the evolution of the Eastern Block of the NCC

The Neoproterozoic was an important period for the growth of the NCC. Previous studies have revealed that two main tectonothermal events occurred in the WSP at ~2.7 Ga and ~2.5 Ga (Wan et al., 2011; Wan et al., 2012a). The large-scale but short ~2.7 Ga tectonothermal event occurred around the world, whereas the ~2.5 Ga tectonothermal event occurred in only a few places, including the NCC. Hence, the NCC preserves the ~2.7 Ga tectonothermal and crust-forming event, as do many cratons around the world, but with an overprinted strong ~2.5 Ga tectonothermal event (Wan et al., 2012a; Sun et al., 2014b). The tectonic evolution of the NCC remains controversial. Some researchers insist on a continental arc environment, whereas others suggest a mantle plume model (Zhao et al., 1998; Zhao et al., 2001; Wang et al., 2012; Wu et al., 2012; Wang et al., 2013; Wu et al., 2013a). Many researchers have previously studied the tectonic evolution of the NCC in Yishui County, TG, Western Shandong Province (Polat et al., 2006; Wan et al., 2012a; Wu et al., 2012). Polat et al. (2006) studied the geological and geochemical signatures of the TG using komatiites and associated basalts. In this study, a model of plume-craton interaction was suggested as a suitable tectonic model for explaining the crustal evolution of the TG in the Neoproterozoic. Wu et al. (2012) studied the petrology and P-T path of the mafic granulites from the Yishui area. Their petrologic, mineralogic and geochemical results and anticlockwise P-T path involving isobaric cooling suggested the presence of a mantle plume beneath the study area at 2.6–2.5 Ga. Hence, they proposed three metamorphic stages, which are pre-peak (M1), peak (M2) and post-peak (M3). In addition, the protoliths of rocks in Yishui County are bimodal volcanics, mainly basic and acid, further indicating that the Yishui area was considered to have evolved in an

extensional setting (Hamilton, 2011). In addition, Wang et al. (2013) conducted a geochemical study on Archean voluminous tholeiites and a minor volume of enriched basalts in the same study area. They concluded that the TG had formed from an upwelling mantle plume within an ocean basin. The minor volume of enriched basalts especially was directly derived from a lower degree of partial melting in the mantle plume. Based on all of the results of the previous studies, we infer that the study area evolution fits an upwelling mantle plume model.

Combining all previous results with those of this study, we propose a brief tectono–thermal evolution scenario for the Western Shandong Province in the Eastern Block of the NCC during the Neoproterozoic as shown in Figure 3.10. The Yishui BIF and the amphibolite as related wall rock were temporally and spatially linked, indicating the typical signatures of Algoma–type BIFs. Finally, we positively propose the mantle plume model in the NCC at 2.6 Ga.

3.6. Conclusions

- (1) Archean alkali basalts in the WSP of NCC have OIB and N–MORB affinity, indicating mantle heterogeneity.
- (2) Based on interpretations of the geochemical data and discrimination diagrams, the Yishui amphibolites are reminiscent of OIB and formed in an intraplate setting with no crustal assimilation during magma ascent. Combining previous and present results, the Yishui amphibolites are found to be genetically linked to the Yishui BIF.
- (3) We prefer the mantle plume model, which can explain the geochemical signatures of Archean basalts in NCC. In addition, the model is very

consistent with the tectonic evolutionary history of the NCC.

References

- Bekker, A., Slack, J.F., Planavsky, N., Krapež, B., Hofmann, A., Konhauser, K.O., and Rouxel, O.J., 2010, Iron formation: The sedimentary product of a complex interplay among mantle, tectonic, oceanic, and biospheric processes. *Economic Geology*, 105, 467-508.
- Blichert-Toft, J., Arndt, N., and Ludden, J., 1996, Precambrian alkaline magmatism. *Lithos*, 37, 97-111.
- Cao, G., Wang, Z., Cheng, Z., Dong, Y., Li, P., Wang, S., Jin, L., Shen, K., Xu, J., and Shen, K., 1996, Early Precambrian geology of western Shandong. Geol. Publ. House, Beijing, 1-210.
- Cheng, S., and Kusky, T., 2007, Komatiites from west Shandong, North China craton: implications for plume tectonics. *Gondwana Research*, 12, 77-83.
- Condie, K.C., 2003, Incompatible element ratios in oceanic basalts and komatiites: tracking deep mantle sources and continental growth rates with time. *Geochemistry, Geophysics, Geosystems*, 4, 1-28.
- Condie, K.C., 2005, High field strength element ratios in Archean basalts: a window to evolving sources of mantle plumes? *Lithos*, 79, 491-504.
- Condie, K.C., and O'Neill, C., 2009, A new perspective on the 2.7 Ga event on Earth. *Geochimica et Cosmochimica Acta*, 73, A240.
- Dai, J., Wang, C., Hébert, R., Li, Y., Zhong, H., Guillaume, R., Bezaud, R., and Wei, Y., 2011, Late Devonian OIB alkaline gabbro in the Yarlung Zangbo suture zone: remnants of the Paleo-Tethys? *Gondwana Research*, 19, 232-243.
- Floyd, P., and Winchester, J., 1975, Magma type and tectonic setting discrimination

- using immobile elements. *Earth and Planetary Science Letters*, 27, 211-218.
- Geng, Y., Du, L., and Ren, L., 2012, Growth and reworking of the early Precambrian continental crust in the North China Craton: constraints from zircon Hf isotopes. *Gondwana Research*, 21, 517-529.
- Gill, R., 2010. *Igneous rocks and processes: a practical guide*. John Wiley & Sons.
- Gómez-Pugnaire, M., Azor, A., Fernández-Soler, J., and Sánchez-Vizcaino, V.L., 2003, The amphibolites from the Ossa–Morena/Central Iberian Variscan suture (Southwestern Iberian Massif): geochemistry and tectonic interpretation. *Lithos*, 68, 23-42.
- Gross, G.A., 1980, A classification of iron formations based on depositional environments. *The Canadian Mineralogist*, 18, 215-222.
- Hamilton, W.B., 2011, Plate tectonics began in Neoproterozoic time, and plumes from deep mantle have never operated. *Lithos*, 123, 1-20.
- Hofmann, A., Jochum, K., Seufert, M., and White, W., 1986, Nb and Pb in oceanic basalts: new constraints on mantle evolution. *Earth and Planetary Science Letters*, 79, 33-45.
- Hu, B., Zhai, M., Li, T., Li, Z., Peng, P., Guo, J., and Kusky, T.M., 2012, Mesoproterozoic magmatic events in the eastern North China Craton and their tectonic implications: Geochronological evidence from detrital zircons in the Shandong Peninsula and North Korea. *Gondwana Research*, 22, 828-842.
- Ilnicki, S., 2012, Amphibolites from the Szklarska Poręba hornfels belt, West Sudetes, SW Poland: magma genesis and implications for the break-up of Gondwana. *International Journal of Earth Sciences*, 101, 1253-1272.
- Jahn, B., Auvray, B., Shen, Q., Liu, D., Zhang, Z., Dong, Y., Ye, X., Zhang, Q., Cornichet, J., and Mace, J., 1988, Archean crustal evolution in China: the Taishan complex, and evidence for juvenile crustal addition from long-term depleted mantle. *Precambrian Research*, 38, 381-403.
- James, H.L., 1954, Sedimentary facies of iron-formation. *Economic Geology*, 49, 235-293.
- Kepezhinskas, P., McDermott, F., Defant, M.J., Hochstaedter, A., Drummond, M.S., Hawkesworth, C.J., Koloskov, A., Maury, R.C., and Bellon, H., 1997,

- Trace element and Sr- Nd-Pb isotopic constraints on a three-component model of Kamchatka Arc petrogenesis. *Geochimica et Cosmochimica Acta*, 61, 577-600.
- Klein, C., 2005, Some Precambrian banded iron-formations (BIFs) from around the world: Their age, geologic setting, mineralogy, metamorphism, geochemistry, and origins. *American Mineralogist*, 90, 1473-1499.
- Lai, X., and Yang, X., 2012a, Characteristics of the banded iron formation (BIF) and its zircon chronology in Yangzhuang, western Shandong. *ACTA PETROLOGICA SINICA*, 28, 3612-3622.
- Lai, X.D., and Yang, X., 2012b, Characteristics of the banded iron formation (BIF) and its zircon chronology in Yangzhuang, western Shandong. *ACTA PETROLOGICA SINICA*, 28, 3612-3622.
- Lan, T.-G., Fan, H.-R., Hu, F.-F., Yang, K.-F., Cai, Y.-C., and Liu, Y.-S., 2014, Depositional environment and tectonic implications of the Paleoproterozoic BIF in Changyi area, eastern North China Craton: Evidence from geochronology and geochemistry of the metamorphic wallrocks. *Ore Geology Reviews*, 61, 52-72.
- Le Bas, M., Le Maitre, R., and Woolley, A., 1992, The construction of the total alkali-silica chemical classification of volcanic rocks. *Mineralogy and Petrology*, 46, 1-22.
- Li, R., Pei, X., Yang, S., Wei, L., Li, Z., Yang, G., Xu, D., Liu, M., and Kou, T., 2015, Mid-Neoproterozoic Tadong amphibolites at the junction of the East Kunlun and Western Qinling Orogens—a record of continental rifting during the break-up of Rodinia. *International Geology Review*, 1-16.
- Li, S.-S., Santosh, M., Cen, K., Teng, X.-M., and He, X.-F., 2016, Neoproterozoic convergent margin tectonics associated with microblock amalgamation in the North China Craton: evidence from the Yishui Complex. *Gondwana Research*, 38, 113-131.
- Li, X.-H., Sun, M., Wei, G.-J., Liu, Y., Lee, C.-Y., and Malpas, J., 2000, Geochemical and Sm–Nd isotopic study of amphibolites in the Cathaysia Block, southeastern China: evidence for an extremely depleted mantle in the Paleoproterozoic. *Precambrian Research*, 102, 251-262.

- Lv, B., Zhai, M., Li, T., and Peng, P., 2012, Zircon U–Pb ages and geochemistry of the Qinglong volcano-sedimentary rock series in Eastern Hebei: implication for ~ 2500Ma intra-continental rifting in the North China Craton. *Precambrian Research*, 208, 145-160.
- Manikyamba, C., and Kerrich, R., 2011, Geochemistry of alkaline basalts and associated high-Mg basalts from the 2.7 Ga Penakacherla Terrane, Dharwar craton, India: an Archean depleted mantle-OIB array. *Precambrian Research*, 188, 104-122.
- Meschede, M., 1986, A method of discriminating between different types of mid-ocean ridge basalts and continental tholeiites with the Nb-Zr-Y diagram. *Chemical Geology*, 56, 207-218.
- Moon, I., Lee, I., and Yang, X., 2017, Geochemical constraints on the genesis of the Algoma-type banded iron formation (BIF) in Yishui County, Western Shandong Province, North China Craton. *Ore Geology Reviews*, 89, 931-945.
- Nutman, A.P., Wan, Y., Du, L., Friend, C.R., Dong, C., Xie, H., Wang, W., Sun, H., and Liu, D., 2011, Multistage late Neoproterozoic crustal evolution of the North China Craton, eastern Hebei. *Precambrian Research*, 189, 43-65.
- Pearce, J.A., 1982, Trace element characteristics of lavas from destructive plate boundaries. *Andesites*, 8, 525-548.
- Pearce, J.A., 2008, Geochemical fingerprinting of oceanic basalts with applications to ophiolite classification and the search for Archean oceanic crust. *Lithos*, 100, 14-48.
- Pearce, J.A., and Peate, D.W., 1995, Tectonic implications of the composition of volcanic arc magmas. *Annual Review of Earth and Planetary Sciences*, 23, 251-286.
- Peng, T., Fan, W., and Peng, B., 2012, Geochronology and geochemistry of late Archean adakitic plutons from the Taishan granite–greenstone Terrain: implications for tectonic evolution of the eastern North China Craton. *Precambrian Research*, 208, 53-71.
- Pirajno, F., 2007, Mantle plumes, associated intraplate tectono-magmatic processes and ore systems. *Episodes*, 30, 6.

- Polat, A., Li, J., Fryer, B., Kusky, T., Gagnon, J., and Zhang, S., 2006, Geochemical characteristics of the Neoproterozoic (2800–2700 Ma) Taishan greenstone belt, North China Craton: evidence for plume–craton interaction. *Chemical Geology*, 230, 60-87.
- Saunders, A., Norry, M., and Tarney, J., 1988, Origin of MORB and chemically-depleted mantle reservoirs: trace element constraints. *Journal of Petrology*, 415-445.
- Shervais, J.W., 1982, Ti-V plots and the petrogenesis of modern and ophiolitic lavas. *Earth and Planetary Science Letters*, 59, 101-118.
- Sun, S.-S., and McDonough, W., 1989, Chemical and isotopic systematics of oceanic basalts: Implications for mantle composition and processes. Geological Society, London, Special Publications, 42, 313-345.
- Sun, X.-H., Zhu, X.-Q., Tang, H.-S., Zhang, Q., Luo, T.-Y., and Han, T., 2014, Protolith reconstruction and geochemical study on the wall rocks of Anshan BIFs, Northeast China: Implications for the provenance and tectonic setting. *Journal of Geochemical Exploration*, 136, 65-75.
- Tang, Y.-J., Zhang, H.-F., Ying, J.-F., Su, B.-X., Chu, Z.-Y., Xiao, Y., and Zhao, X.-M., 2013, Highly heterogeneous lithospheric mantle beneath the Central Zone of the North China Craton evolved from Archean mantle through diverse melt refertilization. *Gondwana Research*, 23, 130-140.
- Taylor, S.R., and McLennan, S.M., 1985, The continental crust: its composition and evolution.
- Wan, Y., Dong, C., Liu, D., Kröner, A., Yang, C., Wang, W., Du, L., Xie, H., and Ma, M., 2012, Zircon ages and geochemistry of late Neoproterozoic syenogranites in the North China Craton: a review. *Precambrian Research*, 222, 265-289.
- Wan, Y., Liu, D., Wang, S., Yang, E., Wang, W., Dong, C., Zhou, H., Du, L., Yang, Y., and Diwu, C., 2011, ~ 2.7 Ga juvenile crust formation in the North China Craton (Taishan-Xintai area, western Shandong Province): further evidence of an understated event from U–Pb dating and Hf isotopic composition of zircon. *Precambrian Research*, 186, 169-180.
- Wang, E.D., Han, C.I., Xia, J.M., Fu, J.F., Li, G.S., Jia, S.S., and Men, Y.K., 2015,

- Geochemical characterization of Archaean amphibolites from the eastern part of Anshan–Benxi iron producing area, northeastern China: implication for tectonic setting of BIFs. *Geological Journal*.
- Wang, W., Liu, S., Wilde, S.A., Li, Q., Zhang, J., Bai, X., Yang, P., and Guo, R., 2012, Petrogenesis and geochronology of Precambrian granitoid gneisses in Western Liaoning Province: constraints on Neoproterozoic to early Paleoproterozoic crustal evolution of the North China Craton. *Precambrian Research*, 222, 290-311.
- Wang, W., Yang, E., Wang, S., Du, L., Xie, H., Dong, C., and Wan, Y., 2009, Petrography of the metamorphic pillow basalt and SHRIMP U–Pb dating of zircons from the intruding trondhjemite in Archean Taishan “group”, Western Shandong. *Geol Rev*, 55, 737-744.
- Wang, W., Yang, E., Zhai, M., Wang, S., Santosh, M., Du, L., Xie, H., Lv, B., and Wan, Y., 2013, Geochemistry of ~ 2.7 Ga basalts from Taishan area: Constraints on the evolution of early Neoproterozoic granite-greenstone belt in western Shandong Province, China. *Precambrian Research*, 224, 94-109.
- White, W.M., 2010, Oceanic island basalts and mantle plumes: the geochemical perspective. *Annual Review of Earth and Planetary Sciences*, 38, 133-160.
- Wu, M., Zhao, G., Sun, M., Li, S., Bao, Z., Tam, P.Y., Eizenhöfer, P.R., and He, Y., 2013, Zircon U–Pb geochronology and Hf isotopes of major lithologies from the Jiaodong Terrane: implications for the crustal evolution of the Eastern Block of the North China Craton. *Lithos*, 190, 71-84.
- Wu, M., Zhao, G., Sun, M., Yin, C., Li, S., and Tam, P.Y., 2012, Petrology and P–T path of the Yishui mafic granulites: implications for tectonothermal evolution of the Western Shandong Complex in the Eastern Block of the North China Craton. *Precambrian Research*, 222, 312-324.
- Wu, Y.B., Gao, S., Gong, H.J., Xiang, H., Jiao, W.F., Yang, S.H., Liu, Y.S., and Yuan, H.L., 2009, Zircon U–Pb age, trace element and Hf isotope composition of Kongling terrane in the Yangtze Craton: refining the timing of Palaeoproterozoic high-grade metamorphism. *Journal of Metamorphic Geology*, 27, 461-477.
- Zeng, G., Chen, L.-H., Hofmann, A.W., Jiang, S.-Y., and Xu, X.-S., 2011, Crust

- recycling in the sources of two parallel volcanic chains in Shandong, North China. *Earth and Planetary Science Letters*, 302, 359-368.
- Zeng, G., Chen, L.-H., Xu, X.-S., Jiang, S.-Y., and Hofmann, A.W., 2010, Carbonated mantle sources for Cenozoic intra-plate alkaline basalts in Shandong, North China. *Chemical Geology*, 273, 35-45.
- Zhai, M.-G., and Santosh, M., 2011, The early Precambrian odyssey of the North China Craton: a synoptic overview. *Gondwana Research*, 20, 6-25.
- Zhai, M., Guo, J., and Liu, W., 2005, Neoproterozoic to Paleoproterozoic continental evolution and tectonic history of the North China Craton: a review. *Journal of Asian Earth Sciences*, 24, 547-561.
- Zhai, M., Windley, B.F., and Sills, J.D., 1990, Archean gneisses, amphibolites and banded iron-formations from the Anshan area of Liaoning Province, NE China: Their geochemistry, metamorphism and petrogenesis. *Precambrian Research*, 46, 195-216.
- Zhang, S., 2010. *Geological Formation Names of China (1866—2000)*. Springer Science & Business Media.
- Zhao, G., Sun, M., Wilde, S.A., and Sanzhong, L., 2005, Late Archean to Paleoproterozoic evolution of the North China Craton: key issues revisited. *Precambrian Research*, 136, 177-202.
- Zhao, G., Wilde, S.A., Cawood, P.A., and Lu, L., 1998, Thermal evolution of Archean basement rocks from the eastern part of the North China Craton and its bearing on tectonic setting. *International Geology Review*, 40, 706-721.
- Zhao, G., Wilde, S.A., Cawood, P.A., and Sun, M., 2001, Archean blocks and their boundaries in the North China Craton: lithological, geochemical, structural and P-T path constraints and tectonic evolution. *Precambrian Research*, 107, 45-73.
- Zhou, M.-F., Zhao, J.-H., Jiang, C.-Y., Gao, J.-F., Wang, W., and Yang, S.-H., 2009, OIB-like, heterogeneous mantle sources of Permian basaltic magmatism in the western Tarim Basin, NW China: implications for a possible Permian large igneous province. *Lithos*, 113, 583-594.
- Zhu, C.Y., Zhao, G., Sun, M., Eizenhöfer, P.R., Liu, Q., Zhang, X., Han, Y., and

Hou, W., 2016, Geochronology and geochemistry of the Yilan greenschists and amphibolites in the Heilongjiang complex, northeastern China and tectonic implications. *Gondwana Research*.

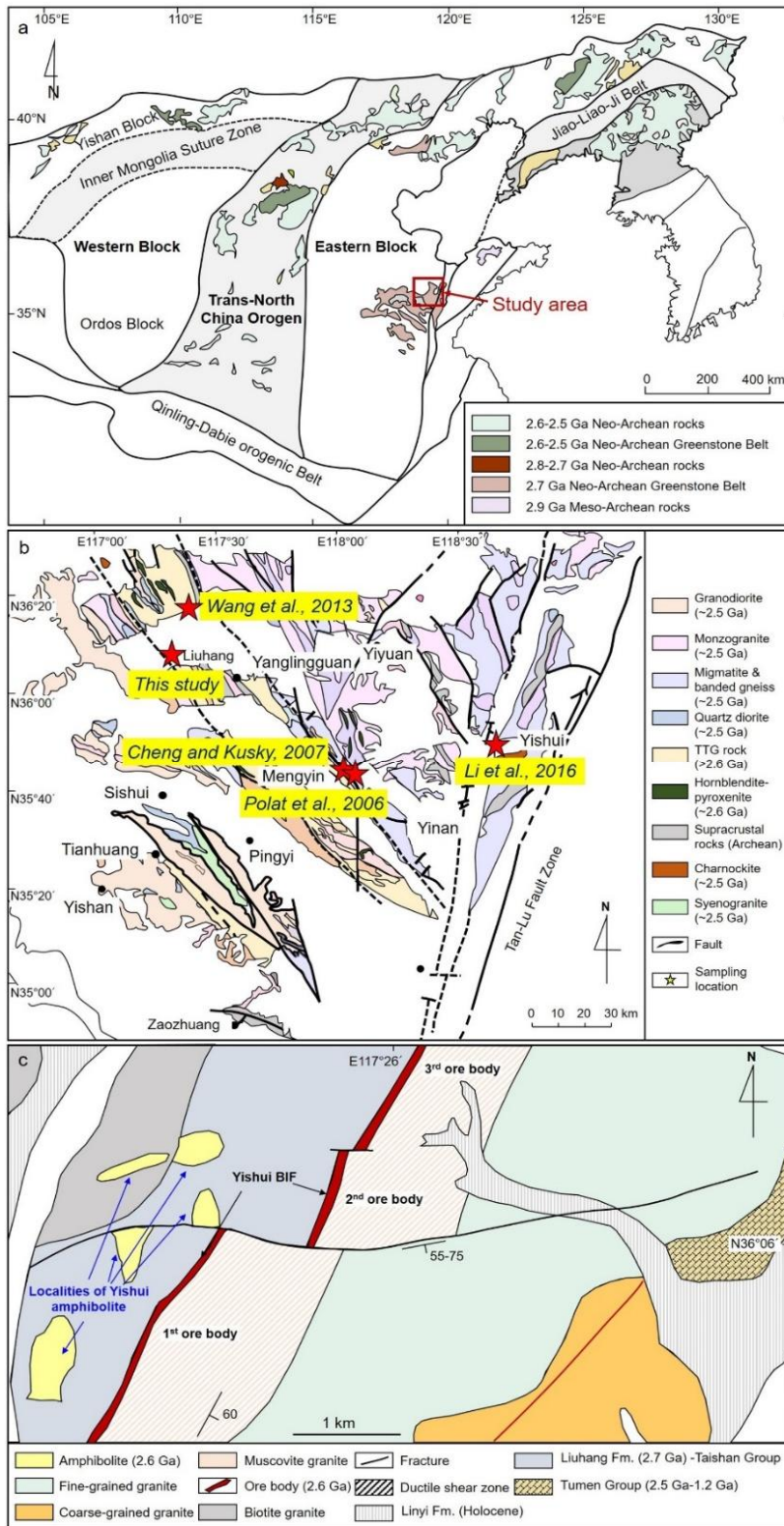


Figure 3.1. (a) Schematic tectonic map of the North China Craton (Zhao et al., 2005). (b) Geological sketch map of the Western Shandong Province (Wan et al., 2011). The locations of study area with comparable data from previous studies (Polat et al., 2006; Cheng and Kusky, 2007; Wang et al., 2013; Li et al., 2016) are marked red star. (c) Geological map of the Yishui BIF and Yishui amphibolite (Lai and Yang, 2012a). Abbreviations: Fm.=formation.

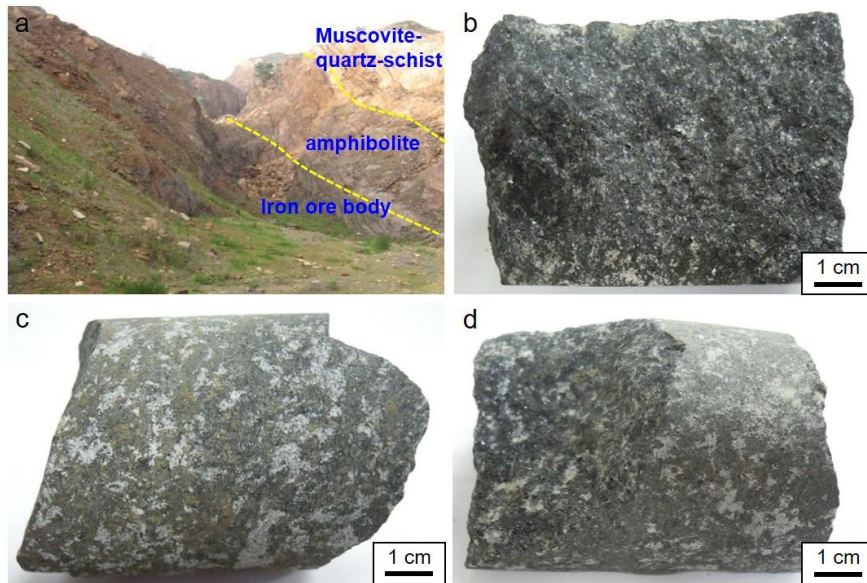


Figure 3.2. (a) Field photograph from the Yishui BIF and Yishui amphibolite. (b–d) Hand specimen photographs of amphibolites.

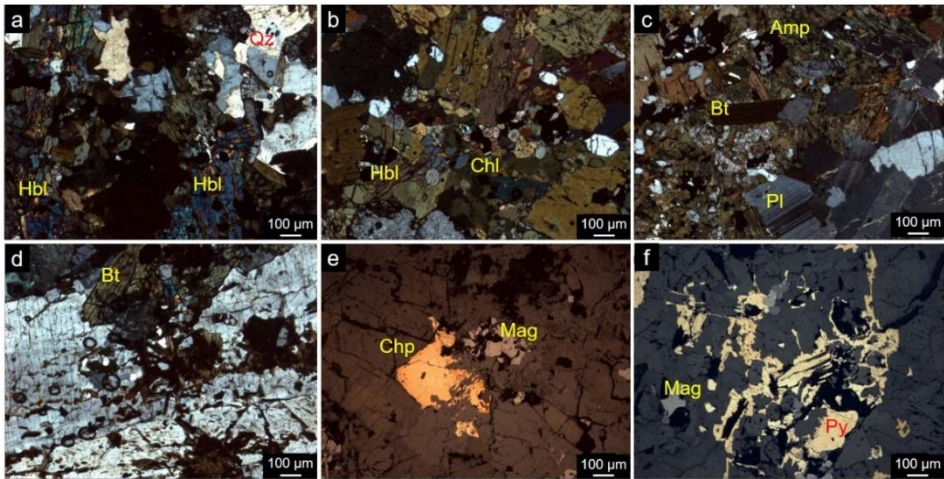


Figure 3.3. Representative photomicrographs of the Yishui amphibolites.

Abbreviations: Amp=amphibole; Hbl=hornblende; Chl=chlorite; Bt=biotite;

Q=quartz; Pl=plagioclase; Mag=magnetite; Chp=chalcopyrite; Py=pyrite.

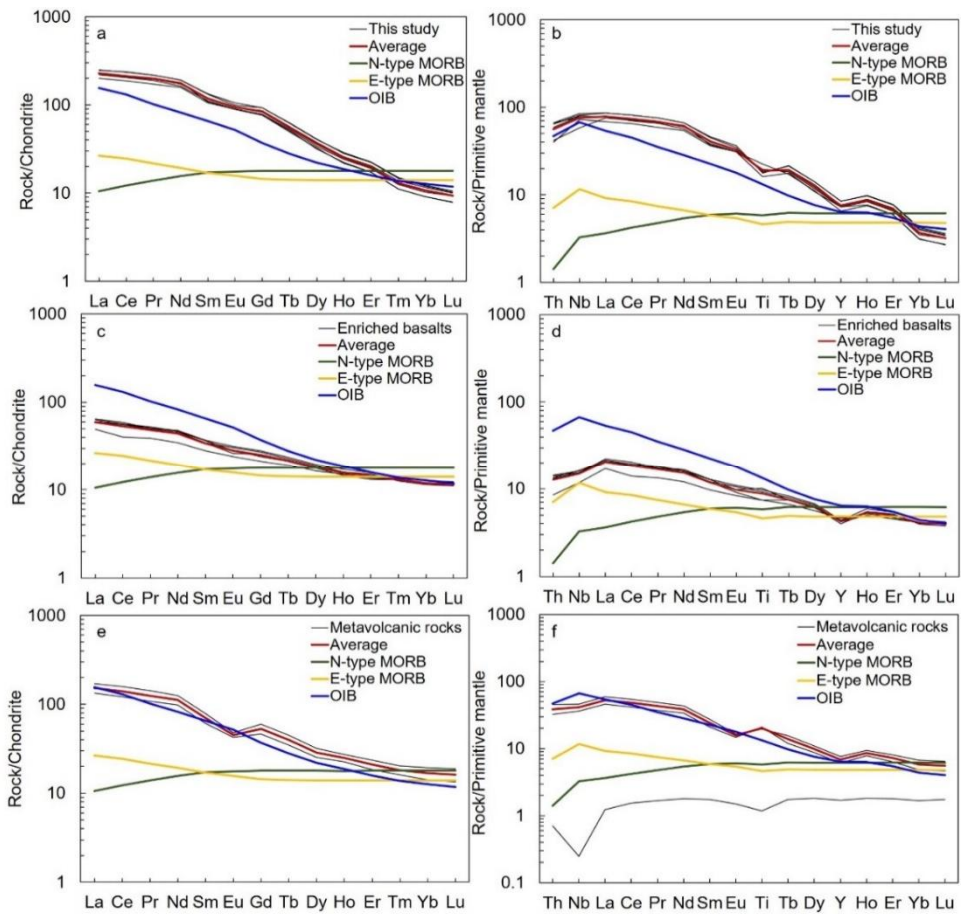


Figure 3.4. Chondrite-normalized REE patterns and primitive mantle-normalized multielement spider diagram of the Yishui amphibolites (a, b), enriched basalt (c, d) and metavolcanic rocks (e, f) from WSP. Chondrite and primitive mantle normalization values are from Sun and McDonough (1989). Enriched basalt and metavolcanic rocks values are from Wang et al. (2013) and Li et al. (2016), respectively. Oceanic island basalt (OIB), enriched mid-ocean ridge basalt (E-MORB) and normal mid-ocean ridge basalt (N-MORB) (Sun and McDonough, 1989) are plotted together for comparison.

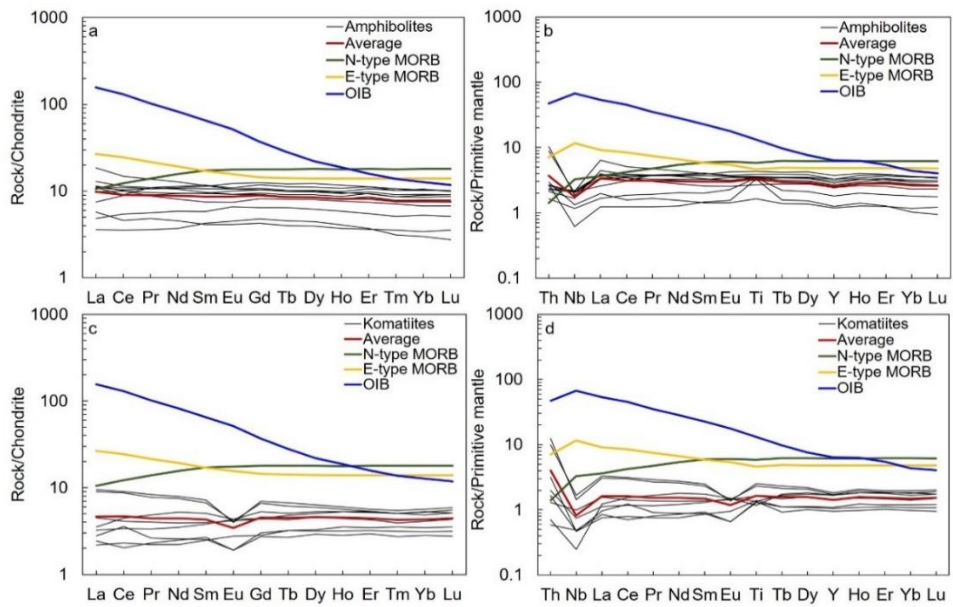


Figure 3.5. Chondrite-normalized REE patterns and primitive mantle-normalized multi-element spider diagram of the amphibolites (a, b), komatiites (c, d) from TG (Polat et al., 2006). The normalized values and comparable data are same with Figure 3.4.

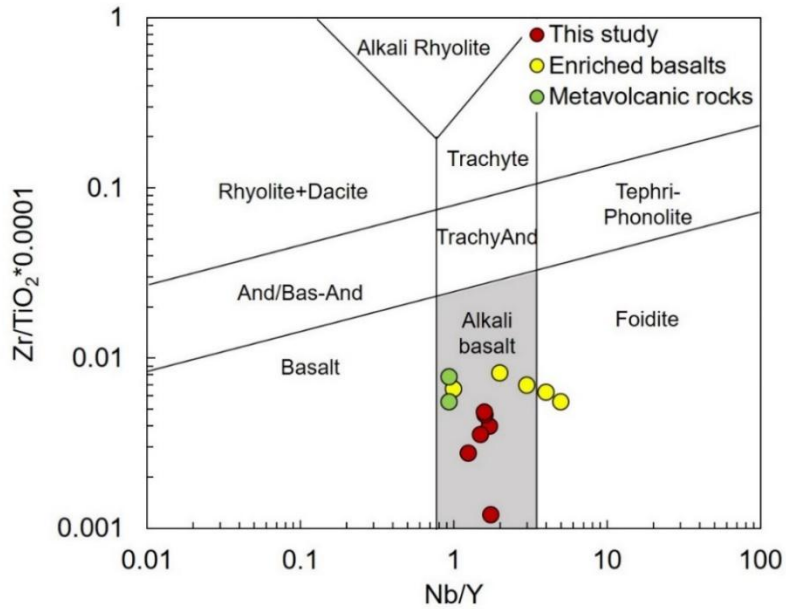


Figure 3.6. Geochemical classification diagram of Nb/Y vs. $Zr/TiO_2 * 0.0001$ (Floyd and Winchester, 1975).

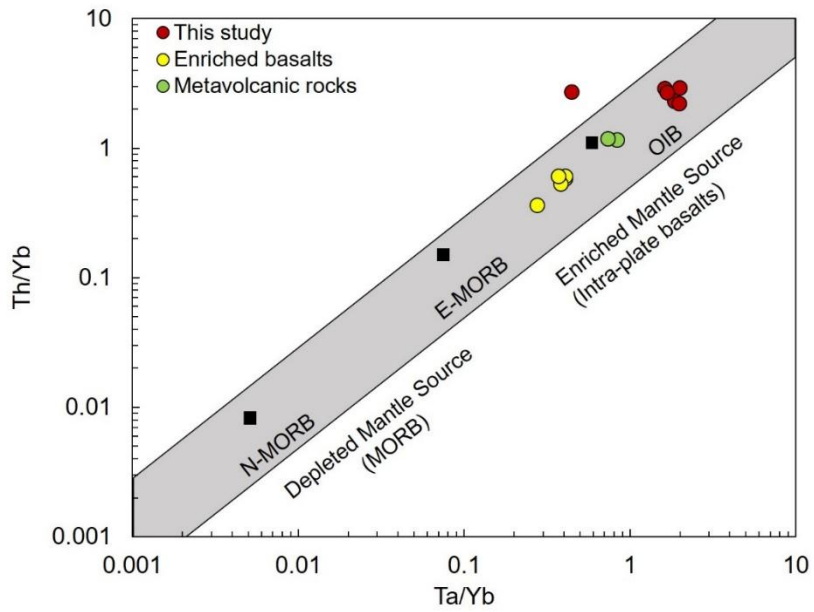


Figure 3.7. Ta/Yb vs. Th/Yb projections (Pearce, 1982).

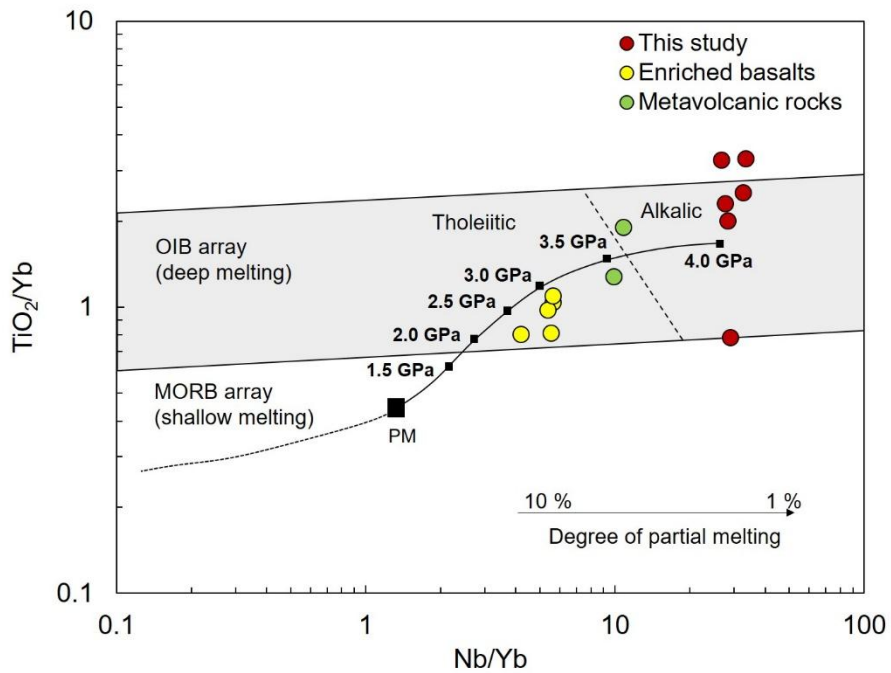


Figure 3.8. Nb/Yb vs. TiO₂/Yb and diagram with the mantle array (Pearce, 2008). The line indicates the melting model calculated by Pearce (2008) for a primitive mantle source at given pressures.

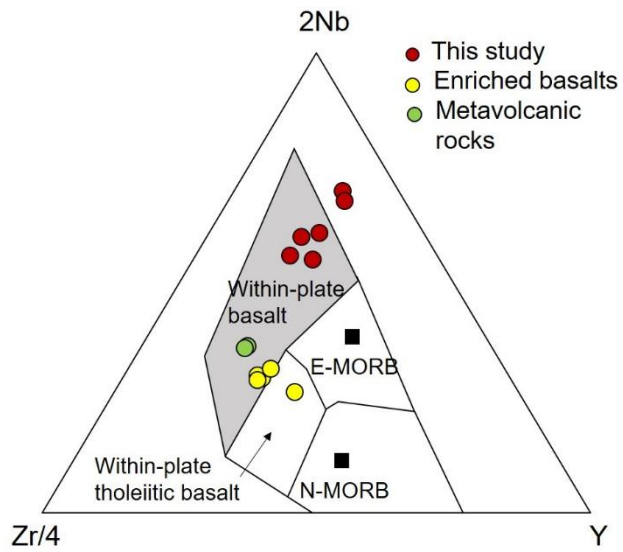


Figure 3.9. Nb–Zr–Y (Meschede, 1986) tectonic setting discrimination diagram.

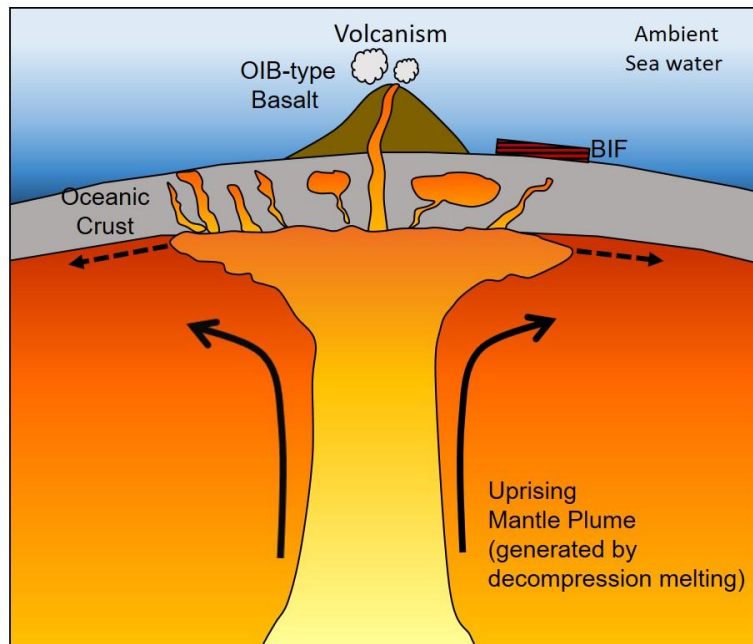


Figure 3.10. A simplified schematic sketch illustrating a possible tectonic model of a mantle plume based on geochemical data.

Chapter 4. Interpretation of formation condition in Superior–type banded iron formation (BIF) of Yuanjiacun in North China Craton using magnetite

Abstract

The superior–type Yuanjiacun banded iron formation (BIF) was formed during the Paleoproterozoic (~2.38–2.21 Ga) and distributed in the Shanxi Province of the North China Craton. The studied BIF is within the Yuanjiacun Formation of the lower part of the Luliang Group and precipitated along a stable continental shelf. The iron ore of the Yuanjiacun BIF has a layering structure that consists of magnetite–rich dark layers and quartz–rich light layers. The major minerals are magnetite and quartz with subordinate hematite, pyrite, amphibole, etc., varying in grain sizes. The grain size of magnetite is 20–180 μm and that of quartz is 50–500 μm . The main purpose of the study was to clarify the relationship between the timing for the formation of Yuanjiacun BIF and the coeval oxygen fugacity ($f\text{O}_2$) through Raman analysis of magnetite as a representative ore mineral in the BIF. Hematite spectra occurred at the edge of the some magnetite grains, representing change of oxidation level during the BIF formation. In addition, lack of negative Ce anomalies of iron ores from Yuanjiacun BIF indicates that $f\text{O}_2$ during their formation was enough for Fe^{2+} oxidation, but not enough for Ce^{3+} oxidation. Combined with previous geochemical data, the results of this study suggest that the Yuanjiacun BIF has close relationship with Great Oxidation Event.

4.1. Introduction

The banded iron formation (BIF) is defined as a chemical sediment, typically thinly bedded or laminated, whose principal chemical characteristic is an anomalously high iron content, commonly—but not necessarily—containing layers of chert (Klein, 2005; Bekker et al., 2010). These formations are the major sources of iron in the world. The genesis of BIFs is of considerable interest to many researchers (Hu et al., 2005; Bekker et al., 2010; Basta et al., 2011; Han et al., 2014; Sun et al., 2014a; Sun et al., 2014b; Yang et al., 2015; Wang and Zhang, 2016; Moon et al., 2017a). BIFs are thought to have formed by a mixture of seawater and hydrothermal fluids during the Precambrian. However, the mechanisms and processes for their formation are not clearly revealed (Bekker et al., 2010). The study of BIFs provides crucial information about the evolution of the early Earth and its atmosphere, the change of fO_2 , the role of cyanobacteria, etc (Ohmoto, 2003; Trendall, 2009). Typically, BIFs have iron- and silica-rich layers. The iron in the formation is precipitated as iron oxyhydroxide and transformed during diagenesis to magnetite or hematite (Posth et al., 2013). Their ores are mainly composed of quartz and magnetite with subordinate hematite and pyrite. BIFs are divided into Algoma-type and Superior-type BIFs based on formation age, tectonic setting, and the associated lithology. Algoma-type BIFs were precipitated in submarine conditions and have a close relationship with volcanic activity, whereas the Superior-type BIFs were formed in relatively stable tectonic settings, such as on the continental shelf (Gross, 1980).

BIFs are distributed throughout Australia, South Africa, Canada, Brazil, and China. Among them, the BIFs in China are mainly located on the North China

Craton (NCC) (Zhai and Windley, 1990; Zhai et al., 1990; Zhang et al., 2011). The NCC is one of the oldest cratons in Asia and has experienced a complex crustal evolution history (Bekker et al., 2010). Hence, the craton preserves many important geological events. The Yuanjiaocun BIF is located in the Shanxi Province on the NCC and is one of the largest open pit mines in Asia. It was formed around 2.3–2.1 Ga and is classified as a Superior–type BIF, which does not have a relationship with volcanic activity (Yu et al., 1997; Geng et al., 2000; Wan et al., 2000). The BIF was formed during the Great Oxidation Event (GOE) (Hou et al., 2014; Wang and Zhang, 2016).

Studies of BIFs were typically conducted assuming a formation model based on the formation age and mechanism (Isley and Abbott, 1999; Huston and Logan, 2004; Bolhar et al., 2005; Basta et al., 2011; Han et al., 2014; Lan et al., 2014b; Sun et al., 2014a; Sun et al., 2014b; Khalil et al., 2015; Yang et al., 2015; Zhu et al., 2015; Moon et al., 2017a). Recently, the study area has changed to study the crystal shape, grain size and the lattice of magnetite as a representative ore mineral in BIFs (Li et al., 2014a). In this study, we used Raman spectroscopic analysis on magnetite from the Yuanjiaocun BIF to reconstruct the formation environment and to understand the relationship between the BIF and the GOE.

4.2. Geological setting

China has some of the oldest cratons in the world, which consist of the North China Craton (NCC), South China Craton (SCC), and the Tarim Craton with its associated micro blocks. The South China Craton consists of two major blocks: the Yangtze Block to the northwest, which has a Late Archean–Paleoproterozoic

(1.7 Ga) nucleus, and the Cathaysia Block to the southeast, which has a Paleoproterozoic nucleus and amalgamated with the Yangtze Block along the Jiangshan–Shaoxing Fault during the Jinning Orogeny (Zhao et al., 2001; Zhao and Zhai, 2013; Zheng et al., 2013b; Li et al., 2014b). The craton consists of Early Archean to Paleoproterozoic basement overlain by Mesoproterozoic to Cenozoic unmetamorphosed cover. Metallogensis in the NCC is closely related to the major geological event. Almost all BIFs in China are distributed throughout the NCC, and this is where the Yuanjiaocun BIF is found, within the Yuanjiaocun Formation in the Lvliang Group (Figure 4.1) (Wu et al., 2012; Zhai and Santosh, 2013).

The Lvliang Group consists of greenschist– to amphibolite–facies metamorphosed sedimentary rocks, with banded iron formations (BIFs) in the lower sequence and metamorphosed volcanic rocks in the upper part of the sequence. The Lvliang Group also includes amphibolites, fine–grained felsic gneisses, schists, and tremolite–actinolite marbles. To the south of the Yuanjiaocun BIF, the degree of metamorphism increases, and chlorite–albite schists, sericite quartz schists, garnetite–chlorite schists, and amphibolites are found (Shen et al., 2010; Hou et al., 2014; Wang et al., 2015a).

4.3. Method

The electron probe micro analysis was conducted at Jeonju center of Korea Basic Science Institute. The instrument model was SHIMADZU 1600 and the experimental conditions were the following: standards and unknowns were analyzed with 1 μm beam diameter at an accelerating voltage of 15 kV and a beam current of 20 nA. The whole rock major and trace elements analyses were

completed by ACTLABS (Activation Laboratories Ltd.,) of Canada, using 4code LITHO.

The Raman Analysis was performed using a DXR Raman Microscope at the Tectonophysics Laboratory of Seoul National University. The laser power was 5.0 mw and the range of the spectral scan was between 99 and 1200 cm^{-1} . Additionally, the exposure time was 64 s. The 3–5 points were analyzed from core to rim.

The principle of Raman analysis is based on light scattering rather than absorption, it may be used in reflection mode on polished thin section. The inelastic scattering to the extent of elastic scattering is called Raman shift, and each mineral exhibits a strong spectral band at its inherent Raman shift depending on the constituent elements and molecular structure. The Raman spectrum of magnetite are 300 – 336 cm^{-1} , 533 – 570 cm^{-1} , 662 – 706 cm^{-1} . If metal trace elements are included in magnetite, the width of Raman spectrum range increases further (Shebanova and Lazor, 2003). Raman spectrum of hematite are various including 205 cm^{-1} , 224 – 228 cm^{-1} , 273 cm^{-1} , 288 – 294 cm^{-1} , 335 cm^{-1} , 408 – 413 cm^{-1} , 465 cm^{-1} , 580 cm^{-1} , 591 cm^{-1} , 669 cm^{-1} (Beattie and Gilson, 1970; Massey et al., 1990; Shim and Duffy, 2002; Murugappan et al., 2014; Drozdov et al., 2016). The Raman spectrum data of mineral were referred to the RRUFF project (<http://rruff.info/>). The differences and exceptionally observed Raman shifts are due to differences in interatomic oscillation energy and defects in the sample (Shebanova and Lazor, 2003).

4.4. Result

The iron ores from the Yuanjiacun BIF are mainly composed of magnetite and quartz, with subordinate biotite, amphibole, and pyrite. The grain sizes of magnetite and quartz are 20 – 180 μm and 50 – 500 μm , respectively. Typically, they show alteration of magnetite-rich layers and quartz-rich layers of 0.01 – 2 cm in scale (Figure 4.2a–d). The magnetite and hematite are distributed individually (Figure 4.2e), although they can also coexist on the edge of magnetite (Figure 4.2f).

The magnetite consists of FeO and Fe₂O₃, with less than 1 wt.% of Na₂O, MgO, Al₂O₃, SiO₂, P₂O₅, K₂O, CaO, TiO₂, and MnO. Iron concentrations are shown as FeO^T in the EPMA (Electron Probe Micro–Analyzer) analysis; this was first calculated for FeO = Fe₂O₃ * 0.8998 and then separated by FeO and Fe₂O₃ (Table 4.1).

The Ce and Pr anomalies were calculated by $\text{Ce}/\text{Ce}^* = \text{Ce}_{\text{PAAS}} / (0.5\text{Pr}_{\text{PAAS}} + 0.5\text{La}_{\text{PAAS}})$ and $\text{Pr}/\text{Pr}^* = \text{Pr}_{\text{PAAS}} / (0.5\text{Ce}_{\text{PAAS}} + 0.5\text{Nd}_{\text{PAAS}})$ (Bau and Dulski, 1996) and normalized to PAAS (Post–Archean Australian Shale). The range of the Ce anomalies were between 0.88 – 0.93 and the Pr anomalies ranged from 0.98 to 1.03 (Table 4.2).

The magnetite from the Yuanjiacun BIF have a Raman shift at 545 – 564 cm^{-1} , and 664 – 680 cm^{-1} (Figure 4.3a, b), while hematite was at 205 – 221 cm^{-1} , 265 – 280 cm^{-1} , 330 – 358 cm^{-1} , and 463 – 468 cm^{-1} (Figure 4.3c, d). The hematite spectrum was observed on the edge of magnetite (Figure 4.3e, f).

4.5. Discussion

4.5.1. The relationship between Yuanjiacun BIF and GOE

Li et al. (2014a) conducted a Raman spectroscopic analysis of magnetite in the Wuyang BIF, located to the southeast of North China. The Wuyang BIF is found in the Tieshanmiao Formation from the late Mesozoic era, and is classified into two types based on the composition. One is the quartz–magnetite BIF (QMB), which is predominantly quartz and magnetite, accompanied by a small amount of calcite. The other is also dominated by quartz and magnetite, but contains pyroxene and quartz pyroxene–magnetite (PMB). Raman spectroscopy was carried out from the edge of the magnetite to its center, resulting in the observation of a hematite spectrum at the edge of the magnetite. This indicates that magnetite and hematite coexist within the magnetite particles, and that the oxidation degree increases from the center of the magnetite to the edge. Also, the growth of hematite at the edges of the magnetite particles proves that the magnetite particles were affected by oxidation during recrystallization (Li et al., 2014a).

In this study, we carried out a Raman spectroscopic analysis of magnetite from the Yuanjiacun BIF. As is consistent with the results of Li et al. (2014a), it was confirmed that the hematite spectrum was observed, which is thought to be due to the increase in the degree of oxidation from the center to the edge of the particle.

The Ce anomaly is influenced by the La concentration, which is anomalous in seawater and marine sediments. In order to remove these factors, Bau and Dulski (1996) calculated Pr anomalies using Pr and Nd aberrations, which are not anomalous, and plotted a diagram using $(\text{Ce}/\text{Ce}^*)_{\text{PAAS}}$ and $(\text{Pr}/\text{Pr}^*)_{\text{PAAS}}$ (Figure 4.4). All of the ore from the Yuanjiacun BIF are shown in the II a area, which means that the Ce anomaly is not present. Furthermore, it means that the marine

environment in which the Yuanjiaocun BIF formed was reductive, unlike the present oxidative marine environment.

Hou et al. (2014) and Wang and Zhang (2016) carried out a study to reconstruct origin of the Yuanjiaocun BIF using rare earth elements, iron, oxygen, and silicon isotopes, together with a study of the lithology and mineralogy. According to the results of the study, the shallow ocean environment at the time of the formation (Paleoproterozoic) of the Yuanjiaocun BIF gradually became oxygen rich due to the global increase in atmospheric oxygen (GOE). There was a vertical environmental change in the deep-sea oxidizing environment, and the oxidation of Fe^{2+} to Fe^{3+} , along with the subsequent sedimentation, occurred in the oxidation-reduction transition zone. It is known that the formation phase of the Yuanjiaocun BIF occurred between 2.3 – 2.1 Ga at which time, significant oxidation occurred (2.4 – 2.0 Ga) (Wang and Zhang, 2016). In other words, the $f\text{O}_2$ in the atmosphere increased due to oxidation during the formation of the Yuanjiaocun BIF, and so hematite was found at the edge of magnetite.

To understand the overall oxidizing environment during the formation of the Yuanjiaocun BIF, Figure 4.4 shows the Yuanjiaocun BIF together with the results from Hou et al. (2014) and Wang et al. (2014). The ores were plotted in the I, IIa and IIIa regions, which means that they show no, or positive, Ce anomalies. In general, there is a pronounced negative Ce anomaly in present oxidized seawater and lack of a negative anomaly in suboxic and anoxic environments (Wang et al., 2014). Therefore, it is concluded that the Yuanjiaocun BIF was formed in a dominantly reduction environment, and at the transition zone between oxidation and reduction in the deep sea.

According to the results of the study, the fO_2 at the time of the formation of the Yuanjiaocun BIF, at the boundary between the Archean and Proterozoic zones, was enough to oxidize Fe^{2+} to Fe^{3+} , but not enough oxidize Ce^{3+} to Ce^{4+} (Bau and Dulski, 1996). The results of this study suggest that the formation of the Yuanjiaocun BIF is closely related to the GOE, which is consistent with the Paleoproterozoic atmospheric–marine environment proposed in previous studies.

4.6. Conclusion

Geochemical analysis of the ore and magnetite from the Yuanjiaocun BIF in the North China province provides information on the environment at the time of this deposit's formation. The growth of hematite, observed along the edge of magnetite, implies that the increase in fO_2 at the time of formation was enough to oxidize Fe^{2+} to Fe^{3+} . However, there is a vertical environmental change, from a deep–sea reductive environment to an oxidative environment due to the influence of the GOE during the formation of the Yuanjiaocun BIF, but this did not affect the oxidation of Ce^{3+} . From these results, it can be concluded that the GOE is closely related to the Yuanjiaocun BIF.

References

- Basta, F.F., Maurice, A.E., Fontboté, L., and Favarger, P.-Y., 2011, Petrology and geochemistry of the banded iron formation (BIF) of Wadi Karim and Um Anab, Eastern Desert, Egypt: implications for the origin of Neoproterozoic BIF. *Precambrian Research*, 187, 277-292.
- Bau, M., and Dulski, P., 1996, Distribution of yttrium and rare-earth elements in the Penge and Kuruman iron-formations, Transvaal Supergroup, South Africa. *Precambrian Research*, 79, 37-55.
- Beattie, I., and Gilson, T., 1970, The single-crystal Raman spectra of nearly opaque materials. Iron (III) oxide and chromium (III) oxide. *Journal of the Chemical Society A: Inorganic, Physical, Theoretical*, 980-986.
- Bekker, A., Slack, J.F., Planavsky, N., Krapež, B., Hofmann, A., Konhauser, K.O., and Rouxel, O.J., 2010, Iron formation: the sedimentary product of a complex interplay among mantle, tectonic, oceanic, and biospheric processes. *Economic Geology*, 105, 467-508.
- Bolhar, R., Van Kranendonk, M.J., and Kamber, B.S., 2005, A trace element study of siderite–jasper banded iron formation in the 3.45 Ga Warrawoona Group, Pilbara Craton—formation from hydrothermal fluids and shallow seawater. *Precambrian Research*, 137, 93-114.
- Drozdo, A.S., Ivanovski, V., Avnir, D., and Vinogradov, V.V., 2016, A universal magnetic ferrofluid: Nanomagnetite stable hydrosol with no added dispersants and at neutral pH. *Journal of colloid and interface science*, 468, 307-312.
- Geng, Y., Wan, Y., Shen, Q., Li, H., and Zhang, R., 2000, Chronological framework of the early Precambrian important events in the Luliang area, Shanxi Province. *ACTA GEOLOGICA SINICA-CHINESE EDITION*-, 74, 223-231 (in Chinese with English abstract).
- Gross, G.A., 1980, A classification of iron formations based on depositional environments. *The Canadian Mineralogist*, 18, 215-222.
- Han, C., Xiao, W., Su, B., Chen, Z., Zhang, X., Ao, S., Zhang, J., Zhang, Z., Wan, B., and Song, D., 2014, Neoproterozoic Algoma-type banded iron formations from Eastern Hebei, North China Craton: SHRIMP U-Pb age, origin and tectonic setting. *Precambrian Research*, 251, 212-231.

- Hou, K., Li, Y., Gao, J., Liu, F., and Qin, Y., 2014, Geochemistry and Si–O–Fe isotope constraints on the origin of banded iron formations of the Yuanjiacun Formation, Lvliang Group, Shanxi, China. *Ore Geology Reviews*, 57, 288-298.
- Hu, H., Niu, S., Wang, B., Sun, A., Xu, C., Li, Y., and Li, M., 2005, Source of fluids in the Longquanzhan gold deposits in the Yishui area, Shandong, China. *Mineral Deposit Research: Meeting the Global Challenge*. Springer, pp. 1539-1542.
- Huston, D.L., and Logan, G.A., 2004, Barite, BIFs and bugs: evidence for the evolution of the Earth's early hydrosphere. *Earth and Planetary Science Letters*, 220, 41-55.
- Isley, A.E., and Abbott, D.H., 1999, Plume-related mafic volcanism and the deposition of banded iron formation. *Journal of Geophysical Research: Solid Earth (1978–2012)*, 104, 15461-15477.
- Khalil, K.I., El-Shazly, A.E., and Lehmann, B., 2015, Late Neoproterozoic banded iron formation (BIF) in the central Eastern Desert of Egypt: Mineralogical and geochemical implications for the origin of the Gebel El Hadid iron ore deposit. *Ore Geology Reviews*, 69, 380-399.
- Klein, C., 2005, Some Precambrian banded iron-formations (BIFs) from around the world: Their age, geologic setting, mineralogy, metamorphism, geochemistry, and origins. *American Mineralogist*, 90, 1473-1499.
- Lan, T.-G., Fan, H.-R., Santosh, M., Hu, F.-F., Yang, K.-F., and Liu, Y., 2014, U–Pb zircon chronology, geochemistry and isotopes of the Changyi banded iron formation in the eastern Shandong Province: Constraints on BIF genesis and implications for Paleoproterozoic tectonic evolution of the North China Craton. *Ore Geology Reviews*, 56, 472-486.
- Lewis, I.R., and Edwards, H., 2001. *Handbook of Raman spectroscopy: from the research laboratory to the process line*. CRC Press.
- Li, H., Zhang, Z., Li, L., Zhang, Z., Chen, J., and Yao, T., 2014, Types and general characteristics of the BIF-related iron deposits in China. *Ore Geology Reviews*, 57, 264-287.
- Massey, M., Baier, U., Merlin, R., and Weber, W., 1990, Effects of pressure and

- isotopic substitution on the Raman spectrum of α -Fe₂O₃: identification of two-magnon scattering. *Physical Review B*, 41, 7822.
- McLennan, S., 1989, Rare earth elements in sedimentary rocks; influence of provenance and sedimentary processes. *Reviews in Mineralogy and Geochemistry*, 21, 169-200.
- Moon, I., Lee, I., and Yang, X., 2017, Geochemical constraints on the genesis of the Algoma-type banded iron formation (BIF) in Yishui County, western Shandong Province, North China Craton. *Ore Geology Reviews*, 89, 931-945.
- Murugappan, K., Silvester, D.S., Chaudhary, D., and Arrigan, D.W., 2014, Electrochemical Characterization of an Oleyl-coated Magnetite Nanoparticle-Modified Electrode. *ChemElectroChem*, 1, 1211-1218.
- Ohmoto, H., 2003, Nonredox transformations of magnetite-hematite in hydrothermal systems. *Economic Geology*, 98, 157-161.
- RRUFF Project website, an integrated database of Raman spectra, X-ray diffraction and chemistry data for minerals, <http://ruff.info/>.
- Shebanova, O.N., and Lazor, P., 2003, Raman spectroscopic study of magnetite (Fe₂O₄): a new assignment for the vibrational spectrum. *Journal of Solid State Chemistry*, 174, 424-430.
- Shim, S.-H., and Duffy, T.S., 2002, Raman spectroscopy of Fe₂O₃ to 62 GPa. *American Mineralogist*, 87, 318-326.
- Sun, X.-H., Zhu, X.-Q., Tang, H.-S., Zhang, Q., and Luo, T.-Y., 2014a, The Gongchangling BIFs from the Anshan–Benxi area, NE China: Petrological–geochemical characteristics and genesis of high-grade iron ores. *Ore Geology Reviews*, 60, 112-125.
- Sun, X.-H., Zhu, X.-Q., Tang, H.-S., Zhang, Q., Luo, T.-Y., and Han, T., 2014b, Protolith reconstruction and geochemical study on the wall rocks of Anshan BIFs, Northeast China: Implications for the provenance and tectonic setting. *Journal of Geochemical Exploration*, 136, 65-75.
- Trendall, A., 2009, The significance of iron-formation in the Precambrian stratigraphic record. *Precambrian sedimentary environments: A modern approach to depositional systems*, 33, 33-66.

- Wan, Y., Geng, Y., Shen, Q., and Zhang, R., 2000, Khondalite series-geochronology and geochemistry of the Jiehekou Group in Luliang area. *ACTA PETROLOGICA SINICA*, 16, 49-58 (in Chinese with English abstract).
- Wang, C., and Zhang, L., 2016. A Genetic Link Between Paleoproterozoic Yuanjiaocun BIF and the Great Oxidation Event in North China Craton. *Main Tectonic Events and Metallogeny of the North China Craton*. Springer, pp. 329-356.
- Wu, M., Zhao, G., Sun, M., Yin, C., Li, S., and Tam, P.Y., 2012, Petrology and P–T path of the Yishui mafic granulites: implications for tectonothermal evolution of the Western Shandong Complex in the Eastern Block of the North China Craton. *Precambrian Research*, 222, 312-324.
- Yang, X.-Q., Zhang, Z.-H., Duan, S.-G., and Zhao, X.-M., 2015, Petrological and geochemical features of the Jingtieshan banded iron formation (BIF): A unique type of BIF from the Northern Qilian Orogenic Belt, NW China. *Journal of Asian Earth Sciences*.
- Yu, J., Wang, D., Wang, C., and Li, H., 1997, Ages of the Luliang Group and its main metamorphism in the Luliang Mountains, Shanxi evidence from single-grain zircon U9Pb ages. *Geological Review*, 43, 403-408 (in Chinese with English abstract).
- Zhai, M., and Santosh, M., 2013, Metallogeny of the North China Craton: link with secular changes in the evolving Earth. *Gondwana Research*, 24, 275-297.
- Zhai, M., and Windley, B.F., 1990, The Archaean and early Proterozoic banded iron formations of North China: their characteristics, geotectonic relations, chemistry and implications for crustal growth. *Precambrian Research*, 48, 267-286.
- Zhai, M., Windley, B.F., and Sills, J.D., 1990, Archaean gneisses, amphibolites and banded iron-formations from the Anshan area of Liaoning Province, NE China: Their geochemistry, metamorphism and petrogenesis. *Precambrian Research*, 46, 195-216.
- Zhang, X., Zhang, L., Xiang, P., Wan, B., and Pirajno, F., 2011, Zircon U–Pb age, Hf isotopes and geochemistry of Shuichang Algoma-type banded iron-

- formation, North China Craton: constraints on the ore-forming age and tectonic setting. *Gondwana Research*, 20, 137-148.
- Zhao, G., Sun, M., Wilde, S.A., and Sanzhong, L., 2005, Late Archean to Paleoproterozoic evolution of the North China Craton: key issues revisited. *Precambrian Research*, 136, 177-202.
- Zhao, G., Wilde, S.A., Cawood, P.A., and Sun, M., 2001, Archean blocks and their boundaries in the North China Craton: lithological, geochemical, structural and P–T path constraints and tectonic evolution. *Precambrian Research*, 107, 45-73.
- Zhao, G., Wilde, S.A., Sun, M., Li, S., Li, X., and Zhang, J., 2008, SHRIMP U–Pb zircon ages of granitoid rocks in the Lüliang Complex: implications for the accretion and evolution of the Trans-North China Orogen. *Precambrian Research*, 160, 213-226.
- Zhao, G., and Zhai, M., 2013, Lithotectonic elements of Precambrian basement in the North China Craton: review and tectonic implications. *Gondwana Research*, 23, 1207-1240.
- Zheng, Y.-F., Xiao, W.-J., and Zhao, G., 2013, Introduction to tectonics of China. *Gondwana Research*, 23, 1189-1206.
- Zhu, M., Dai, Y., Zhang, L., Wang, C., and Liu, L., 2015, Geochronology and geochemistry of the Nanfen iron deposit in the Anshan-Benxi area, North China Craton: Implications for ~ 2.55 Ga crustal growth and the genesis of high-grade iron ores. *Precambrian Research*.

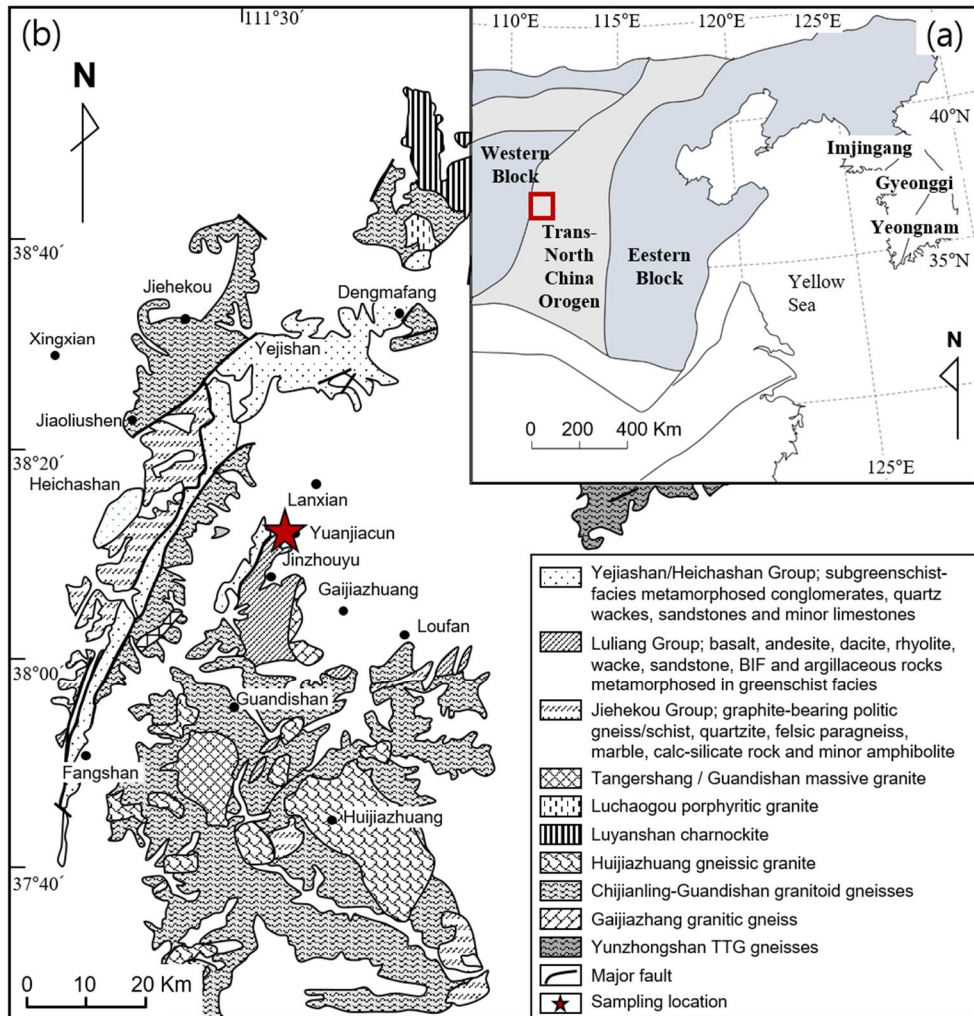


Figure 4.1. (a) Tectonic map of the North China Craton (NCC), revised from Zhao et al. (2005). Red square indicate location of Yuanjiacun BIF. The Archean to Proterozoic basement are widely distributed in the Eastern and Western Block of NCC. The Trans North China orogen is covered Paleoproterozoic basement. (b) Simplified geological map of the Luliang Complex, modified after Zhao et al. (2008).

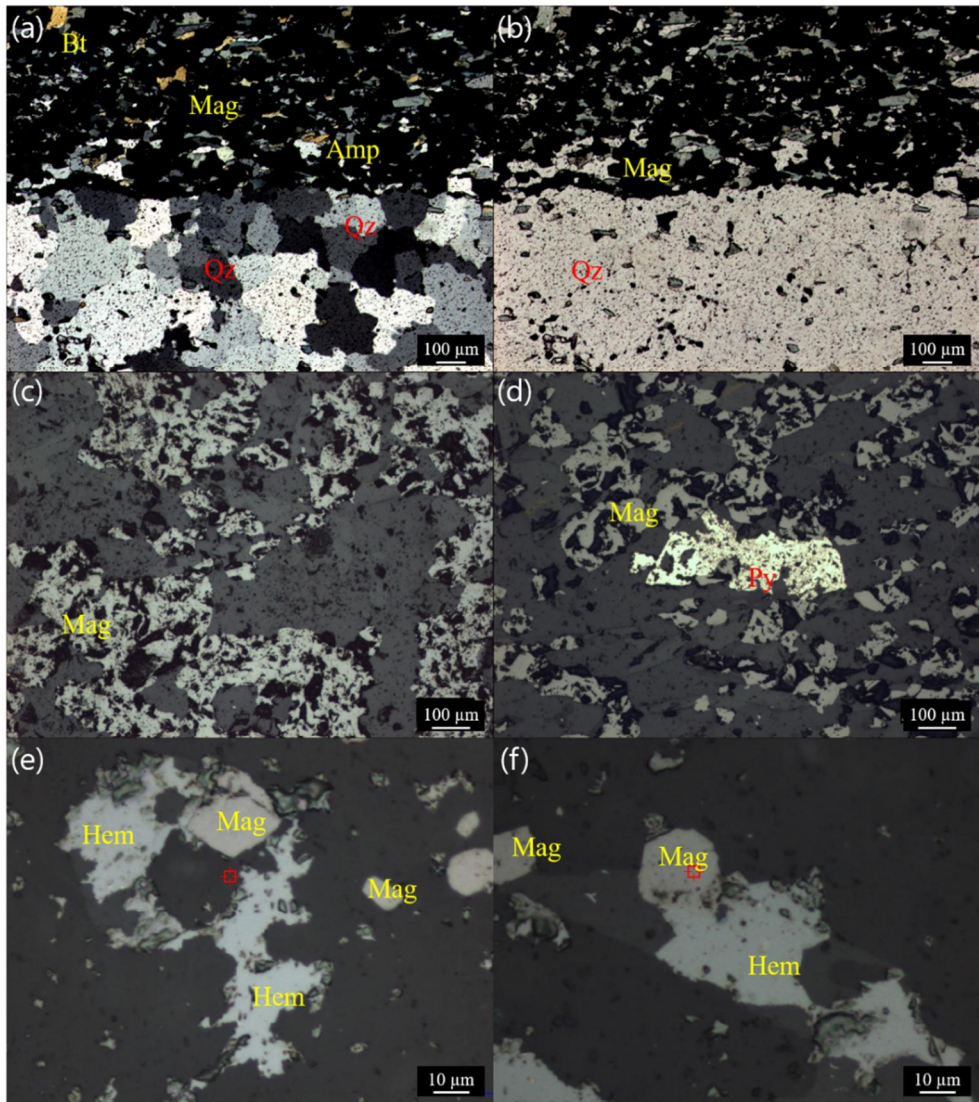


Figure 4.2. Yuanjiaacun BIF consisting of alternating Fe-rich layer and Si-rich layer (a) under cross polarized light and (b) open polarized light. (Magnetite; Mag, Hematite; Hem, Pyrite; Py, Quartz; Qz, Biotite; Bt, Amphibole; Amp). (c) Magnetite occurred as a representative ore mineral (reflected light) with (d) minor pyrite (reflected light). (e) Magnetite and hematite are identified in the thin section under reflecting microscope of Raman. (f) Magnetite and hematite were simultaneously shown in

magnetite.

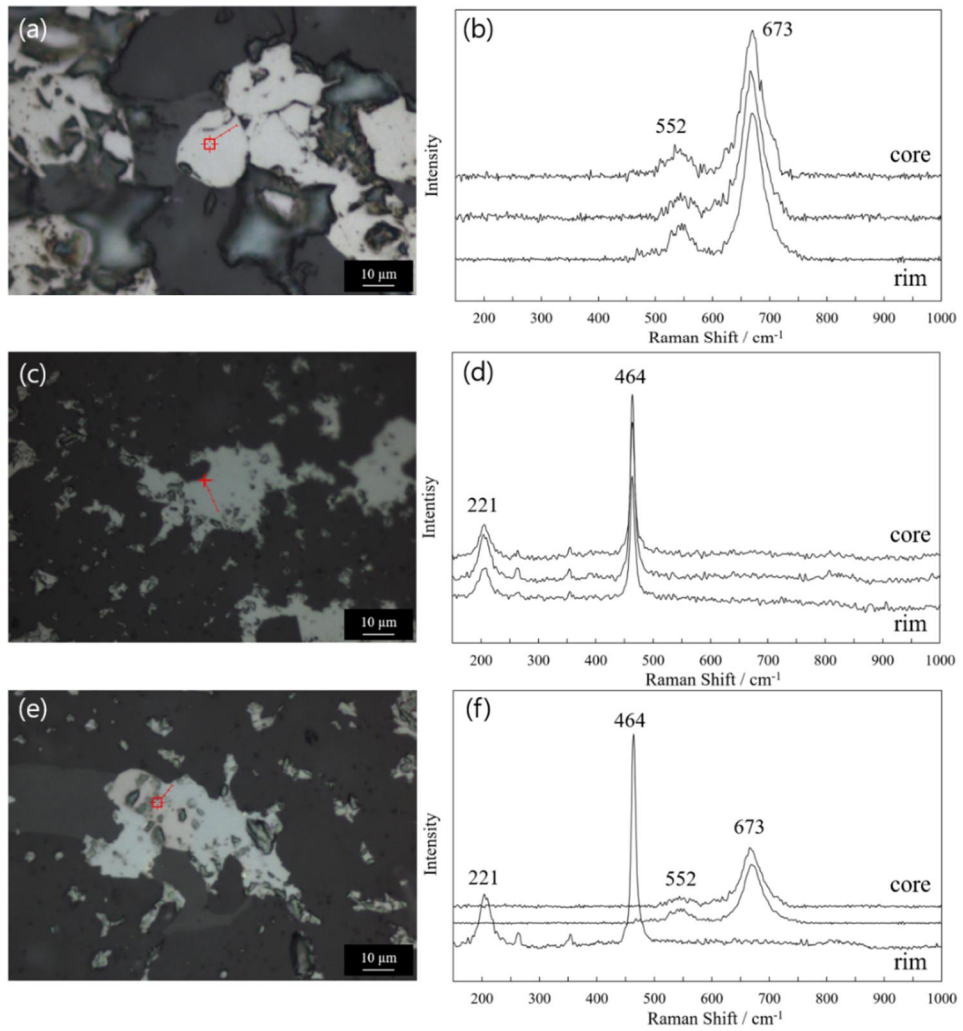
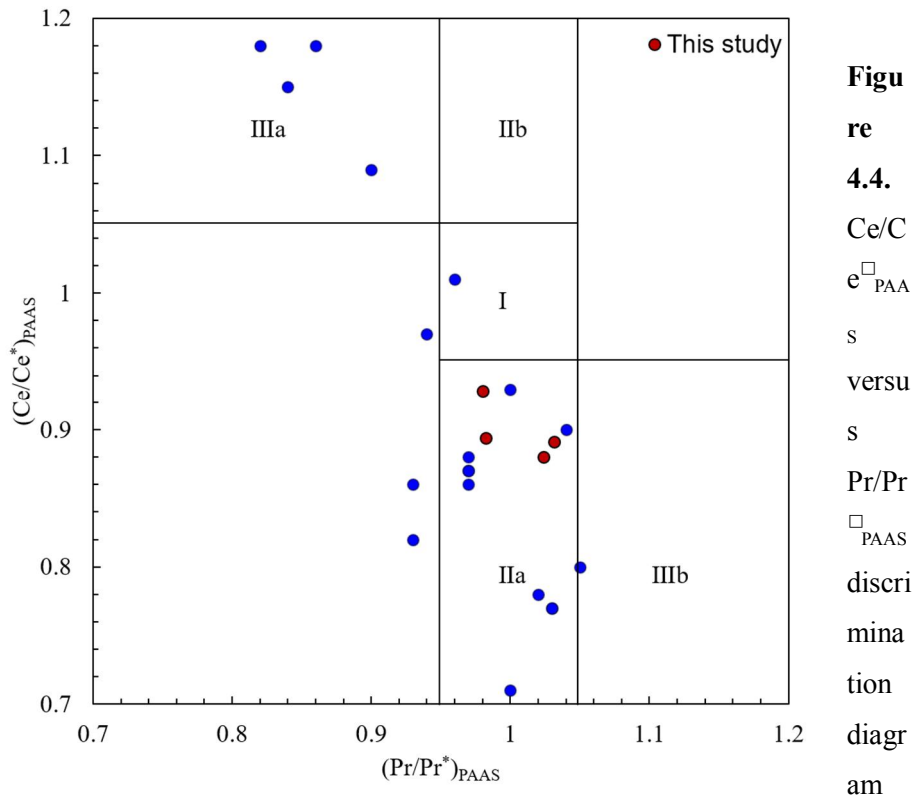


Figure 4.3. Raman analysis position (a, c, e) and Raman spectrum (b, d, f) of the magnetite and hematite from Yuanjiacun BIF.



for iron ores of Yuanjiacun BIF. Field I: neither Ce_{PAAS} nor La_{PAAS} anomaly; field II a: positive La_{PAAS} anomaly, no Ce_{PAAS} anomaly; field II b: negative La_{PAAS} anomaly, no Ce_{PAAS} anomaly; field IIIa: positive Ce_{PAAS} anomaly; field IIIb: negative Ce_{PAAS} anomaly. Red circles indicate iron ores from this study and blue circles comes from Hou et al. (2014) and Wang et al. (2014).

Table 4.1. EPMA data of the magnetite from Yuanjiacun BIF (wt.%)

	Na ₂ O	MgO	Al ₂ O ₃	SiO ₂	P ₂ O ₅	K ₂ O	CaO	TiO ₂	MnO	Fe ₂ O ₃	FeO	Total
1	0.00	0.01	0.07	0.17	0.02	0.00	0.03	0.02	0.06	69.60	31.31	101.27
2	0.01	0.00	0.07	0.07	0.02	0.01	0.02	0.04	0.01	69.52	31.27	101.03
3	0.00	0.00	0.06	0.09	0.00	0.00	0.01	0.03	0.00	70.22	31.59	102.00
4	0.02	0.00	0.09	0.12	0.00	0.01	0.01	0.04	0.01	69.60	31.31	101.20
5	0.00	0.01	0.06	0.11	0.01	0.00	0.01	0.04	0.02	70.07	31.52	101.85
6	0.00	0.00	0.07	0.08	0.00	0.00	0.02	0.04	0.00	69.43	31.23	100.87
7	0.01	0.00	0.08	0.05	0.01	0.00	0.01	0.05	0.04	69.32	31.18	100.75
8	0.00	0.00	0.08	0.10	0.05	0.00	0.01	0.06	0.01	69.82	31.41	101.53
9	0.02	0.00	0.03	0.07	0.02	0.00	0.03	0.01	0.00	70.25	31.60	102.03
10	0.00	0.02	0.03	0.07	0.02	0.01	0.03	0.00	0.00	68.76	30.93	99.87
11	0.00	0.06	0.11	0.27	0.03	0.05	0.02	0.02	0.01	69.39	31.22	101.17
12	0.01	0.02	0.05	0.20	0.00	0.00	0.03	0.00	0.00	69.18	31.12	100.61
13	0.00	0.43	0.26	1.48	0.01	0.15	0.12	0.00	0.05	68.17	30.67	101.34
14	0.00	0.01	0.02	0.09	0.00	0.00	0.02	0.00	0.03	69.36	31.20	100.74
15	0.00	0.01	0.03	0.05	0.00	0.00	0.01	0.01	0.04	69.28	31.17	100.60
16	0.00	0.00	0.02	0.08	0.00	0.00	0.00	0.00	0.01	69.06	31.07	100.25
17	0.01	0.00	0.04	0.05	0.00	0.00	0.01	0.00	0.00	69.51	31.27	100.88
18	0.02	0.02	0.04	0.19	0.00	0.02	0.02	0.01	0.01	69.89	31.44	101.64
19	0.01	0.01	0.01	0.05	0.00	0.00	0.02	0.01	0.04	69.23	31.14	100.52
20	0.00	0.00	0.04	0.07	0.00	0.00	0.02	0.01	0.00	70.08	31.52	101.73
21	0.00	0.00	0.05	0.09	0.00	0.01	0.02	0.00	0.03	68.70	30.90	99.81
22	0.00	0.00	0.03	0.10	0.00	0.00	0.02	0.00	0.00	69.52	31.28	100.95
23	0.01	0.00	0.08	0.12	0.00	0.08	0.03	0.01	0.00	68.64	30.88	99.85
24	0.00	0.01	0.04	0.08	0.00	0.00	0.01	0.00	0.02	69.95	31.47	101.59
25	0.00	0.03	0.04	0.12	0.00	0.01	0.00	0.00	0.04	69.69	31.35	101.27
26	0.00	0.00	0.03	0.05	0.00	0.01	0.01	0.00	0.00	69.31	31.18	100.58
27	0.00	0.00	0.03	0.10	0.00	0.00	0.01	0.01	0.03	68.85	30.97	99.99
Avg.	0.00	0.02	0.06	0.15	0.01	0.01	0.02	0.01	0.02	69.74	31.37	101.42

Avg: Average

Table 4.2 Pr/Pr* and Ce/Ce* data of the iron ores from Yuanjiacun BIF.

	Pr/Pr*	Ce/Ce*
1	0.98	0.89
2	0.98	0.93
3	1.02	0.88
4	1.03	0.89

Chapter 5. In-situ LA-ICP-MS trace element analyses of magnetite: New insight on the geochemical difference between Algoma- and Superior-type BIFs

Abstract

Magnetite is a representative ore mineral in banded iron formations (BIFs) and its composition can be used a petrogenetic and provenance indicator. Previous studies classified BIFs into Algoma- and Superior-types based on their tectonic setting, size and lithologic associations. In this study, we determined trace element contents of magnetite from one Algoma-type and two Superior-type BIFs in China by in-situ LA-ICP-MS analyses. Our results, together with a compilation of previously reported trace element data on magnetite from other regions, exhibit that there are systematic differences in trace element composition of magnetite between Algoma- and Superior-type BIFs due to differences in their depositional environments. The magnetite from the Algoma-type BIFs are more enriched in Al, Ti, Ni, and V than those from the Superior-type BIFs. The former precipitated dominantly from high temperature hydrothermal fluid under low oxygen fugacity conditions while the latter formed mainly from low temperature and relative oxidized sea water. In addition, the decreasing trend of Ni contents in magnetite from Algoma- to Superior-type BIFs is consistent with decreasing upper mantle

temperature from Archean to Proterozoic.

5.1. Introduction

Precambrian banded iron formation (BIF) is a window to understand changes in environmental conditions and role of photosynthetic bacteria during Archean and Proterozoic period (Isley and Abbott, 1999; Huston and Logan, 2004; Klein, 2005; Lascelles, 2007; Trendall, 2009; Bekker et al., 2010; Han et al., 2014; Lan et al., 2014a; Lan et al., 2014b; Ma et al., 2014; Sun et al., 2014). Gross and McLeod (1980) divided BIFs into Algoma- and Superior-type BIFs based on their depositional settings and lithological associations. The Algoma-type BIFs are associated with subaqueous volcanism and mainly formed in Eoarchean to Paleoproterozoic (Gross and McLeod, 1980; Barley et al., 1998; Bekker et al., 2010). In contrast, the Superior-type BIFs are most abundant in Paleoproterozoic period and intimately related to more stable tectonic conditions such as near-shore continental-shelf (Gross, 1980; Trendall, 2009). Huston and Logan (2004) proposed classification criteria for types of BIFs based on the intensity of Eu anomaly. They showed that Eu anomalies ($Eu/Eu^* = 2Eu/(Sm_N + Gd_N)$) of Algoma-type BIFs are > 1.8 whereas and those of Superior-type BIFs are < 1.8 . This discrepancy has been ascribed to differences in the involvement of submarine hydrothermal fluids in the formation of BIFs (Huston and Logan, 2004). The Algoma-type BIFs were more influenced by the volcanic related hydrothermal emanations than the Superior-type BIFs.

Magnetite is mechanically and chemically stable during erosion,

weathering, transportation and metamorphism (Grigsby, 1990; McClenaghan, 2005). A large number of cations (Mg, Al, Sc, Ti, V, Cr, Mn, Co, Ni, Zn, Ga, Ge, Y, Hf, Nb, Mo, Ta, and Zr) can be hosted by cubic spinel structure of magnetite (Nadoll et al., 2012; Liu et al., 2015). Magnetite geochemistry is controlled by physicochemical conditions during their crystallization which include fluid composition, temperature, pressure, oxygen, sulfur fugacity and fluid–host rock interaction (Nadoll et al., 2012; Huang et al., 2013; Liu et al., 2015). Therefore, magnetite geochemistry of the BIFs will enable us to constrain the physicochemical controlling factors and understand their depositional conditions (Razjigaeva and Naumova, 1992; Dupuis and Beaudoin, 2011; Nadoll et al., 2012; Nadoll et al., 2014).

In this study, we measured trace element contents of magnetite from the Algoma–type Yishui BIF and the Superior–type Huoqiu and Yuanjiacun BIFs from China using in–situ LA–ICP–MS technique. The results will be compared with previous LA–ICP–MS data on BIF magnetite from other areas in order to test if there are systematic differences in trace element compositions of magnetite between the two types of BIFs and to investigate factors controlling the compositions of magnetite.

5.2. Geological background

The North China Craton (NCC) is composed of the Archean to Paleoproterozoic Eastern Block and the Western Block with three Paleoproterozoic orogenic belts including the Trans–North China Orogen, the Khondalite Belt and the Jiao–Liao–Ji Belt (Zhao et al., 2001)(Figure 5.1a). It is surrounded by the

Central Asian Orogenic Belt, Qinling–Dabie Orogenic Belt and Su–Lu Orogenic Belt. Early Archean to Paleoproterozoic basement overlain by Mesoproterozoic to Cenozoic unmetamorphosed cover of the NCC (Zhao et al., 1998; Zhao et al., 2001; Zhao et al., 2005; Santosh, 2010; Zhai and Santosh, 2011). The Western Block was formed by the amalgamation of the Yinshan and Ordos Blocks along the Inner Mongolia Suture Zone (IMSZ) at ~1.95 Ga. The Eastern Block have undergone rifting at ~1.90 Ga and collision between the Longgang and the Langrim Blocks (Zhao et al., 2001). The NCC experienced two significant magmatic events at 2.8 – 2.7 Ga and 2.55 – 2.50 Ga which is closely related to crustal growth of the NCC (Yang et al., 2008; Li et al., 2010; Geng et al., 2012).

Most BIFs in the NCC formed during Archean with a peak growth in Neoproterozoic and belong to Algoma–type BIFs, while few has Paleoproterozoic Superior–type BIFs affinity (Zhai and Santosh, 2013; Lan et al., 2014a). The former are distributed in Hebei, Liaoning, Wutai and western Shandong Provinces and the latter are distributed in the Shanxi Province and eastern Shandong Province. The different distribution can be explained by tectonic events. The Archean NCC consist of at least seven micro–blocks (Zhai and Santosh, 2011). Their amalgamation was accompanied by intense magmatic activities and the events provided suitable environment for the precipitation of abundant Algoma–type BIFs. However, the confined Paleoproterozoic rifting provide non favorable environment of deposition of BIFs and resulted in lack of Superior–type BIFs in NCC (Lan et al., 2014a).

5.2.1. The Yishui BIF

The Yishui BIF is located in the Liuhang Formation of Taishan Group in Shandong Province. The main ore bodies are distributed in the Taishan Group, which is extended northwest–southeast direction of the western Shandong Province (WSP) and subdivided into the Shancaoyu, Yanlingguan, and Liuhang unit. The Archean sedimentary rocks are widespread in the study area (Figure 5.1c). All the units underwent upper greenschist to amphibolite facies metamorphism. The Taishan Group is mainly composed of metasedimentary rocks with minor BIF and volcanic rocks which formed in 2600–2540 Ma (Wan et al., 2012; Wang et al., 2013). The Liuhang Formation mainly consists of amphibolite, volcano–sedimentary rock and detrital material and subdivided into lower and upper parts based on lithology (Lai and Yang, 2012). Amphibolite occurs in the lower part, and biotite gneiss and metaconglomerate occur in the upper part. Magnetite and quartz are dominant minerals in the Yishui BIF with minor amphibole and rare pyrite and chalcopyrite. Recent geochemical study on the Yishui BIF (Moon et al., 2017) argued that it was formed by precipitation from a mixture of seawater and high–temperature hydrothermal fluids in submarine environment near a volcanic vent. Moon et al. (2017) considered the Yishui BIF as Algoma–type because of the marked positive Eu anomaly of the iron ore and its close spatial relationship with amphibolite as a wall rock.

5.2.2. The Huoqiu BIF

The Huoqiu BIF is a part of the northwest Huoqiu Group of the Eastern Block of the southeastern margin of the NCC (Figure 5.1b). The Huoqiu Group extends over 60 km from south to north with 1500 km² of total area and is

composed of the Huayuan Formation, the Wuji Formation and the Zhouji Formation based on lithology (Yang et al., 2014; Liu et al., 2015). Iron ores of the Huoqiu BIF are composed of quartz, magnetite and hematite (or specularite). The ore body is hosted by amphibole schist, plagioclase gneiss and amphibolite (Yang et al., 2014). Generally, Superior-type BIFs are thought to be formed in a stable shallow sea environment and closely related to sedimentary sequences (Klein, 2005). The Huoqiu BIF preserved rhythmic sequences comprised of biotite-leptynite and amphibole leptynite sandwiched between thin-layered mica-quartz schist-amphibolite or amphibole schist. These sedimentary sequences represent flysch deposition, which is rarely associated with Algoma-type BIFs (Yang et al., 2014). In addition, abundant carbonate minerals with insignificant relationship with volcanic activity are indicative of that the Huoqiu BIF belongs to Superior-type. Liu and Yang (2015) suggested that the Huoqiu BIF was formed in continental marginal sea or back arc basin environments based on geochemical studies of plagioclase amphibolite and gneiss.

5.2.3. The Yuanjiacun BIF

The Yuanjiacun BIF is located in the Shanxi Province and hosted by the Yuanjiacun Formation in the Lvliang Group (Figure 5.1d). The Yuanjiacun BIF is the largest open-pit iron deposit in Asia and have experienced greenschist facies metamorphism. The thickness of the Yuanjiacun BIF is approximately 1500 m. Magnetite and quartz occur as main minerals with minor hematite, siderite, specularite, limonite, pyrite, chlorite, dolomite, and calcite. The Yuanjiacun BIF is considered as Superior-type because it is laterally extensive and has close spatial

relationship with clastic sedimentary rocks (Wang et al., 2015). Hou et al. (2014) suggested that the Yuanjiaocun BIF was deposited at a shallow marine condition with limited influence from volcanic activity.

5.3. Analytical method

5.3.1. Whole-rock major and trace element analysis

We have measured major and trace element contents in six iron ores from the Huoqiu BIF and four iron ores from the Yuanjiaocun BIF. The samples were crushed and milled to fine powder in an agate mortar. The whole-rock analyses of iron ores from the Huoqiu and Yuanjiaocun BIF were conducted by activation laboratories Ltd. (Actlabs) in Ancaster, Ontario, Canada using package “4Litho” with fusion inductively coupled plasma emission (FUS-ICP) and inductively coupled plasma emission mass spectrometry (ICP-MS). The results are reported in Table 5.1 and 5.2. The whole-rock compositions of the Yishui BIF are taken from Moon et al. (2017).

5.3.2. Magnetite major and trace element analysis

Polished thin sections were prepared for representative parts of each sample. The in-situ major and trace element concentrations of magnetites from the Algoma-type Yishui BIF (n=45), and from the Superior-type Huoqiu BIF (n=22) and Yuanjiaocun BIF (n=22) were analysed by electron microprobe (EPMA) and laser ablation inductively coupled plasma mass spectrometry (LA-ICP-MS), respectively. A summary of magnetites geochemical data are given in Table 5.3.

In-situ major element analyses were carried out using SHIMADZU 1600 electron microprobe (EPMA) at Daedeok headquarters and Jeonju center of Korea Basic Science Institute (KBSI). The operating conditions are as follows: 15 kV of acceleration voltage, 20 nA of beam current, 1 μm of beam size and 0.5 μm of step size in elemental mapping.

In-situ trace element analyses of magnetite were performed at Ochang headquarters of Korea Basic Science Institute. The laser ablation system consists of Cetac Analyte (193 nm Excimer laser) and Thermo X2 series ICP-MS. The operating conditions were laser spot size of 50 μm or 65 μm with repetition rate of 5 Hz. Each analysis consists of 30s of background acquisition (gas blank) and 40s of data acquisition (sample ablation). The measured isotopes were ^{24}Mg , ^{27}Al , ^{29}Si , ^{31}P , ^{42}Ca , ^{45}Sc , ^{47}Ti , ^{51}V , ^{52}Cr , ^{55}Mn , ^{57}Fe , ^{59}Co , ^{60}Ni , ^{63}Cu , ^{66}Zn , ^{71}Ga , ^{74}Ge , ^{89}Y , ^{90}Zr , ^{93}Nb , ^{95}Mo , ^{118}Sn , ^{179}Hf , ^{181}Ta , ^{182}W and ^{208}Pb . The GSE-1G and BCR-2G were used as primary standards for calibrating trace element concentrations in magnetite. The FeO^{T} concentration obtained from EPMA was used as an internal standard to correct the yield differences between the standard and unknown samples. Data reduction was performed using the GLITTER software (www.glitter-gemoc.com).

5.4. Results

5.4.1. Algoma-type Yishui BIF

5.4.1.1. Petrography

The petrographic characteristics of iron ores from the Yishui BIF are summarized in Moon et al. (2017). They display massive structure (Figure 5.2a, b) or have continuous band structure of macro-bands of Fe- and Si- rich layers

(Figure 5.2c). The representative layering textures of alternating quartz, magnetite and Fe–silicate (amphibole) are observed under microscope (Figure 5.3a). Magnetite and quartz occur as major components with subordinate minor calcite, grunerite, actinolite, tremolite, spinel, hematite and pyrite (Figure 5.3b, c). Anhedral to euhedral magnetite range from 40 to 300 μm in size, and is commonly represent discrete and aggregate form.

5.4.1.2. Iron ore whole–rock composition

SiO_2 and $\text{Fe}_2\text{O}_3^{\text{T}}$ contents of the iron ore from the Yishui BIF range from 37.2 wt.% to 53.1 wt.% (avg. 44.9 wt.%) and from 40.4 wt.% to 55.4 wt.% (avg. 47.5 wt.%) respectively. The iron ores have MgO varying from 1.8 to 3.8 wt.% and CaO from 0.9 to 3.8 wt.%. Al_2O_3 , TiO_2 , Na_2O , K_2O , MnO and P_2O_5 contents are very low (< 1 wt.%). The oxide compositions of the Yishui BIF have higher $\text{Fe}_2\text{O}_3^{\text{T}}$ and lower SiO_2 , Al_2O_3 than typical Algoma–type BIFs (Gross and McLeod, 1980).

Post Archean Average Shale (PAAS) normalized patterns of the iron ores (Figure 5.4 and Table 5.2) are characterized by enrichment of HREE relative to LREE ($\text{La}/\text{Yb}_{\text{PAAS}}=0.17\text{--}0.29$). The iron ores represent weak positive La anomalies ($\text{La}/\text{La}^*_{\text{PAAS}}=1.05\text{--}1.19$), negative Ce anomalies ($\text{Ce}/\text{Ce}^*_{\text{PAAS}}=0.85\text{--}0.91$) with obvious positive Eu anomalies ($\text{Eu}/\text{Eu}^*_{\text{PAAS}}=2.44\text{--}4.19$) (Moon et al., 2017).

5.4.1.3. Magnetite composition

The magnetite from the Algoma–type Yishui BIF have homogeneous composition. They are depleted in Mn, V and Ni, but enriched in Ti and Cr than those of average Algoma–type BIFs in this study (Figure 5.5).

The spikes of Al, Si, Mg, and Mn in time-resolved spectra for LA-ICP-MS analyses were observed in some magnetite grains which we attributed to silicate mineral inclusions (Figure 5.6a) (Dupuis and Beaudoin, 2011; Zhao et al., 2016). The parts of spectra contaminated by inclusions were excluded for the LA-ICP-MS data reduction.

5.4.2. Superior-type Huoqiu BIF and Yuanjiacun BIF

5.4.2.1. Petrography

The iron ores from the Superior-type Huoqiu BIF (Figure 5.2d-f, 5.3d-f) and Yuanjiacun BIF (Figure 5.2g-i, 5.3g-i) have meso- to microscale alternating band texture indicating their sedimentary origin (Figure 5.2e-g). The microbanding consists of alternation of Fe-rich and Si-rich microbands (Figure 5.3d, g). Amphibole is widely distributed in the Fe-rich layers and sporadically occurred in the Si-rich layers (Figure 5.3e, g). Magnetite occurs as a main iron ore mineral with a trace amount of pyrite (Figure 5.3f, h, i). The subhedral to anhedral magnetite varies from 60 to 170 μm in grain size, which is smaller than those from the Yishui BIF. The dominant gangue mineral is quartz which has grain sizes of 100–500 μm .

5.4.2.2. Geochemistry of iron ore

The iron ores from the Yuanjiacun and Huoqiu BIF are mainly composed of SiO_2 and $\text{Fe}_2\text{O}_3^{\text{T}}$ (the average of $\text{SiO}_2+\text{Fe}_2\text{O}_3^{\text{T}}$ are 95.8 wt.% and 98.2 wt.%, respectively) which are consistent with major mineral components of quartz and magnetite with subordinate minor MgO, CaO, Al_2O_3 , MnO, Na_2O , K_2O , TiO_2 and P_2O_5 . They have higher SiO_2 , $\text{Fe}_2\text{O}_3^{\text{T}}$ and lower Al_2O_3 , CaO, Na_2O than typical

Superior-type BIFs (Gross and McLeod, 1980) (Table 5.1).

The total REE+Y concentrations of the iron ores from Yuanjiacun and Huoqiu BIF vary 12.8 – 13.5 ppm and 5.81 – 13.5 ppm, respectively. The PAAS-normalized REY patterns of Yuanjiacun and Huoqiu BIF are characterized by HREE enrichment, positive Eu and negative Ce anomalies (Figure 5.4 and Table 5.2).

5.4.2.3. Geochemistry of magnetite

The most abundant trace elements of magnetite from the two Superior-type BIFs are Mg, Al, Ti, V, Cr and Mn (Table 5.3). Cobalt, Ni, Zn, Ga and Mo contents are < 1ppm. The magnetite compositions of the two Superior-type BIFs are similar to the average magnetite compositions of the Superior-type BIFs with enriched in Ge, Mn and Ni and depleted in Sc and Ti (Figure 5.5). Inclusions are characterized by elevated by Al, Si, Mg and Mn concentration in magnetite occurred (Figure 5.6b, c). Also, Sn peak appeared in magnetite of Huoqiu BIF due to cassiterite inclusions (Zhao and Zhou, 2015).

5.5. Discussion

5.5.1. Algoma- and Superior-types BIFs

The Precambrian BIFs are classified into Algoma- and Superior- type according to their depositional settings, size, and lithological association, which controls their precipitation and deposition mechanism (Gross, 1980). The Algoma-type BIFs are generally hosted by volcanic rocks and closely related to volcanic activity (Gross, 1980). The restricted volcanogenic related deposit condition in

Archean provided appropriate physical–chemical condition for Algoma–type BIF precipitation (Dymek and Klein, 1988). They are precipitated explicitly from submarine hydrothermal fluid at the mid–ocean ridge, back–arc basin spreading center and island arc (Gross, 1980). They formed in restricted basin environments (Barrett et al., 1988) during Eoarchean to late Paleoproterozoic (Isley and Abbott, 1999; Huston and Logan, 2004). The Algoma–type BIFs are relatively thinner and smaller than the Superior–type BIFs (Gross, 1980). The Superior–type BIFs are often interbedded with carbonates, quartz arenite, and black shale without significant contribution from volcanic activity (Gross, 1980), which suggests they may have formed in shallow marine environments at continental margin settings. They commonly show granular and clastic texture and are more laterally extended relative to the Algoma–type BIFs (Gross, 1980; Klein, 2005; Bekker et al., 2010). Superior–type BIFs are known to have a close genetic link with Great Oxidation Event (GOE) (Bekker et al., 2010). The GOE is one of the most important geological redox–related events during the Earth’s history. The GOE began at around 2.45 Ga and the first timing of the rise of oxygen fugacity in Earth’s atmosphere (Bekker et al., 2004). The transformation from anoxic to oxic atmospheric conditions was reflected in the change of chemical and geological conditions (Zhai and Santosh, 2011). The event accompanied increase of oxygen and decrease of CH₄ in atmosphere (Konhauser et al., 2009) and formation of huge volume of BIFs (Zhai and Santosh, 2011).

Huston and Logan (2004) proposed systematic geochemical differences between the two types of BIFs based on the degree of Eu anomaly ($Eu/Eu^* = 2Eu_N / (Sm_N + Nd_N)$) in North American Shale Composite (NASC)–normalized REE patterns.

They suggested that the iron and silica of Algoma-type BIFs were dominantly supplied from the volcanic-related hydrothermal emanations than those of Superior-type BIFs. Furthermore, declining temperature of the hydrothermal fluid from Archean to Proterozoic due to decreasing temperature of the upper mantle was reflected in decreasing of the intensity of Eu anomaly of Algoma- to Superior-type BIFs (Bau and Möller, 1993). Hence, Eu anomalies of Algoma-type BIFs are > 1.8 and Superior-type BIFs are < 1.8 (Huston and Logan, 2004). The NASC-normalized Eu anomalies of the Algoma-type Yishui BIF varies from 2.4 to 4.1 with average values of 3.1. The Eu anomalies of Superior-type Huoqiu and Yuanjiacun BIFs are calculated with additional previously reported data from Yang et al. (2014), Hou et al. (2014) and Wang et al. (2014). The most iron ores have less than 1.8 of Eu anomalies. However, some of them exhibit up to 4.4 of Eu anomalies. The calculated values of Superior-type BIFs are smaller than those of Algoma-type BIFs generally. Especially, iron ores in Huoqiu BIF in this study have strong positive Eu anomaly, indicating Huoqiu BIF may have been influenced by high-temperature hydrothermal when it formed (Yang et al., 2014). In addition, Sang et al. (1981) investigated initial $^{87}\text{Sr}/^{86}\text{Sr}$ values from most Huoqiu BIF samples and stated that $^{87}\text{Sr}/^{86}\text{Sr}$ values of samples are between 0.704 and 0.707. The values are higher than those of mantle (0.703) and lower than those of normal continental crust (0.719), representing that they were formed by mixture of volcanic and sedimentary materials. According to the results, hydrothermal systems of Huoqiu BIF might be affected by volcanic activity locally. However, these geochemical data do not correspond to stratigraphic features of Huoqiu BIF. Huoqiu BIF preserved discernible rhythmic sequences, reflecting turbidite features.

Under lithological association of drill cores, from bottom to top, the Huoqiu BIF is characterized by flysch deposition. These stratigraphic features are rarely occurred in Algoma-type BIFs. These are reasons why Huoqiu BIF is included in Superior-type BIF nevertheless strong positive Eu anomaly (Yang et al., 2014).

The trace element compositions of magnetite are considered to reflect the ore-forming fluid compositions and genetic mechanism (Dare et al., 2014; Nadoll et al., 2014). They are considered to be controlled by ionic radius, charge balance, oxygen fugacity, temperature and coexisting minerals. In the following section, we will discuss the (1) dominant controlling factors that govern compositional variations in magnetite of BIFs, (2) to understand the influence of genetic conditions of BIFs on magnetite chemistry and (3) the systematic differences in trace element compositions of magnetite between the Algoma- and Superior-type BIFs. We compiled data from Wadi Karim and Um Anab BIF (Basta et al., 2011), Nuvvuagittuq BIF (Mloszewska et al., 2012), Randalls BIF (Steadman et al., 2014), Magin BIF (Duparc et al., 2016), Izok Lake and Austin Brook BIF (Makvandi et al., 2016) and Yishui BIF of Algoma-type BIFs and Sokoman BIF (Chung et al., 2015), Huoqiu BIF, Yuanjiacun BIF of Superior-type BIFs. Experiments on the each BIF had been conducted under different conditions. Hence, the data should be handled with caution.

Chung et al. (2015) used trace element data to compare primary and altered magnetites of the Superior-type Sokoman BIF and discuss the genetic link between depositional processes and magnetite composition. In general, the original sedimentary features of BIFs are rarely preserved in magnetite. However, some fine-grained magnetites in the Sokoman BIF have relict sedimentary textures and

are referred to as primary magnetite. The relatively low content and uniform distribution of trace elements in primary magnetites reflect their seawater origin. In addition, the trace element concentrations of Ti, Al, V, Mg, and Mn in altered magnetite show larger variations than those of primary magnetite with wide overlap. The wide variations are caused by post-sedimentation processes such as hydrothermal alteration. Enrichment is indicative of the addition of fluids from mafic-ultramafic rocks, implying the close genetic link between the origin of the iron formation and the volcanogenic hydrothermal system. The variable composition of altered magnetite therefore reflects the important role of hydrothermal fluids in the precipitation of the iron formation. Specifically, the deposition of Algoma-type BIFs is closer related to high-temperature hydrothermal alteration of the oceanic crust than that of Superior-type BIFs (Bekker et al., 2010). The various properties of hydrothermal fluids, generated by the volcanic system and based on the deposition site, lead to the modification of the composition of primary magnetite, resulting in different magnetite compositions (Chung et al., 2015). Therefore, the bulk continental crust-normalized trace element patterns of magnetites of average Algoma-type BIFs represent larger variations than that of Superior-type BIFs (Figure 5.5d). These results support that Algoma-type BIFs formed under diverse geologic conditions including hydrothermal alteration, and regional influences, whereas Superior-type BIFs formed in relatively stable geological settings.

5.5.2. Geochemical differences in magnetite from the Algoma- and Superior type BIFs

5.5.2.1. The global trend on the magnetite compositions

The partitioning behavior of trace elements in magnetite under specific conditions is governed by various factors including the temperature, fluid composition, oxygen and sulfur fugacities and fluid–rock interaction (Dare et al., 2014; Nadoll et al., 2014). The element enrichment of magnetite in hydrothermal deposits is influenced by single or multiple physicochemical factors (Nadoll et al., 2014).

As discussed above, hydrothermal fluids are genetically related to BIFs and play important roles in BIF precipitation. The magnetite in BIFs is termed to hydrothermal magnetite (Nadoll et al., 2014). Hydrothermal and magmatic magnetites can be distinguished using discrimination diagram of V vs. Ti (Knipping et al., 2015). In the diagram (Figure 5.7a), all magnetites from Algoma– and Superior–type BIFs plot inside or near the hydrothermal field and are indicative of their hydrothermal origin. The magnetites are subdivided into two groups based on the Ti and V compositions. The magnetites from Algoma–type BIFs have higher Ti and V contents than those of Superior–type BIFs due to the temperature and oxygen fugacity. Typically, the partitioning behavior and distribution of trace elements in magnetite mainly depend on the temperature and element solubility (McIntire, 1963; Frost, 1991). Algoma–type BIFs formed at >2.5 Ga and experienced high mantle heat flux (Bekker et al., 2010). In addition, Eu enrichment in Algoma–type BIFs indicates the contribution of high–temperature hydrothermal fluids to BIF formation (Klinkhammer et al., 1994; Huston and Logan, 2004). In contrast, the peak formation of Superior–type BIFs occurred at 2.5–2.3 Ga, reflecting atmospheric oxidation and Paleoproterozoic glaciation

(Bekker et al., 2010). The relative decrease in the magnitude of Eu anomalies of Superior-type BIFs suggests the contribution of relatively low-temperature hydrothermal fluids to BIF precipitation (Huston and Logan, 2004). Hence, Algoma-type BIFs formed under higher temperature conditions than Superior-type BIFs. Therefore, magnetites of Algoma-type BIFs are systematically enriched in Ti and V compared with those of Superior-type BIFs. Overall, the trace element concentration of magnetite decreases with decreasing temperature.

In addition, the Archean atmosphere and coeval hydrosphere had low oxygen levels (Huston and Logan, 2004). The V concentration in magnetite is strongly controlled by the oxygen fugacity during magnetite/melt partitioning (Toplis and Corgne, 2002). Hence, V is a redox-sensitive element and can be used as a representative indicator of redox conditions (Irving, 1978; Toplis and Corgne, 2002; Reguir et al., 2008). Multivalent states of V in natural fluid systems include V^{2+} , V^{3+} , V^{4+} , and V^{5+} , whereby V^{2+} occurs under extremely reduced conditions. V^{3+} , V^{4+} , and V^{5+} are commonly present in the Earth's system (Bordage et al., 2011). Among them, only V^{3+} can be preferentially enriched in the magnetite structure under low fO_2 conditions and V^{5+} is incompatible at high fO_2 conditions from fluids (Toplis and Corgne, 2002; Nadoll et al., 2014). As shown in Figure 5.7a, V in magnetites decrease from Algoma- to Superior-type BIFs, which is consistent with the fO_2 increase from Archean to Paleoproterozoic. This trend therefore reflects the change of the oxygen conditions from Archean to Paleoproterozoic.

The discrimination diagram of Ti+V vs. Al+Mn (Dupuis and Beaudoin, 2011) is used for the identification of types of hydrothermal deposits based on the magnetite composition. Figure 5.7b shows that most of the BIF magnetites plot

outside the BIF field and widely vary due to complex genesis mechanisms. The most interesting points are the compositional characteristics of magnetite in the diagram which also can be systematically divided into two groups according to the BIF type. This can also be explained by the temperature dependency of the magnetite composition.

Figure 5.7c shows the variations in the magnetite compositions according to the Ni and V contents. The Ni flux in the ocean dramatically declines with time during Earth's history (Konhauser et al., 2009). Methanogens, methane-producing bacteria, depend on nickel as a metal critical for their essential enzymes (Jaun and Thauer, 2007; Bekker et al., 2010). Hence, the decrease of the Ni concentration restrained the activity of methane producers and supply of biogenic methane in the ancient ocean. The methanogens controlled the oxygen level in the Precambrian atmosphere. Therefore, Ni can be used as an indicator for changing atmospheric conditions over geologic time (Konhauser et al., 2009). Konhauser et al. (2009) suggested two stages, that is stage 1 (~3.8–2.7 Ga) and stage 2 (around 2.5 Ga), based on the maximal molar Ni/Fe ratios in magnetites and hematites from BIFs. The molar Ni/Fe ratios of both stages widely vary. The maximal ratios are almost consistent and relatively high in stage 1 and dramatically decreased at boundary between stage 1 and stage 2. At that time, the Ni reduction in the oceans due to Paleoproterozoic glaciation (Huronian glaciation) led to the cooling of the upper mantle and decreasing production of Ni-rich ultramafic rocks. Accordingly, the magnetite chemistry reflects the change of the Ni flux in the ocean from Archean to Paleoproterozoic. However, there is a wide overlap between Algoma- and Superior-type BIFs and no systematic variations can be observed in magnetites

from the Yishui, Huoqiu, and Yuanjiacun BIFs, although the division of Algoma- and Superior-type BIFs is based on the Ni contents of magnetites. This is because most of the studied BIFs are older than 2.5 Ga, included in stage 1, except Yuanjiacun (2.3 Ga) and Sokoman BIFs (1.8 Ga). From this perspective, the lack of a compositional trend of Ni in magnetite and wide overlap can be accounted for by the large Ni variation in stage 1. Figure 5.7c shows no clear systematic differences of V between Algoma- and Superior-type BIFs, which is due to the lack of data.

Globally, there are systematic differences in the magnetite compositions from Algoma- and Superior-type BIFs. The discrepancy between the two types of BIFs helps to understand the geological and environmental evolution of the early Earth from Archean to Paleoproterozoic. In addition, we confirmed that the systematic differences of the magnetite composition from Algoma- and Superior-type BIFs are consistent with characteristics of BIFs from previous studies.

5.5.2.2. Regional trend on the magnetite compositions

The partitioning behavior of trace elements in magnetites from the Yishui, Huoqiu and Yuanjiacun BIFs with average and the compositional ranges of magnetites from Algoma- and Superior-type BIFs are summarized in bulk continental normalized multi-element spectra (Figure 5.5). The magnetites from the Yishui BIF are homogeneous and show Ge, Ga, Ti, V and Cr spikes and Sc, Mn and Ni depletion. Compared with the average magnetite from Algoma-type BIFs, they are depleted in Mn, V and Ni and enriched in Ti (Figure 5.5a). These differences in the elemental distribution between magnetites from the Yishui BIF and average Algoma-type BIFs indicate the regional influence on the Yishui BIF

formation. We exclude the possibility of secondary alteration because of the homogeneous distribution of the trace elements in magnetite of the Yishui BIF. The magnetites from the Huoqiu and Yuanjiacun BIFs exhibit similar trends to those of average magnetite from Superior-type BIFs, which are characterized by Ge and Mn enrichment and Sc, Ga, and Ti depletion (Figure 5.5b, c). The similar systematic trends show that Huoqiu and Yuanjiacun BIFs have common features with other Superior-type BIFs. However, magnetites from the Huoqiu and Yuanjiacun BIFs display wide ranges in Ga, Ti, V, and Cr (Figure 5.5b,c), which indicates that the BIFs experienced post-sedimentation processes, such as hydrothermal alteration, as suggested by Chung et al. (2015).

As explained above, the regional influence on the formation of BIFs is considerably high and the discrepancy between global and regional trends is particularly important in understanding the effect of regional geological conditions on the magnetite composition. This perspective is discussed in detail in the following paragraphs.

Despite the discerning compositional variations in magnetite from Algoma- and Superior-type BIFs, the magnetites from the Yishui, Huoqiu, and Yuanjiacun BIFs have similar Al + Mn and Ni contents, as shown in Figure 5.7b and c. This can be partially attributed to the regional influence on the Yishui, Huoqiu, and Yuanjiacun BIFs. Magnetites from the Yishui, Huoqiu, and Yuanjiacun BIFs have similar Al concentrations but different Mn contents. Magnetites from the Yishui BIF have lower Mn concentrations than other Algoma-type BIFs (Figure 5.5a). Manganese is easily incorporated into magnetite under hydrothermal conditions. Hence, it can be used as proxy for the composition of the hydrothermal

fluids if secondary alteration has not occurred (Nadoll et al., 2014). Therefore, the low Mn content in magnetites from the Yishui BIF are probably due to the Mn deficiency of the original hydrothermal fluids.

As explained in Section 5.5.2.1., Ni is generally supplied from abundant Ni-rich tholeiite and komatiite and olivine-rich basalt in the hotter Precambrian mantle (Konhauser et al., 2009). In other words, Ni-rich ultra (mafic) volcanic rocks on the seafloor provide enough Ni to be dissolved in seawater (Barley, 1986). Steadman et al. (2014) suggested that the low Ni content of magnetite is due to the lack of exposure of these lithologies in the proximal depositional site of the Randalls BIF. From this point of view, the komatiite–tholeiite sequence is the major supracrustal assemblage in the WSP (Wang et al., 2013). However, Ni-rich tholeiite, komatiite, and olivine-rich basalt have not been reported at the depositional site of the Yushui BIF (Wu et al., 2012; Li et al., 2016; Santosh et al., 2016).

Figure 5.8 shows the average Ga, Al, V, Ni, and Ti contents with maximum and minimum in magnetites from each BIF and average values of Algoma– and Superior–type BIFs. The Ga and Al concentrations are temperature-dependent (Nadoll et al., 2014). Interestingly, Ga in magnetites shows the most ideal trend between Algoma– and Superior–type BIFs (Figure 5.8a). The Al trend in the magnetites is almost the same (Figure 5.8b).

The compositional trends of magnetite from the Nuvvuagittuq and Magin BIFs show marked depletion of Ti and V compared with those of magnetites from Algoma– and Superior–type BIFs (Figures 5.8d and e). One possible controlling factor (first-order factor) is the fluid composition dependency of hydrothermal

magnetite (Nadoll et al., 2014). Titanium is considered to be relatively immobile in hydrothermal magnetite during hydrothermal alteration (Van Baalen, 1993) and the concentrations are commonly low in hydrothermal fluids (Dare et al., 2014). Because Ti is compatible with magnetite, the magnetite composition reflects the Ti depletion of the fluid (Dare et al., 2014). The V concentration of iron ores ranges from 2.19 to 9.26 ppm with an average of 4.28 ppm, and the median content of magnetites is 6.5 ppm in Nuvvuagittuq BIF (Mloszewska et al., 2012). Vanadium in magnetites and iron ores in Huoqui BIF are less than 5 and 8 ppm and the those concentration in Yuanjiacun BIFs are less than 5 ppm and 11 ppm, respectively. The similar concentrations indicate that the V concentration of iron ore is mainly controlled by magnetite. Therefore, V in magnetite can reflect the source of the iron ore such as the composition of the hydrothermal fluid. As a result, hydrothermal fluid with low Ti and V concentrations may have existed at the proximal depositional sites of the Nuvvuagittuq and Magin BIFs. The other possible controlling factor is the effect of hydrothermal alteration on the BIFs. Hydrothermally altered magnetite exhibits highly variable trace element contents compared with unaltered magnetite (Chung et al., 2015). Magnetite from the Nuvvuagittuq BIF displays lower V contents than the magnetites of other Algoma-type BIFs with a wide range concentrations (Mloszewska et al., 2012). Hence, the altered magnetite from the Nuvvuagittuq BIF might have comparatively low V contents. Although the data of this study cannot clearly explain the Ti and V depletion in magnetite of the Nanfen and Magin BIFs, multiple factors might control the Ti and V composition in magnetite of the BIFs.

Based on the result of this trend, the composition of magnetite can be

incidentally controlled by regional influence.

5.6. Concluding remarks

Based on the in-situ LA-ICP-MS analyses of magnetite, the results are as follows:

- 1) The geochemical properties of magnetite are well-preserved in its grains. Single or multiple physicochemical factors govern controlling the abundance of trace elements in magnetites.
- 2) Globally, magnetites from Algoma- and Superior-type BIFs have systematic differences in trace element abundances, despite considerable overlap. In this regard, the variations of specific elements reflect changes of temperature, oxygen fugacity and mantle activity from Archean to Paleoproterozoic. Magnetites from the Algoma-type BIFs are more enriched in trace elements than those from the Superior-type because the former originated dominantly from high-temperature hydrothermal fluid under low oxygen fugacity conditions with volcanic activity while the latter formed mainly from low temperature and relatively oxidized sea water. The results are well consistent with previous studies.
- 3) Regional influences also have played important role on the formation of BIFs. It was confirmed that magnetite compositions were modified according to the regional influences.

References

- Barley, M., 1986, Incompatible–element enrichment in Archean basalts: a consequence of contamination by older sialic crust rather than mantle heterogeneity. *Geology*, 14, 947–950.
- Barley, M.E., Krapez, B., Groves, D.I., and Kerrich, R., 1998, The Late Archean bonanza: metallogenic and environmental consequences of the interaction between mantle plumes, lithospheric tectonics and global cyclicality. *Precambrian Research*, 91, 65–90.
- Barrett, T., Fralick, P., and Jarvis, I., 1988, Rare–earth–element geochemistry of some Archean iron formations north of Lake Superior, Ontario. *Canadian Journal of Earth Sciences*, 25, 570–580.
- Basta, F.F., Maurice, A.E., Fontboté, L., and Favarger, P.–Y., 2011, Petrology and geochemistry of the banded iron formation (BIF) of Wadi Karim and Um Anab, Eastern Desert, Egypt: implications for the origin of Neoproterozoic BIF. *Precambrian Research*, 187, 277–292.
- Bau, M., and Möller, P., 1993, Rare earth element systematics of the chemically

- precipitated component in Early Precambrian iron formations and the evolution of the terrestrial atmosphere–hydrosphere–lithosphere system. *Geochimica et Cosmochimica Acta*, 57, 2239–2249.
- Bekker, A., Holland, H., Wang, P.-L., Rumble Iii, D., Stein, H., Hannah, J., Coetzee, L., and Beukes, N., 2004, Dating the rise of atmospheric oxygen. *Nature*, 427, 117.
- Bekker, A., Slack, J.F., Planavsky, N., Krapež, B., Hofmann, A., Konhauser, K.O., and Rouxel, O.J., 2010, Iron formation: the sedimentary product of a complex interplay among mantle, tectonic, oceanic, and biospheric processes. *Economic Geology*, 105, 467–508.
- Bolhar, R., Kamber, B.S., Moorbath, S., Fedo, C.M., and Whitehouse, M.J., 2004, Characterisation of early Archaean chemical sediments by trace element signatures. *Earth and Planetary Science Letters*, 222, 43–60.
- Bordage, A., Balan, E., de Villiers, J.P., Cromarty, R., Juhin, A., Carvallo, C., Calas, G., Raju, P.S., and Glatzel, P., 2011, V oxidation state in Fe–Ti oxides by high–energy resolution fluorescence–detected X–ray absorption spectroscopy. *Physics and Chemistry of Minerals*, 38, 449–458.
- Cao, G., Wang, Z., Cheng, Z., Dong, Y., Li, P., Wang, S., Jin, L., Shen, K., Xu, J., and Shen, K., 1996, Early Precambrian geology of western Shandong. Geol. Publ. House, Beijing, 1–210.
- Chung, D., Zhou, M.-F., Gao, J.-F., and Chen, W.T., 2015, In-situ LA-ICP-MS trace elemental analyses of magnetite: The late Palaeoproterozoic Sokoman Iron Formation in the Labrador Trough, Canada. *Ore Geology Reviews*, 65, 917–928.
- Condie, K.C., 1993, Chemical composition and evolution of the upper continental crust: contrasting results from surface samples and shales. *Chemical Geology*, 104, 1–37.
- Dare, S.A., Barnes, S.-J., and Beaudoin, G., 2012, Variation in trace element content of magnetite crystallized from a fractionating sulfide liquid, Sudbury, Canada: implications for provenance discrimination. *Geochimica et Cosmochimica Acta*, 88, 27–50.
- Dare, S.A., Barnes, S.-J., Beaudoin, G., Méric, J., Boutroy, E., and Potvin-Doucet,

- C., 2014, Trace elements in magnetite as petrogenetic indicators. *Mineralium Deposita*, 49, 785–796.
- Duparc, Q., Dare, S.A., Cousineau, P.A., and Goutier, J., 2016, Magnetite Chemistry As A Provenance Indicator In Archean Metamorphosed Sedimentary Rocks. *Journal of Sedimentary Research*, 86, 542–563.
- Dupuis, C., and Beaudoin, G., 2011, Discriminant diagrams for iron oxide trace element fingerprinting of mineral deposit types. *Mineralium Deposita*, 46, 319–335.
- Dymek, R.F., and Klein, C., 1988, Chemistry, petrology and origin of banded iron-formation lithologies from the 3800 Ma Isua supracrustal belt, West Greenland. *Precambrian Research*, 39, 247–302.
- Frost, B.R., 1991, Stability of oxide minerals in metamorphic rocks. *Reviews in Mineralogy and Geochemistry*, 25, 469–488.
- Geng, Y., Du, L., and Ren, L., 2012, Growth and reworking of the early Precambrian continental crust in the North China Craton: constraints from zircon Hf isotopes. *Gondwana Research*, 21, 517–529.
- Grigsby, J.D., 1990, Detrital magnetite as a provenance indicator. *Journal of Sedimentary Research*, 60.
- Gross, G., and McLeod, C., 1980, A preliminary assessment of the chemical composition of iron formations in Canada. *The Canadian Mineralogist*, 18, 223–229.
- Gross, G.A., 1980, A classification of iron formations based on depositional environments. *The Canadian Mineralogist*, 18, 215–222.
- Han, C., Xiao, W., Su, B., Chen, Z., Zhang, X., Ao, S., Zhang, J., Zhang, Z., Wan, B., and Song, D., 2014, Neoproterozoic Algoma-type banded iron formations from Eastern Hebei, North China Craton: SHRIMP U–Pb age, origin and tectonic setting. *Precambrian Research*, 251, 212–231.
- Hou, K., Li, Y., Gao, J., Liu, F., and Qin, Y., 2014, Geochemistry and Si–O–Fe isotope constraints on the origin of banded iron formations of the Yuanjiacun Formation, Lvliang Group, Shanxi, China. *Ore Geology Reviews*, 57, 288–298.
- Huang, X.-W., Zhou, M.-F., Qi, L., Gao, J.-F., and Wang, Y.-W., 2013, Re–Os

- isotopic ages of pyrite and chemical composition of magnetite from the Cihai magmatic–hydrothermal Fe deposit, NW China. *Mineralium Deposita*, 48, 925–946.
- Huston, D.L., and Logan, G.A., 2004, Barite, BIFs and bugs: evidence for the evolution of the Earth's early hydrosphere. *Earth and Planetary Science Letters*, 220, 41–55.
- Irving, A.J., 1978, A review of experimental studies of crystal/liquid trace element partitioning. *Geochimica et Cosmochimica Acta*, 42, 743–770.
- Isley, A.E., and Abbott, D.H., 1999, Plume-related mafic volcanism and the deposition of banded iron formation. *Journal of Geophysical Research: Solid Earth (1978–2012)*, 104, 15461–15477.
- Jaun, B., and Thauer, R., 2007. of Book: Nickel and its Surprising Impact in Nature, Vol. 2 of Metal Ions in Life Sciences. John Wiley & Sons, Ltd.
- Klein, C., 2005, Some Precambrian banded iron-formations (BIFs) from around the world: Their age, geologic setting, mineralogy, metamorphism, geochemistry, and origins. *American Mineralogist*, 90, 1473–1499.
- Klinkhammer, G., Elderfield, H., Edmond, J., and Mitra, A., 1994, Geochemical implications of rare earth element patterns in hydrothermal fluids from mid-ocean ridges. *Geochimica et Cosmochimica Acta*, 58, 5105–5113.
- Knipping, J.L., Bilinker, L.D., Simon, A.C., Reich, M., Barra, F., Deditius, A.P., Wälle, M., Heinrich, C.A., Holtz, F., and Munizaga, R., 2015, Trace elements in magnetite from massive iron oxide–apatite deposits indicate a combined formation by igneous and magmatic–hydrothermal processes. *Geochimica et Cosmochimica Acta*, 171, 15–38.
- Konhauser, K.O., Pecoits, E., Lalonde, S.V., Papineau, D., Nisbet, E.G., Barley, M.E., Arndt, N.T., Zahnle, K., and Kamber, B.S., 2009, Oceanic nickel depletion and a methanogen famine before the Great Oxidation Event. *Nature*, 458, 750–753.
- Lai, X.D., and Yang, X., 2012, Characteristics of the banded iron formation (BIF) and its zircon chronology in Yangzhuang, western Shandong. *ACTA PETROLOGICA SINICA*, 28, 3612–3622.
- Lan, T.-G., Fan, H.-R., Hu, F.-F., Yang, K.-F., Cai, Y.-C., and Liu, Y.-S., 2014a,

- Depositional environment and tectonic implications of the Paleoproterozoic BIF in Changyi area, eastern North China Craton: Evidence from geochronology and geochemistry of the metamorphic wallrocks. *Ore Geology Reviews*, 61, 52–72.
- Lan, T.–G., Fan, H.–R., Santosh, M., Hu, F.–F., Yang, K.–F., and Liu, Y., 2014b, U–Pb zircon chronology, geochemistry and isotopes of the Changyi banded iron formation in the eastern Shandong Province: Constraints on BIF genesis and implications for Paleoproterozoic tectonic evolution of the North China Craton. *Ore Geology Reviews*, 56, 472–486.
- Lascelles, D.F., 2007, Black smokers and density currents: a uniformitarian model for the genesis of banded iron–formations. *Ore Geology Reviews*, 32, 381–411.
- Li, S.–S., Santosh, M., Cen, K., Teng, X.–M., and He, X.–F., 2016, Neoproterozoic convergent margin tectonics associated with microblock amalgamation in the North China Craton: evidence from the Yishui Complex. *Gondwana Research*, 38, 113–131.
- Li, T., Zhai, M., Peng, P., Chen, L., and Guo, J., 2010, Ca. 2.5 billion year old coeval ultramafic–mafic and syenitic dykes in Eastern Hebei: Implications for cratonization of the North China Craton. *Precambrian Research*, 180, 143–155.
- Liu, P.–P., Zhou, M.–F., Chen, W.T., Gao, J.–F., and Huang, X.–W., 2015, In-situ LA–ICP–MS trace elemental analyses of magnetite: Fe–Ti–(V) oxide-bearing mafic–ultramafic layered intrusions of the Emeishan Large Igneous Province, SW China. *Ore Geology Reviews*, 65, 853–871.
- Ma, X., Fan, H.–R., Santosh, M., and Guo, J., 2014, Chronology and geochemistry of Neoproterozoic BIF–type iron deposits in the Yinshan Block, North China Craton: Implications for oceanic ridge subduction. *Ore Geology Reviews*, 63, 405–417.
- Makvandi, S., Ghasemzadeh–Barvarz, M., Beaudoin, G., Grunsky, E.C., McClenaghan, M.B., Duchesne, C., and Boutroy, E., 2016, Partial least squares–discriminant analysis of trace element compositions of magnetite from various VMS deposit subtypes: Application to mineral exploration.

- Ore Geology Reviews, 78, 388–408.
- McClenaghan, M.B., 2005, Indicator mineral methods in mineral exploration. *Geochemistry: Exploration, Environment, Analysis*, 5, 233–245.
- McIntire, W., 1963, Trace element partition coefficients—a review of theory and applications to geology. *Geochimica et Cosmochimica Acta*, 27, 1209–1264.
- McLennan, S., 1989, Rare earth elements in sedimentary rocks; influence of provenance and sedimentary processes. *Reviews in Mineralogy and Geochemistry*, 21, 169–200.
- Mloszewska, A.M., Pecoits, E., Cates, N.L., Mojzsis, S.J., O'Neil, J., Robbins, L.J., and Konhauser, K.O., 2012, The composition of Earth's oldest iron formations: the Nuvvuagittuq Supracrustal Belt (Québec, Canada). *Earth and Planetary Science Letters*, 317, 331–342.
- Moon, I., Lee, I., and Yang, X., 2017, Geochemical constraints on the genesis of the Algoma-type banded iron formation (BIF) in Yishui County, Western Shandong Province, North China Craton. *Ore Geology Reviews*.
- Nadoll, P., Angerer, T., Mauk, J.L., French, D., and Walshe, J., 2014, The chemistry of hydrothermal magnetite: a review. *Ore Geology Reviews*, 61, 1–32.
- Nadoll, P., Mauk, J.L., Hayes, T.S., Koenig, A.E., and Box, S.E., 2012, Geochemistry of magnetite from hydrothermal ore deposits and host rocks of the Mesoproterozoic Belt Supergroup, United States. *Economic Geology*, 107, 1275–1292.
- Razjigaeva, N., and Naumova, V., 1992, Trace element composition of detrital magnetite from coastal sediments of northwestern Japan Sea for provenance study. *Journal of Sedimentary Research*, 62, 802–809.
- Reguir, E.P., Chakhmouradian, A.R., Halden, N.M., Yang, P., and Zaitsev, A.N., 2008, Early magmatic and reaction-induced trends in magnetite from the carbonatites of Kerimasi, Tanzania. *The Canadian Mineralogist*, 46, 879–900.
- Rudnick, R., and Gao, S., 2003, Composition of the continental crust. *Treatise on geochemistry*, 3, 659.
- Sang, B.L., Xing, F.M., and Chen, Y.Z., 1981, The Precambrian metamorphic iron

- ore characteristics and prospecting. *Anhui Inst Geol Sci*, 1, 10–20.
- Santosh, M., 2010, Assembling North China Craton within the Columbia supercontinent: the role of double-sided subduction. *Precambrian Research*, 178, 149–167.
- Santosh, M., Teng, X.-M., He, X.-F., Tang, L., and Yang, Q.-Y., 2016, Discovery of Neoproterozoic suprasubduction zone ophiolite suite from Yishui Complex in the North China Craton. *Gondwana Research*, 38, 1–27.
- Steadman, J.A., Large, R.R., Davidson, G.J., Bull, S.W., Thompson, J., Ireland, T.R., and Holden, P., 2014, Paragenesis and composition of ore minerals in the Randalls BIF-hosted gold deposits, Yilgarn craton, Western Australia: Implications for the timing of deposit formation and constraints on gold sources. *Precambrian Research*, 243, 110–132.
- Sun, X.-H., Zhu, X.-Q., Tang, H.-S., Zhang, Q., and Luo, T.-Y., 2014, The Gongchangling BIFs from the Anshan–Benxi area, NE China: Petrological–geochemical characteristics and genesis of high-grade iron ores. *Ore Geology Reviews*, 60, 112–125.
- Toplis, M.J., and Corgne, A., 2002, An experimental study of element partitioning between magnetite, clinopyroxene and iron-bearing silicate liquids with particular emphasis on vanadium. *Contributions to Mineralogy and Petrology*, 144, 22–37.
- Trendall, A., 2009, The significance of iron-formation in the Precambrian stratigraphic record. *Precambrian sedimentary environments: A modern approach to depositional systems*, 33, 33–66.
- Van Baalen, M., 1993, Titanium mobility in metamorphic systems: a review. *Chemical Geology*, 110, 233–249.
- Wan, Y., Dong, C., Liu, D., Kröner, A., Yang, C., Wang, W., Du, L., Xie, H., and Ma, M., 2012, Zircon ages and geochemistry of late Neoproterozoic syenogranites in the North China Craton: a review. *Precambrian Research*, 222, 265–289.
- Wan, Y., Dong, C., Wang, W., Xie, H., and Liu, D., 2010, Archean Basement and a Paleoproterozoic Collision Orogen in the Huoqiu Area at the Southeastern Margin of North China Craton: Evidence from Sensitive High Resolution

- Ion Microprobe U–Pb Zircon Geochronology. *Acta Geologica Sinica (English Edition)*, 84, 91–104.
- Wang, C., Konhauser, K.O., and Zhang, L., 2015, Depositional environment of the Paleoproterozoic Yuanjiacun banded iron formation in Shanxi Province, China. *Economic Geology*, 110, 1515–1539.
- Wang, C., Zhang, L., Lan, C., and Dai, Y., 2014, Rare earth element and yttrium compositions of the Paleoproterozoic Yuanjiacun BIF in the Lüliang area and their implications for the Great Oxidation Event (GOE). *Science China Earth Sciences*, 57, 2469–2485.
- Wang, W., Yang, E., Zhai, M., Wang, S., Santosh, M., Du, L., Xie, H., Lv, B., and Wan, Y., 2013, Geochemistry of ~ 2.7 Ga basalts from Taishan area: Constraints on the evolution of early Neoproterozoic granite–greenstone belt in western Shandong Province, China. *Precambrian Research*, 224, 94–109.
- Wu, M., Zhao, G., Sun, M., Yin, C., Li, S., and Tam, P.Y., 2012, Petrology and P–T path of the Yishui mafic granulites: implications for tectonothermal evolution of the Western Shandong Complex in the Eastern Block of the North China Craton. *Precambrian Research*, 222, 312–324.
- Xue, G.Q., Gelius, L.J., Sakyi, P.A., Zhou, N.N., Chen, W.Y., Su, B.C., Li, H., Zhong, H.S., and Su, Y.P., 2014, Discovery of a hidden BIF deposit in Anhui province, China by integrated geological and geophysical investigations. *Ore Geology Reviews*, 63, 470–477.
- Yang, J.–H., Wu, F.–Y., Wilde, S.A., and Zhao, G., 2008, Petrogenesis and geodynamics of Late Archean magmatism in eastern Hebei, eastern North China Craton: geochronological, geochemical and Nd–Hf isotopic evidence. *Precambrian Research*, 167, 125–149.
- Yang, X., Liu, L., Lee, I., Wang, B., Du, Z., Wang, Q., Wang, Y., and Sun, W., 2014, A review on the Huoqiu banded iron formation (BIF), southeast margin of the North China Craton: Genesis of iron deposits and implications for exploration. *Ore Geology Reviews*, 63, 418–443.
- Zhai, M.–G., and Santosh, M., 2011, The early Precambrian odyssey of the North China Craton: a synoptic overview. *Gondwana Research*, 20, 6–25.
- Zhai, M., and Santosh, M., 2013, Metallogeny of the North China Craton: link with

- secular changes in the evolving Earth. *Gondwana Research*, 24, 275–297.
- Zhao, G., Sun, M., Wilde, S.A., and Sanzhong, L., 2005, Late Archean to Paleoproterozoic evolution of the North China Craton: key issues revisited. *Precambrian Research*, 136, 177–202.
- Zhao, G., Wilde, S.A., Cawood, P.A., and Lu, L., 1998, Thermal evolution of Archean basement rocks from the eastern part of the North China Craton and its bearing on tectonic setting. *International Geology Review*, 40, 706–721.
- Zhao, G., Wilde, S.A., Cawood, P.A., and Sun, M., 2001, Archean blocks and their boundaries in the North China Craton: lithological, geochemical, structural and P–T path constraints and tectonic evolution. *Precambrian Research*, 107, 45–73.
- Zhao, L., Chen, H., Zhang, L., Li, D., Zhang, W., Wang, C., Yang, J., and Yan, X., 2016, Magnetite geochemistry of the Heijianshan Fe–Cu (–Au) deposit in Eastern Tianshan: Metallogenic implications for submarine volcanic-hosted Fe–Cu deposits in NW China. *Ore Geology Reviews*.
- Zhao, W.W., and Zhou, M.–F., 2015, In-situ LA–ICP–MS trace elemental analyses of magnetite: The Mesozoic Tengtie skarn Fe deposit in the Nanling Range, South China. *Ore Geology Reviews*, 65, 872–883.

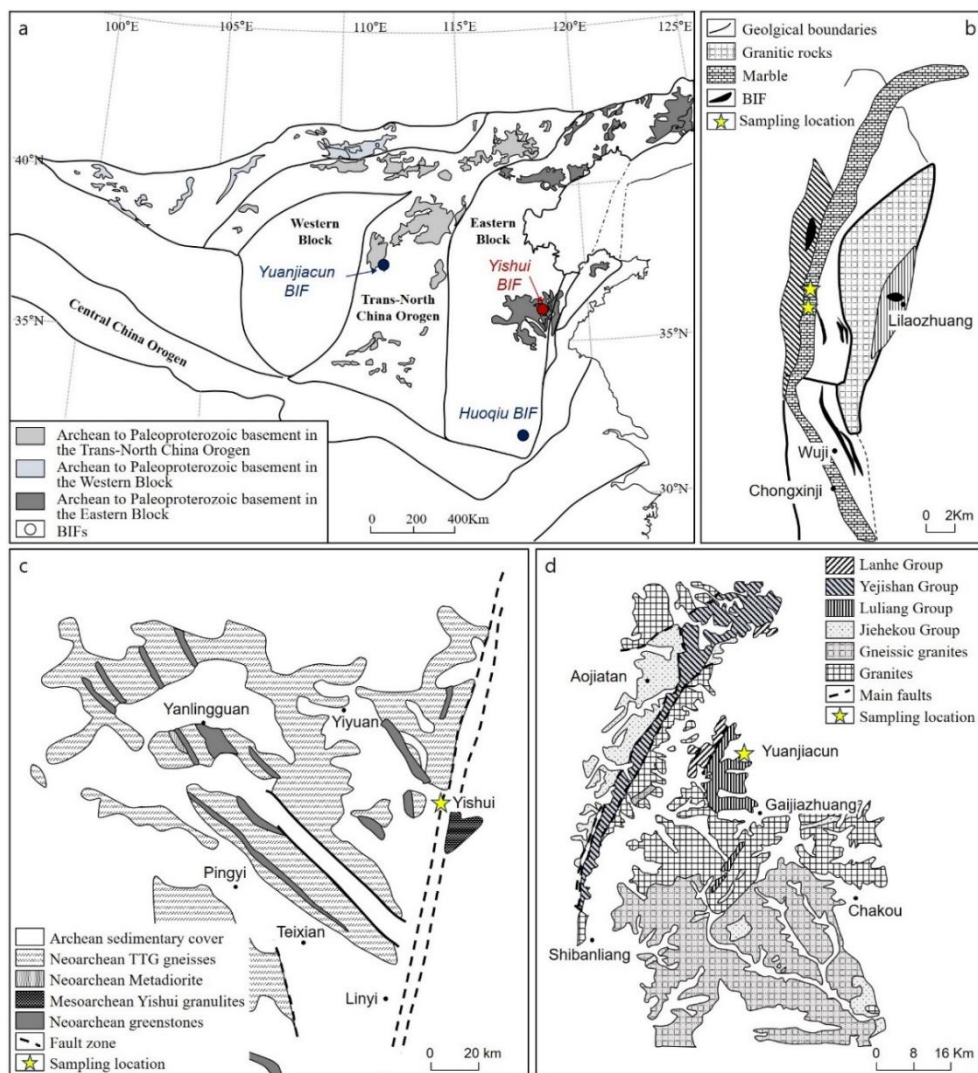


Figure 5.1. (a) Geological map of the North China Craton (Zhao et al., 2005). Simplified geological map of the (b) Huoqiu BIF (Xue et al., 2014), (c) Yishui BIF (Cao et al., 1996) and (d) Yuanjiacun BIF (Wan et al., 2010).

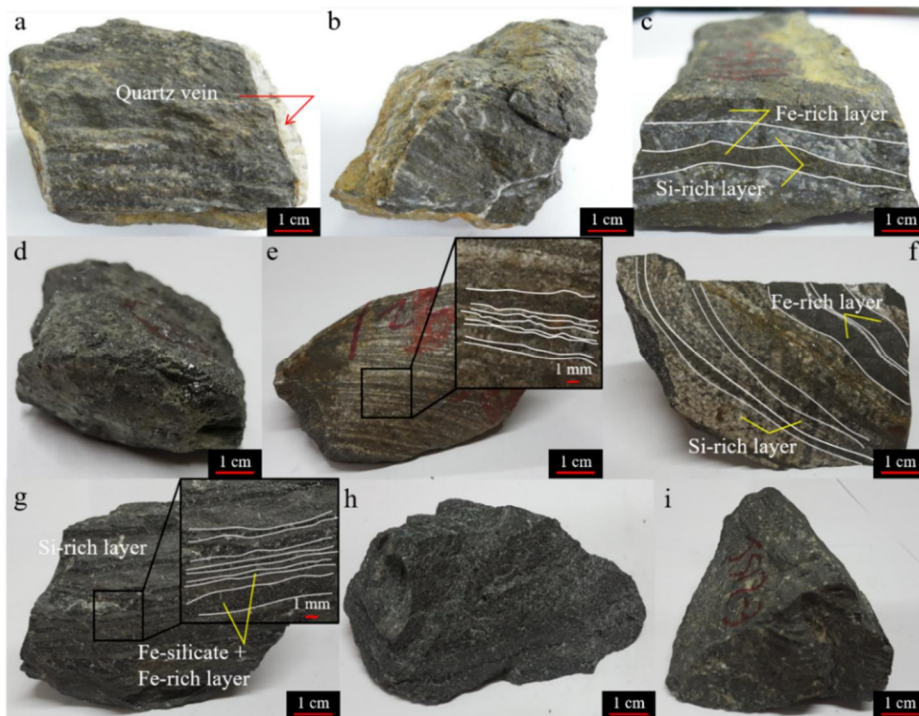


Figure 5.2. Photographs of iron ores from Yishui BIF (a–c) (Moon et al., 2017), Huoqiu BIF (d–f) and Yuanjiacun BIF (g–i). White lines indicate the individual bands.

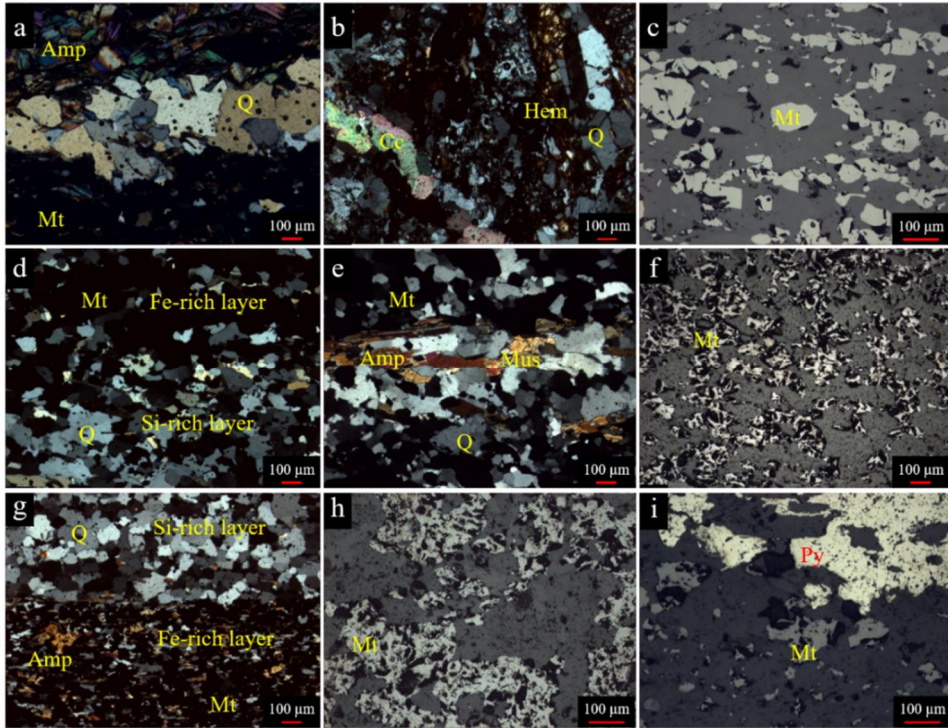


Figure 5.3. Photomicrographs of iron ore from Yishui BIF (a–c), Huoqiu BIF (d–f) and Yuanjiacun BIF (g–i). The mineral abbreviations are listed as follows: Mt–magnetite, Amp–amphibole, Hem–hematite, Q–quartz, Py–pyrite, Mus–muscovite.

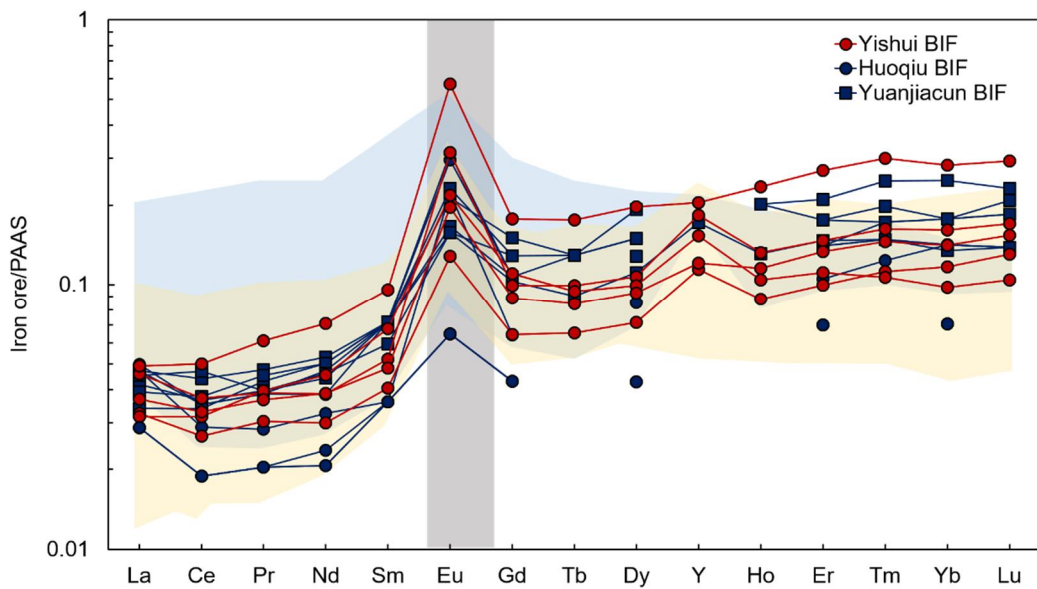


Figure 5.4. Post Archean Average Shale normalized REY (REE + Y) patterns of the iron ores from Yishui, Huoqiu, Yuanjiacun BIFs; the values of the Post Archean Average Shale based on McLennan (1989). The blue and yellow fields are the compositional ranges of iron ores from Huoqiu and Yuanjiacun BIFs, respectively. Literature whole-rock REY compositions of Huoqiu and Yuanjiacun BIFs are from Hou et al. (2014) and Yang et al. (2014).

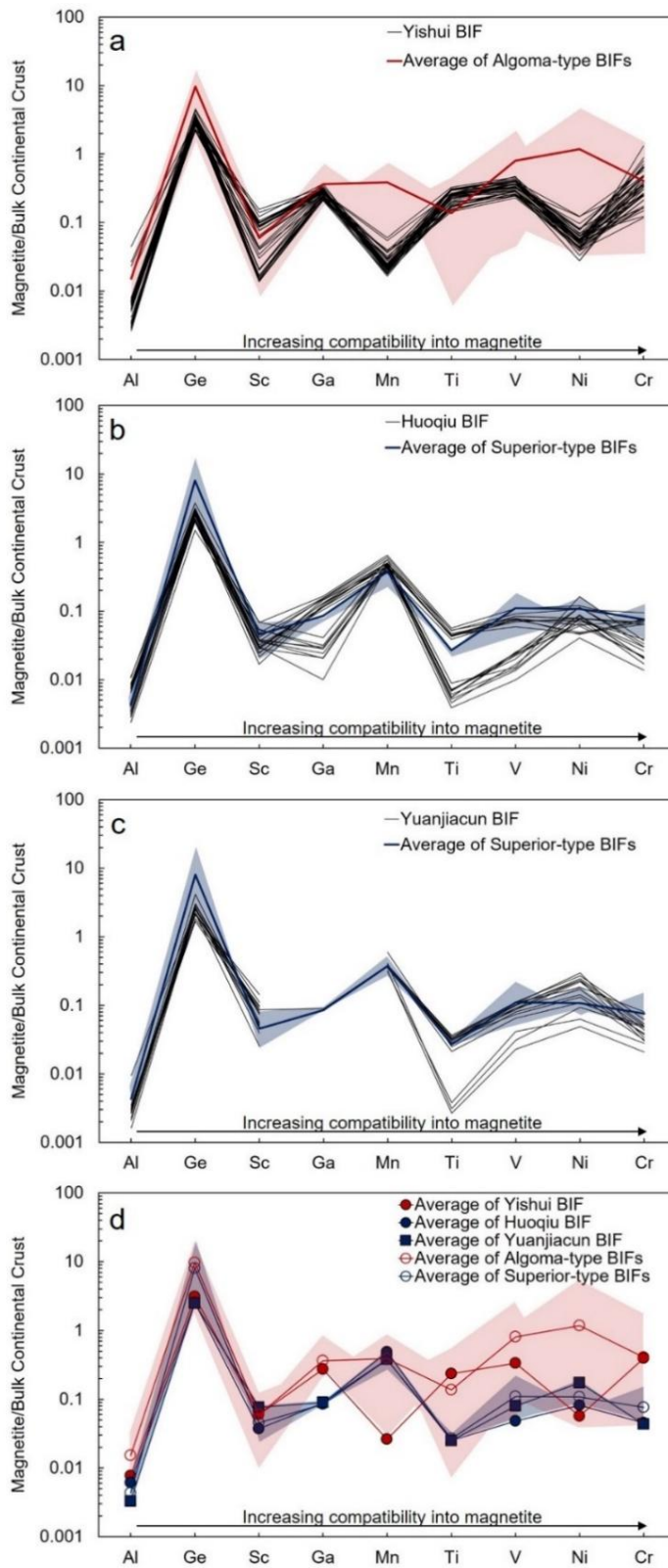


Figure 5.5. Bulk continental crust normalized trace elements in magnetite from (a) Yishui BIF, (b) Huoqiu BIF and (c) Yuanjiacun BIF with average of Algoma– and Superior–type BIFs. The red and blue fields are the compositional ranges of magnetites from Algoma– and Superior–type BIFs, respectively. Bulk continental crust values used for normalization are from (Rudnick and Gao, 2003). Elements are ordered with an increase in compatibility into magnetite to the right (Dare et al., 2012).

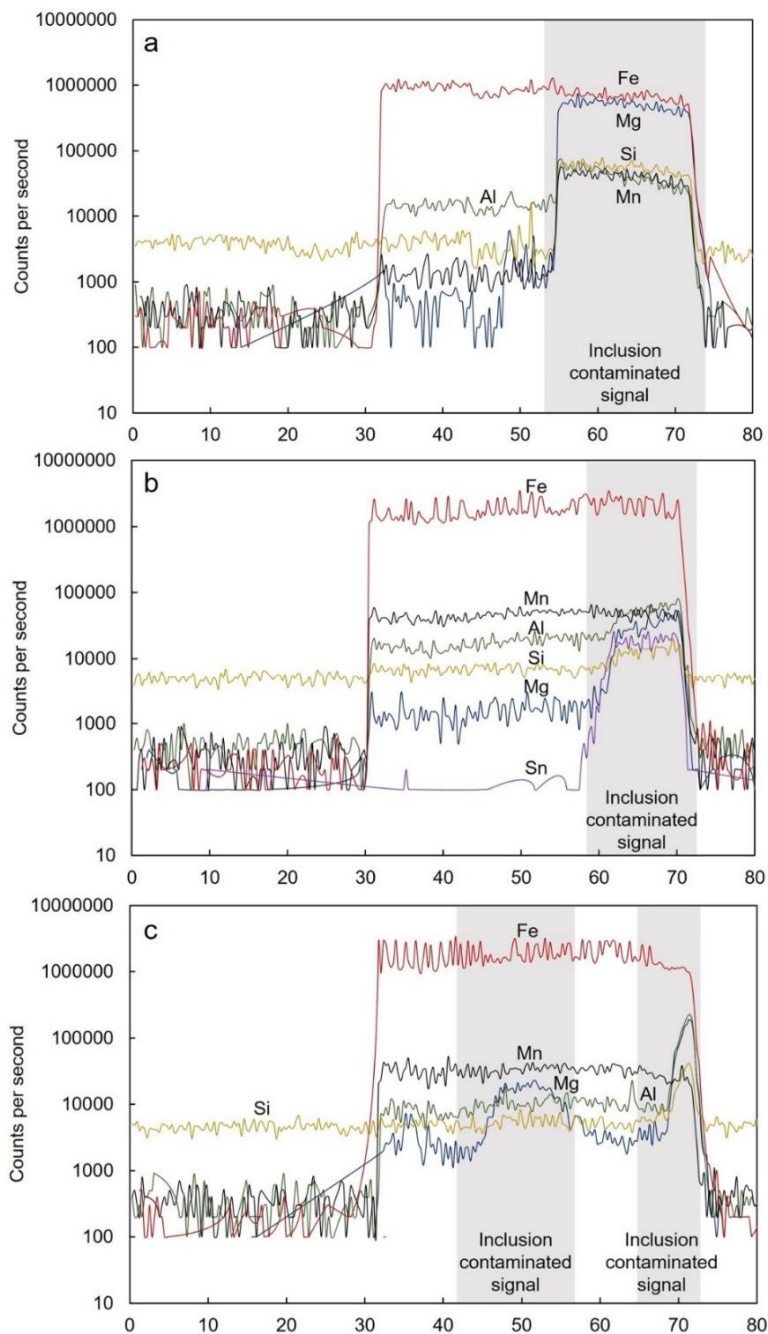


Figure 5.6. Time-resolved analytical signals of an LA-ICP-MS analysis across a magnetite grain from (a) Yishui BIF and (b) Huoqiu BIF and (c) Yuanjiacun BIF.

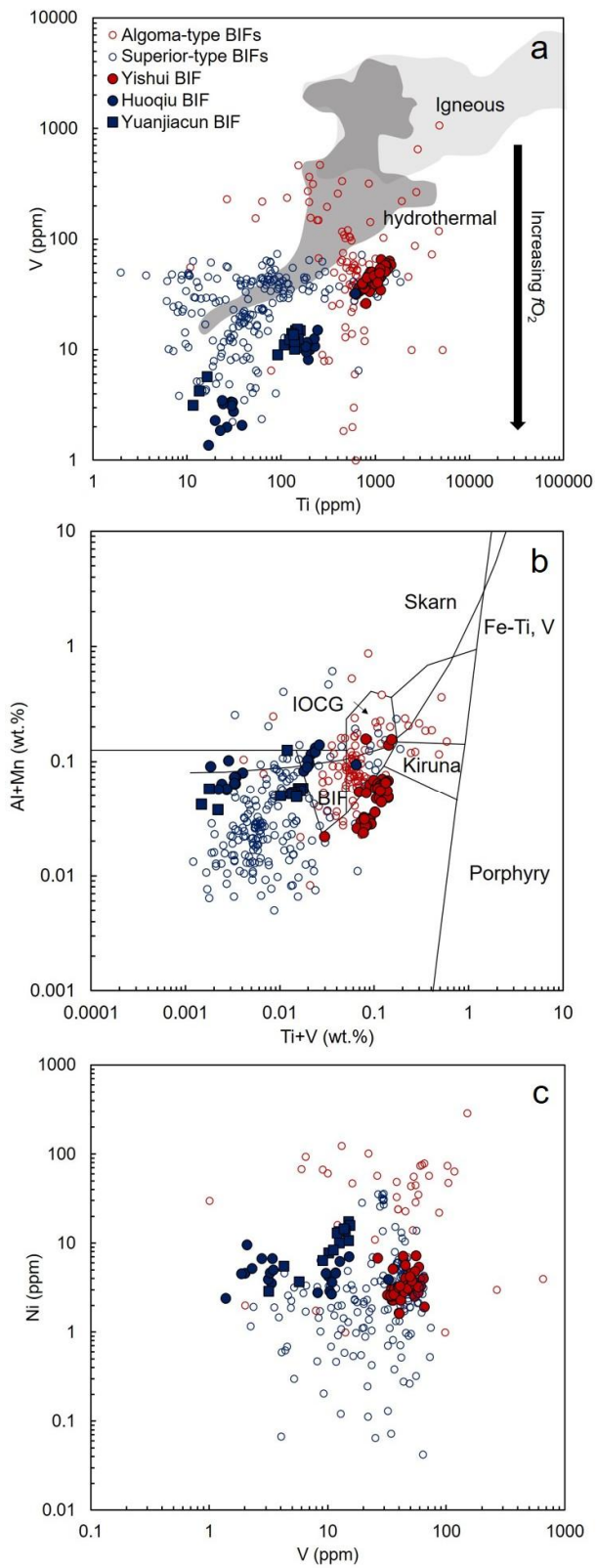


Figure 5.7. Binary diagram of (a) V vs. Ti (Knipping et al., 2015). The dark grey and light grey areas indicate magnetite of igneous and hydrothermal origin, respectively (Nadoll et al., 2014). Plots of chemical discrimination diagram for magnetite of (b) Ti+V vs. Al+Mn. The reference fields are from Dupuis and Beaudoin (2011) and Nadoll et al. (2014). The values are shown in weight percent (wt. %). Plot of (c) Ni vs. V for magnetites (Zhao et al., 2016).

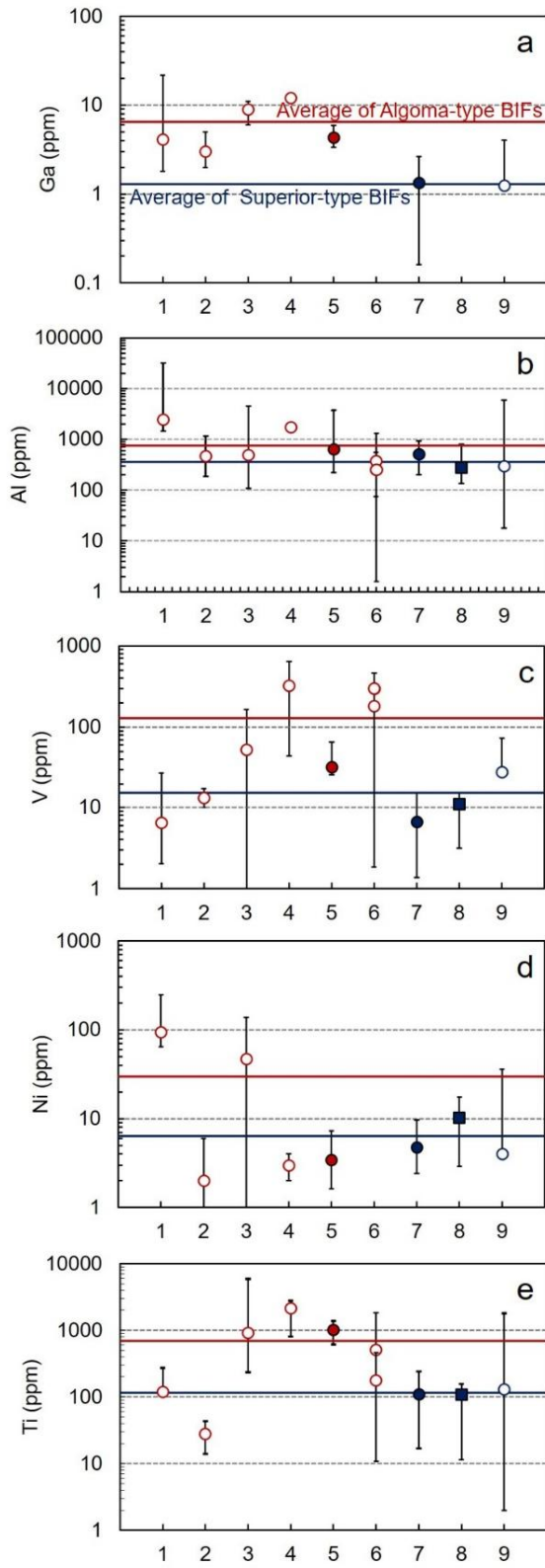


Figure 5.8. Plots for (a) Ga, (b) Al, (c) Ni, (d) V and (e) Ti concentration in magnetites of studied BIFs. The error bars represent the maximum and minimum contents of each element in magnetite from each BIF. The average values of Algoma- and Superior-type BIFs are shown as red and blue lines, respectively. The Wadi Karim and Um Anab BIFs in 6 are separately plotted. The BIFs are ordered based on their ages. 1: Nuvvuagittuq BIF (3.75 Ga; Mloszewska et al., 2012); 2: Magin BIF (2.6–2.8 Ga; Duparc et al., 2016); 3: Izok Lake BIF (2.58–2.68 Ga; Makvandi et al., 2016); 4: Randalls (2.66 Ga; Steadman et al., 2014); 5: Yishui BIF (2.6 Ga; this study); 6: Wadi Karim and Um Anab BIFs (Neoproterozoic; Basta et al., 2011); 7: Houqui BIF (2.6–2.8 Ga; this study); 8: Yuanjiacun BIF (2.3–2.2 Ga; this study); 9: Sokoman BIF (1.88 Ga; Chung et al., 2015). The symbols as for Figure. 5.7.

Table 5.1 The average major elements (wt.%) of the iron ores from the BIFs with representative values.

	SiO ₂	Al ₂ O ₃	TiO ₂	Fe ₂ O ₃ ^T	MgO	CaO	N ₂ O	K ₂ O	MnO	P ₂ O ₅	Total
Yishui BIF	53.1	0.4	0.0	40.3	2.5	1.3	0.2	0.1	0.1	0.0	98.3
	42.0	0.5	0.0	43.8	1.7	6.5	0.1	0.0	0.1	0.0	99.7
	37.2	1.1	0.1	55.4	3.7	1.6	0.2	0.1	0.1	0.1	99.8
	47.6	0.5	0.0	46.7	3.6	0.9	0.0	0.1	0.1	0.1	99.9
	44.6	0.4	0.0	51.2	2.5	0.9	0.0	0.0	0.0	0.1	100.0
Average	44.9	0.6	0.04	47.5	2.8	2.3	0.1	0.1	0.1	0.1	
Huoqiu BIF	61.8	0.5	0.1	34.3	1.5	1.2	0.1	0.0	0.1	0.1	99.3
	60.1	0.4	0.1	36.6	1.6	1.3	0.0	0.0	0.1	0.1	100.2
	57.4	0.1	0.0	33.7	5.9	1.6	0.0	0.0	0.4	0.1	98.8
	57.2	0.1	0.0	34.9	5.9	1.6	0.0	0.0	0.4	0.1	99.8
	45.3	0.1	0.0	54.4	1.4	0.6	0.0	0.0	0.1	0.0	100.6
	45.2	0.1	0.0	53.6	1.4	0.6	0.0	0.0	0.1	0.0	99.7
Average	54.5	0.3	0.0	41.2	3.0	1.2	0.0	0.0	0.2	0.1	
Yuanjiacun BIF	57.9	0.3	0.0	41.7	0.6	0.8	0.0	0.0	0.1	0.1	100.5
	55.8	0.3	0.0	43.2	0.6	0.8	0.0	0.0	0.1	0.09	99.7
	45.2	0.1	0.0	51.7	1.8	1.7	0.0	0.0	0.1	0.1	99.4
	44.9	0.1	0.0	52.5	1.9	1.7	0.0	0.0	0.05	0.1	99.9
Average	50.9	0.2	0.0	47.3	1.2	1.3	0.0	0.0	0.1	0.1	

Fe₂O₃^T = total Fe oxide.

Table 5.2 Trace and rare earth elements (ppm) of iron ores from the BIFs.

	Yishui BIF					Huoqiu BIF						Yuanjiacun BIF			
La	1.75	1.25	1.21	1.40	1.88	1.10	1.10	1.80	1.90	1.80	1.80	1.60	1.80	1.30	1.50
Ce	2.95	2.13	2.52	2.62	3.98	1.50	1.50	2.80	2.80	2.30	2.60	2.90	3.50	2.70	3.00
Pr	0.34	0.27	0.35	0.32	0.54	0.18	0.18	0.34	0.34	0.25	0.26	0.35	0.42	0.38	0.40
Nd	1.30	1.02	1.54	1.31	2.41	0.70	0.80	1.30	1.60	1.10	1.20	1.50	1.80	1.70	1.70
Sm	0.29	0.22	0.38	0.27	0.53	0.20	0.20	0.40	0.40	0.20	0.30	0.40	0.40	0.40	0.40
Eu	0.34	0.14	0.23	0.21	0.62	0.07	0.07	0.32	0.34	0.24	0.27	0.18	0.17	0.23	0.25
Gd	0.46	0.30	0.51	0.41	0.83	0.20	0.20	0.50	0.50	0.30	0.40	0.50	0.60	0.70	0.60
Tb	0.08	0.05	0.07	0.07	0.14							0.10		0.10	0.10
Dy	0.50	0.34	0.47	0.43	0.92	0.20	0.20	0.50	0.50	0.40	0.40	0.70	0.60	0.90	0.70
Y	4.94	3.09	4.14	3.26	5.52										
Ho	0.13	0.09	0.10	0.11	0.23									0.20	0.20
Er	0.42	0.28	0.32	0.38	0.77	0.20	0.20	0.40	0.40	0.30	0.30	0.50	0.40	0.60	0.50
Tm	0.07	0.05	0.04	0.06	0.12			0.06	0.06	0.05	0.05	0.07	0.07	0.10	0.08
Yb	0.45	0.33	0.28	0.40	0.80	0.20	0.20	0.40	0.40	0.40	0.40	0.50	0.50	0.70	0.50
Lu	0.07	0.06	0.05	0.07	0.13			0.06	0.06	0.06	0.06	0.08	0.09	0.10	0.08
Eu/Eu* _{PAAS}	4.18	2.44	2.44	2.85	4.19	1.64	1.64	3.30	3.51	4.43	3.57	1.86	1.57	1.92	2.31
Eu/Eu* _{NASC}	4.05	2.36	2.36	2.76	4.05	1.57	1.57	3.18	3.38	4.28	3.45	1.79	1.52	1.86	2.23
La/La* _{PAAS}	1.16	1.05	1.13	1.14	1.18	1.45	2.06	1.21	2.36	2.35	2.69	1.38	1.29	1.18	1.10
Ce/Ce* _{PAAS}	0.88	0.85	0.89	0.90	0.91	0.77	0.77	0.82	0.80	0.77	0.85	0.89	0.93	0.88	0.89
La/Yb _{PAAS}	0.29	0.28	0.32	0.26	0.17	0.41	0.41	0.33	0.35	0.33	0.33	0.24	0.27	0.14	0.22

Post Archean Average Shale (PAAS) and North American Shale Composite (NASC) values are from McLennan (1989) and Condie (1993), respectively. $La/La^*_N = La_N / (3Pr_N - 2Nd_N)$ (Bolhar et al., 2004), $Ce/Ce^*_N = 2 \times Ce_N / (La_N + Pr_N)$, $Eu/Eu^*_N = 2 \times Eu_N / (Sm_N + Gd_N)$ (Lan et al., 2014b).

Table 5.3 Average of trace elements (in ppm) of magnetite from the BIFs.

		Mg	Al	Ti	V	Cr	Mn	Co	Ni	Zn	Ga	Mo	Pb
Yishui BIF	Avg (n=45)	1153	822	994	45	51	50	1	3	5	4	1	0
	SD	3658	1299	254	11	32	109	0	1	13	1	0	1
Huoqiu BIF	Avg (n=22)	211	517	132	8	23	375	1	5	9	1	0	0
	SD	503	220	138	7	81	53	1	2	4	1	0	0
Yuanjiacun BIF	Avg (n=14)	208	276	107	11	6	295	1	10	8	1	1	0
	SD	587	155	54	4	2	53	1	5	4	1	1	0

n = number of analytical points

SD= standard deviation

Chapter 6. Summary and conclusions

Reconstruction of the genesis of BIFs is still unrevealed due to complex formation mechanism of BIFs. In this study, petrological, mineralogical and geochemical studies of iron ore and magnetite from BIFs and their related wall rock (amphibolite) were conducted.

The studied BIFs are located in NCC, which are Yishui BIF and Yuanjiacun BIF. The results show that Yishui BIF was precipitated from a mixture of less than 1% high-temperature hydrothermal fluids ($> 250\text{ }^{\circ}\text{C}$) and seawater with insignificant detrital input. In addition, the related wall rock (Yishui amphibolite) is geochemically akin to alkali basalts and OIB. On the basis of these results, mantle plume model is suggested to explain both genesis of Yishui BIF and petrogenesis of Yishui amphibolite.

Yuanjiacun BIF was formed during the GOE. Hence, the timing for the formation of Yuanjiacun BIF has close association with the coeval oxygen fugacity. We observed hematite at the edge of the some magnetite grains. The results can be used to evaluate the change of oxidation condition.

Using the data obtained in this study together with compiled literature data, I investigated systematic differences in magnetite compositions between Archean Algoma- and Paleoproterozoic Superior-type BIFs in order to understand the role of their genetic conditions on the chemistry of magnetite. The magnetites from the Algoma-type BIFs are more enriched in trace elements than those from the Superior type because the former originated dominantly from high temperature hydrothermal fluid under low oxygen fugacity conditions while the latter formed mainly from low temperature and relative oxidized sea water.

요약 (국문 초록)

호상철광상(Banded iron formation)은 지질학적 특징에 따라서 호상구조를 띠고 퇴적기원을 가지는 광상이다. 호상철광상은 대부분 선캄브리아기에 형성되었고, 초기지구 환경과 지각 진화의 재구성, 그 시기의 대기과 해양 상태, 광합성 세균의 역할의 이해 등에 있어서 매우 중요한 정보를 제공해 주고 있다. 이러한 특성에 따라서 호상철광상의 성인 연구는 국내외 지질학자들에게 상당히 많은 관심을 받고 있다. 이전 연구 결과 호상철광상은 선캄브리아기에 해수와 높은 온도의 열수 시스템으로부터 철과 규소를 공급 받아서 형성되었다고 밝혀졌지만, 아직 규명되지 않은 부분이 많이 있다.

호상철광상의 성인과 관련된 지각 진화 과정 간의 관계를 이해하기 위해, 본 학위 논문에서는 북중국 산둥 반도에 위치하고 있는 이수이 호상철광상의 광석과 관련 모암인 각섬암을 대상으로 희토류 원소를 이용한 지구화학적 연구를 수행하였다. 연구 결과 이수이 호상철광상은 신시생대에 해수와 0.1~1%의 >250°C 열수 시스템의 혼합으로 인해 형성되었음을 밝혔다. 맨틀 플룸 모델은 이수이 호상철광상뿐만 아니라 관련되어 나타나는 모암의 성인, 신시생대의 북중국의 지각 진화과정을 가장 잘 설명할 수 있는 모델로 제시되었다.

호상철광상이 형성 될 당시 대기의 산소 농도의 변화를 알아보고자 자철석 연구를 수행하였다. 광석 현미경 하에서 자철석의 가장자리에 적철석이 성장해 있는 것을 관찰했고, 라만 분광법을 통해 그 변화를 확

인하였다. 북중국의 유안지아쿤 호상철광상은 대산화사건에 의해 대기중에 산소가 급증하던 시기에 형성되었다. 그에 따라 자철석의 가장자리가 산화를 받아서 적철석으로 변화했음을 알 수 있었다. 결론적으로 유안지아쿤 호상철광상과 대산화사건간의 밀접한 연관성이 있었음을 유추 할 수 있다.

호상철광상은 형성 시기와 환경에 따라서 크게 알고마 유형과 슈퍼리어 유형 호상철광상으로 나뉜다. 다른 형성환경에서 형성된 호상철광상과 수반되어 나타나는 자철석의 미량원소 함량 간의 연관성을 알아보고자 하였다. 알고마 유형 호상철광상은 슈퍼리어 유형 호상철광상에 비해 고온, 환원된 환경에서 형성되었기 때문에, 이러한 형성 환경의 차이가 자철석의 미량원소 함량에 영향을 미쳤음을 가정 할 수 있다. 연구 결과 알고마 유형과 슈퍼리어 유형 호상철광상의 자철석의 미량 원소는 타입별로 뚜렷한 양상을 나타냈고, 이는 이전 연구 결과 제시되었던 두 호상철광상의 타입 연구 결과와도 일치하게 나타남을 확인했다.

주요어: 호상철광상, 북중국, 대산화사건, 지구화학, 희토류 원소, 각섬암, 자철석, 선캄브리아기

학번: 2012-20339

